MINISTRY OF NATIONAL EDUCATION

THE ANNALS OF "DUNAREA DE JOS" UNIVERSITY OF GALATI

Fascicle IX
METALLURGY AND MATERIALS SCIENCE

YEAR XXXII (XXXVII)
June 2014, no. 2

ISSN 1453-083X

2014
GALATI UNIVERSITY PRESS

EDITORIAL BOARD

THE ANNALS OF "DUNAREA DE JOS" UNIVERSITY OF GALATI.
FASCICLE IX. METALLURGY AND MATERIALS SCIENCE
N^0. 2 – 2014, ISSN 1453 – 083X

Table of Content

THE ANNALS OF "DUNAREA DE JOS" UNIVERSITY OF GALATI
FASCICLE IX. METALLURGY AND MATERIALS SCIENCE
N^0. 2 – 2014, ISSN 1453 – 083X

ANTIMICROBIAL PROPERTIES OF SEMICONDUCTIVE OXIDE NANOPARTICLES. FROM FUNDAMENTAL TO APPLICATION[1]

Mariana (BUȘILA) IBĂNESCU[1*], Dana TUTUNARU[2], Viorica MUȘAT[1]
[1]"Dunărea de Jos" University of Galaţi, Centre of Nanostructures and Functional Materials-CNMF,
111 Domnească Street, 800008, Galaţi, Romania
[2]"Dunărea de Jos" University of Galaţi, Faculty of Medicine and Pharmacy,
111 Domnească Street, 800008, Galaţi, Romania
[*]Corresponding author;
e-mail: mariana.ibanescu@ugal.ro

ABSTRACT

A problem of modern society is the spread of diseases worldwide. Infection control and maintaining a high level of hygiene by applying antimicrobial coatings (including medical products, packaging materials, membrane filter/water treatment or filters in air conditioning) are of the greatest importance. Hospitals, pharmaceutical production, food factories must be thoroughly disinfected in order to destroy pathogenic microbes. Microbial contamination of water is a major threat to public health. With the emergence of organisms resistant to many antimicrobial agents there is an increased demand for improved disinfection methods.

Recently, the confluence of nanotechnology and biology has led to metals and metal oxides under the form of nanoparticles as potential antimicrobial agents. Nanoparticles have unique and well defined physical and chemical properties which can be manipulated suitably for desired applications. The applications of nanoparticles as antimicrobials is gaining relevance in prophylaxis and therapeutics, in medical devices, food industry and textile fabrics.

This work focuses on the properties of ZnO nanoparticles doped with different concentrations of silver. The mechanism of action of nanoparticles as bactericidal will be highlighted in this study. Specific applications of the investigated nanoparticles are presented.

KEYWORDS: semiconductive oxide nanoparticles, antimicrobial properties

1. Introduction

Increasing health and hygiene requirements have increased interest in obtaining functional semiconductor oxide nanomaterials which have non-toxic and bioactive properties, are cost-effective and antimicrobial and provide UV protection. A large number of materials which were considered to be safe develop toxicity at nano size ranges which is mainly related to the increased specific surface area and high reactivity of nano size materials [1]. In this context, in recent years an increasing interest in the synthesis of new materials with improved efficiency has been manifested. Among these materials, semiconductor oxide nanoparticles (ZnO, TiO_2, SnO_2, CuO, etc.) present a great potential [2]. Polymer nanocomposites containing semiconductive zinc oxide nanoparticles have attracted a great interest due to their unique chemical and physical properties and important biological applications especially duet o their bactericidal effect [3]. The semiconductor oxides have an antibacterial activity of bactericidal and bacteriostatic type, as a result of the photocatalytic effect in the presence of UV radiation. Due to this property, these oxides have a very high potential for numerous applications in various antiseptic fields [2, 4]: in food industry for the processing of fresh food, which can not be pasteurized; in pharmaceutical industry for the production of antiseptics (bandages, burn); in textile industry for removal of microorganisms from raw materials; in medical clinical laboratories, medical wards with a higher risk

[1] Papers presented at the second edition of the Scientific Conference of Doctoral Schools from "Dunarea de Jos" University of Galati, CSSD-UDJG 2014, Galati, May 15-16, 2014.

factor for infection with pathogenic microorganisms; antiseptic filter air conditioning, where microorganisms can grow and become very harmful to human health, potable water, etc. Antimicrobial efficiency of biocidal materials varies greatly between different types of microorganisms. Disinfection resistance varies in the order of Gram-negative bacteria, Gram-positive bacteria. To interpret the effect of antimicrobial metal oxide semiconductor nanoparticles a number of mechanisms have been proposed. The antimicrobial and antioxidative activity of ZnO nanoparticles in suspension or applied on the fabric or other materials, is based on a number of mechanisms, most of which are known [7]: interruption membrane/cell wall transfer of electrons; the penetration of ions into the cell, which prevents DNA replication and affects the structure and permeability of cell membranes; generation of reactive oxygen species (ROS) [5-10]. The combination of ZnO with silver is advantageous for several reasons. On the one hand, silver is a well-known antibacterial material, furthermore it might improve the photocatalytic action of the ZnO. This report concerns the solvothermal preparation of zinc oxide and silver- doped zinc oxide nanoparticles for antimicrobial applications. This manuscript reports studies on Ag/ZnO nanoparticles with high antibacterial activities prepared by a chemical procedure successfully prepared. The resulting materials were investigated using electron microscopy (SEM), optical absorption (UV–VIS). Also, the antimicrobial activity of the as prepared materials was measured using the paper disc method.

2. Experimental details

2.1. Materials and microorganisms

Silver nitrate ($AgNO_3$), acetic acid (CH_3COOH), zinc oxide (ZnO) nanoparticles were purchased from Sigma–Aldrich and used as received.

Antimicrobial susceptibility was performed on isolated bacteria from urine culture Gram-negative bacteria, *Escherichia coli (E. coli)* and the Gram-positive bacteria, *Staphylococcus aureus (S. Aureus)* on Mueller-Hinton agar.

2.2. Synthesis

ZnO was dopped with different amounts of $AgNO_3$ (0.1, 5 and 15at%). The commercial nanoparticles are spherically shaped with a diameter smaller than 50 nm. Isopropanol was used as solvent for the preparation of all the solutions. An amount of 0.3 g ZnO nanoparticles was dispersed in 100mL isopropanol and 0.1 at%, 5 at% or 15 at% $AgNO_3$ was added in these ZnO dispersions under magnetic stirring for 2 h at room temperature in dark condition. The resulting nanocomposite precipitates were washed several times with ethanol and dried at 70°C.

2.3. Characterization of Ag/ZnO nanoparticles

The crystalline structures of the obtained nanoparticles were identified by X-ray diffraction patterns using a DRON-3 diffractometer system (Burevestnik, USSR) with CoKα radiation, λ=1.789 Å. SEM images were obtained with a Quanta 200 scanning electron microscope operating at 15kV and X-ray Energy Dispersive Spectrometer (EDS-FEI). Specimens were prepared by dispersing the samples by sonication in 2-propanol and by depositing a few drops of the suspensions on carbon-coated grids.

2.4. Antimicrobial testing

The antimicrobial activity of Ag/ZnO composites with respect to simple ZnO was investigated by using the paper disc method on Mueller-Hinton agar without blood against the Gram-negative bacteria, *Escherichia coli (E. coli)* and the Gram-positive bacteria, *Staphylococcus Aureus (S. Aureus)* on Mueller-Hinton agar with blood. For this, it has been used sterilized paper disc of 6 mm in diameter impregnated with 10 µl (5mg/1mL) solution of the composite. In each sterilized culture dish, 0.2mL fresh broth cultured for 24h was added followed by 20mL melted nutrient agar medium at approximately 50^{o}C. The dishes were then cooled down to room temperature before being ready for use. The samples were then gently pressed against the medium plate to have good contact with the inoculated agar, then turned flat. The samples stayed in a constant temperature incubator at 37 ± 1^{o}C for 24 h, before the inhibition zones were measured.

The method for antimicrobial testing was standardized by correlation of zone diameters with minimal inhibitory concentration determined in broth.

3. Results and discussions

3.1. XRD analysis

Figure 1 shows the X-ray diffraction patterns of the ZnO and Ag/ ZnO nanoparticles examined in the form of powder. Diffraction lines exhibited three additional peaks at 2θ = 37.3^o, 40.3^o and 42.6^o, which were assigned to the (1 0 0), (0 0 2), (1 0 1) planes of specifically hexagonal zinc oxide nanoparticles. No characteristic peaks of silver phases were observed in Figure 1, indicating that the samples are single crystalline phase. These data revealed the successful formation of Ag/ZnO.

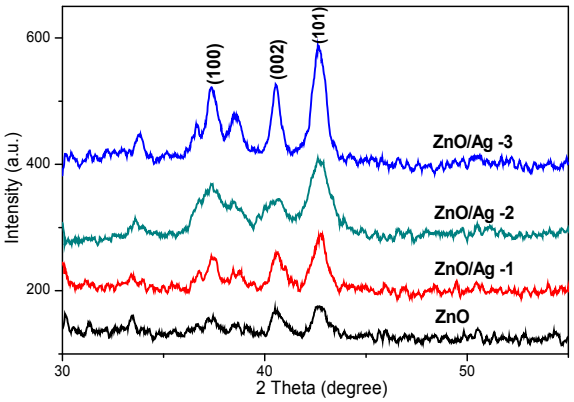

Fig. 1. *XRD patterns for ZnO and Ag/ZnO nanoparticles with different concentration of Ag*

3.2. Surface morphologies

Figure 2 shows SEM images of undoped and ZnO nanoparticles doped with different concentrations of Ag (0.1, 5, 15 at%). These images indicate the existence of agglomerates. With the increase of dopant concentration, there is a decreased tendency of these agglomerations (Figure 2d). EDS spectra indicate the presence of the Ag dopant, with the other chemical elements from the composition of the samples (Zn and O). The peaks of carbon (C) and iron (Fe) come from the substrate of samples used to perform the SEM analysis. The obtained nanopaticles contain a smaller amount of silver as compared to the concentration of Ag^+ ions in solution. At the same time, the EDS results confirm the increase of the amount of silver in the obtained nanoparticles with the increasing concentration of the dopant in solution.

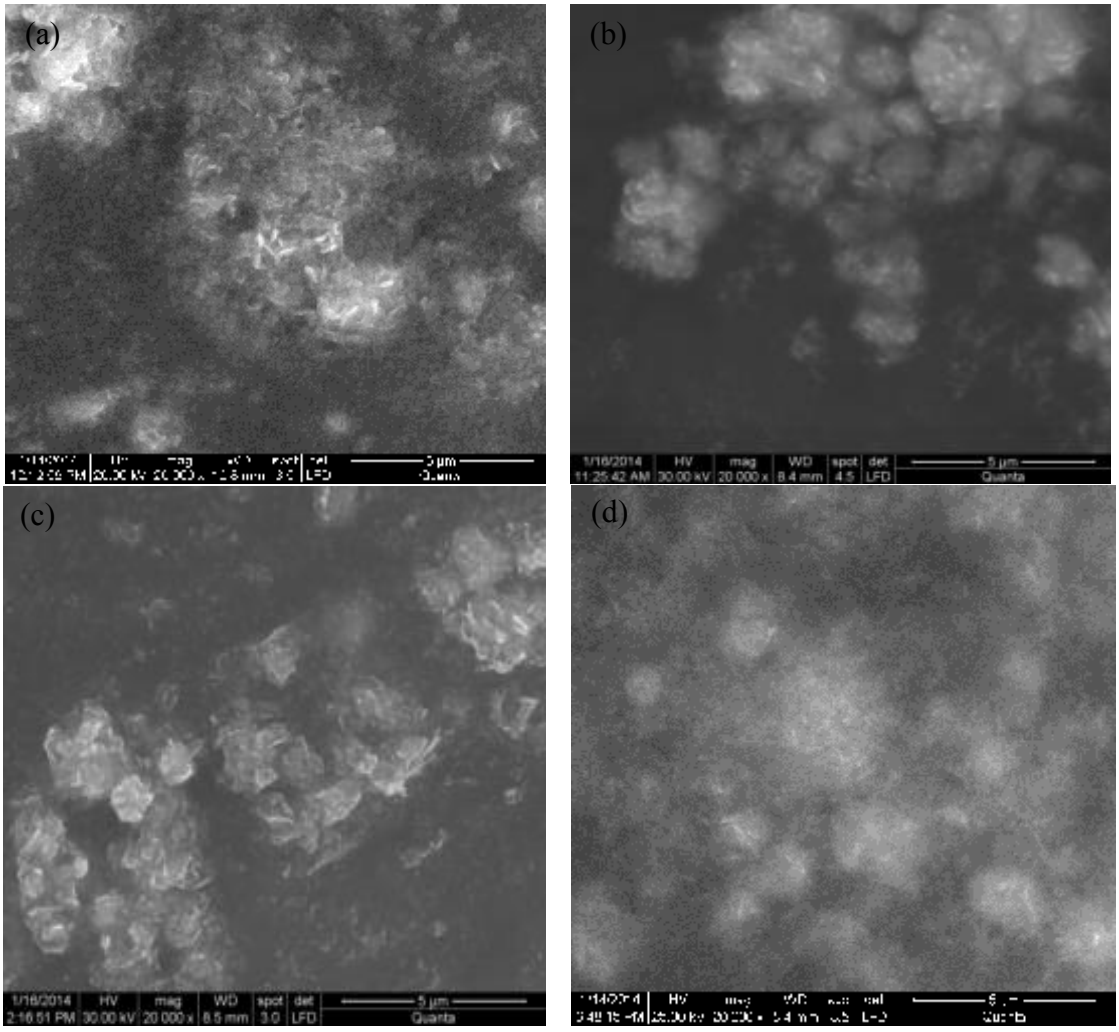

Fig. 2. *SEM images for a) ZnO nanoparticles; b-d) Ag/ZnO nanoparticles with different concentration of Ag*

3.3. Antimicrobial activities

In Figure 4 it is presented the antimicrobial activity of ZnO (1) and Ag/ZnO (2-5) nanoparticles (6-9) tested by the disc and well diffusion agar methods. The presence of an inhibition zone clearly indicated the antibacterial effect of these nanoparticles. The size of inhibition zone was different according to the type of bacteria, and the concentrations of Ag doped ZnO nanoparticles.

According to the results, it can be concluded that ZnO nanoparticles are effective antibacterial agents both on Gram-positive and Gram-negative bacteria. The same results were confirmed in the study of Zhongbing *et al*. (2008) in which Gram-negative membrane and Gram-positive membrane disorganization was approved by transmission electron microscopy of bacteria ultrathin sections [11]. Makhluf *et al*. (2005) attributed the antibacterial behavior of MgO to several mechanisms, namely generation of reactive oxygen species (ROS), interruption of the membrane/cell wall by transfer of electrons; ion penetration into the cell, generated in ZnO using chemiluminescence residues, prevents the replication of DNA and affects the structure and permeability of the cell membrane [12].

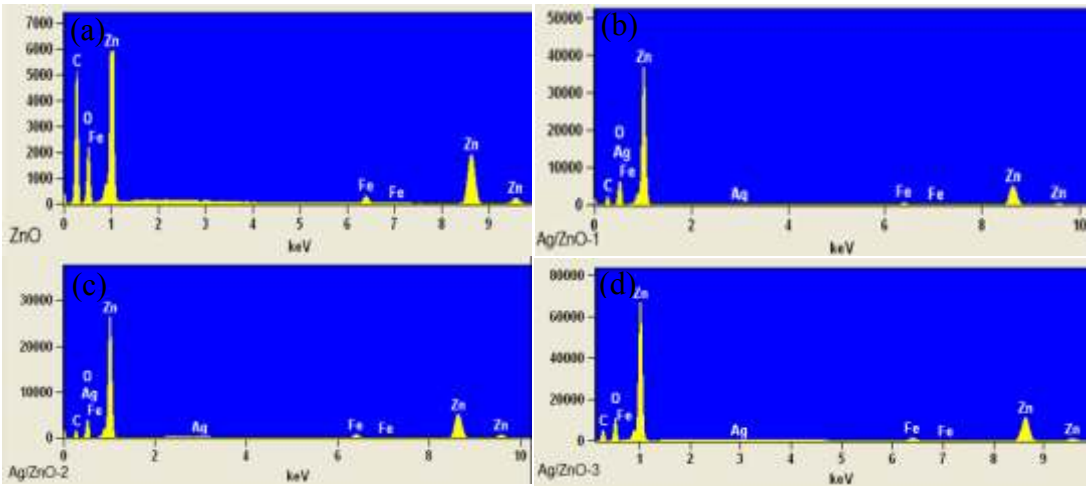

Fig. 3. *EDX spectrum for a) ZnO nanoparticles; b-d) Ag/ZnO nanoparticles with different concentration of Ag*

Sawai *et al*. (1996b) measured the active oxygen species, the H_2O_2 produced in ZnO residue and the concentration of H_2O_2 produced was directly proportional to the concentration of ZnO particles [13]. H_2O_2 was also detected by Yamamoto *et al*. (2004) [14]. Stoimenov *et al*. (2002) suggest that there could be electrostatic interactions between the involved area and bacteria [15].

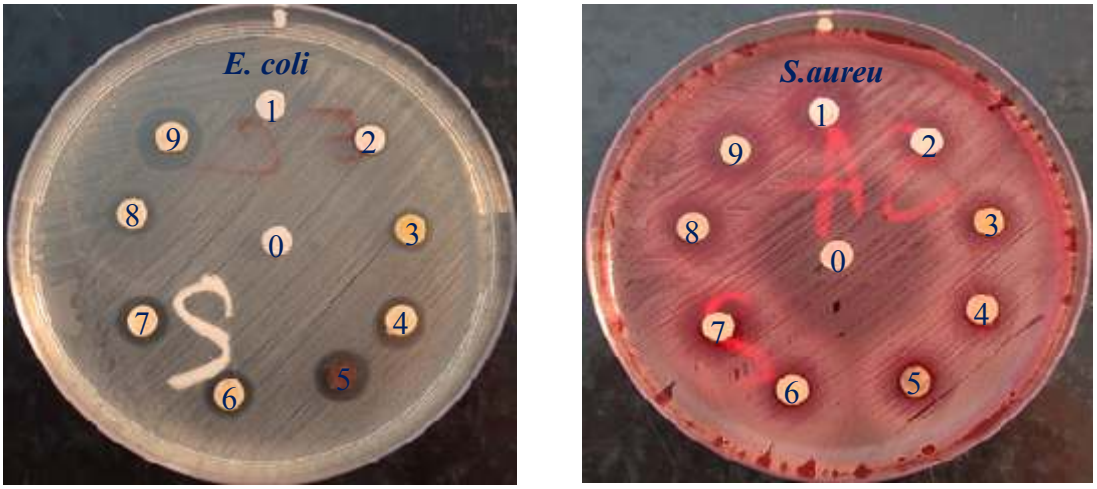

Fig. 4. *Zone of inhibition for ZnO (1), Ag/ZnO (commercial ZnO nanoparticles) (2-5), Ag:ZnO (ZnO nanoparticles obtained of synthesis) (6-9)*

Karunakaran C. *et al.* (2011) obtained Ag-doped ZnO nanoparticles with an average size of 50 nm, which leads to an increase in the contact surface and thus to an increase of their antimicrobial activity. The experimental evidence suggests that the dominant mechanisms of bacterial activity of ZnO is based on the production of reactive oxygen species (ROS - in particular in the presence of ultraviolet light), which chemically interact with the bacterial cell. [5-10]. Under light irradiation ZnO nanoparticles (Eg = 3.37 eV) generated electron–hole pairs. The hole (h^+) reacted with OH^- on the surface of NPs, generating hydroxyl radicals ($OH^\bullet$), superoxide anion (O^{2-}) and perhydroxyl radicals ($HO_2^\bullet$). These highly active free radicals damaged the cells of microorganism as a result of decomposition and complete destruction [16-17].

On the other hand silver ions disrupt the DNA replication and cell division. Both antimicrobial agents seem to compromise the integrity of bacterial membrane because of chemical interactions.

The results of the antimicrobial tests confirm that the optical and photo-catalytical behaviour of the hybrid metal (Ag)/semiconductor (ZnO) composite nanoparticles is consistent with the increase of the photo-catalytic activity of Ag/ZnO composite nanoparticle with respect to intrinsic ZnO nanoparticles [18]. This recommends Ag-doped ZnO nanoparticles composite for potential application in medical devices, food industry and textile fabrics.

4. Conclusions

ZnO and ZnO/Ag nanoparticles were prepared. The XRD measurement confirms that the sol-gel derived ZnO and silver-doped ZnO nanoparticles consist of Wurtzite-type nanocrystallites with different crystalline orientation, but (101) is the dominating peak. Increasing dopant concentration, respectively Ag, leads to a decrease in the size of nanoparticles that increase the specific surface area but also decrease the agglomeration.

Antimicrobial activity was recorded with respect to the increased amount of dopant.

References

[1]. K. M. Reddy, F. Kevin, B. Jason, G. W. Denise, H. Cory, P. Alex - *Selective toxicity of zinc oxide nanoparticles to prokaryotic and eukaryotic systems*. J. Appl. Phys. Lett., 90 (21), 2007, p. 1-3.

[2]. T. C. Horan, D. H. Culver, R. P. Gaynes, W. R. Jarvis, J. R. Edwards, C. R. Reid - *Nosocomial Infections in Surgical Patients in the United States*, *January 1986-June 1992*, National Nosocomial Infections Surveillance (NNIS) System. In Infection Control and Hospital Epidemiology, The Official Journal of the Society of Hospital Epidemiologists of America, 14, 1993, p. 73-80.

[3]. B. S. Atiyeh, M. Costagliola, S. N. Hayek, S. A. Dibo - *Effect of silver on burn wound infection control and healing: review of the literature.* Burns. 33, 2007, p. 139-148.

[4]. K. Tinker, *Moment of Truth: Proper Air Flow Critical to Healthcare Laundries*, In White Paper from the Healthcare Laundry Accreditation Council, 2010.

[5]. X. H. Wang, Y. M. Du, H. Liu - *Preparation, characterization and antimicrobial activity of chitosan-Zn complex,* Carbohydr. Polym. 56, 2004, p. 21-26.

[6]. Y. Inoue, Y. Kanzaki, *The mechanism of antibacterial activity of silver-loaded zeolite*, J. Inorg. Biochem., 67, 1997, p. 377.

[7]. A. Bacchi, M. Carcelli, P. Pelagatti, C. Pelizzi, G. Pelizzi, F. Zani - *Antimicrobial and mutagenic activity of some carbono- and thiocarbonohydrazone ligands and their copper(II), iron(II) and zinc(II) complexes*, J. Inorg. Biochem., 75, 1999, p. 123-133.**[8]. Z. H. Yang, C. S. Xie, X. P. Xia, S. Z. Cai -** *Zn^{2+} release behavior and surface characteristics of Zn/LDPE nanocomposites and ZnO/LDPE nanocomposites in simulated uterine solution*, J. Mater. Sci. Mater. Med., 19, 2008, p. 3319-3326.

[9]. E. P. Azevedo, T. D. P. Saldanha, M. V. M. Navarro, A. C. Medeiros, M. F. Ginani, F. N. Raffin - *Mechanical properties and release studies of chitosan films impregnated with silver sulfadiazine,* J. Appl. Polym. Sci., 102, 2006, p. 3462-3470.

[10]. Y. M. Qin, C. J. Zhu, J. Chen, Y. Z. Chen, C. Zhang - *The absorption and release of silver and zinc ions by chitosan fibers,* J. Appl. Polym. Sci., 101, 2006, p. 766-771.

[11]. H. Zhongbing, Zh. Xu, Y. Danhong, Y. Guangfu, L. Xiaoming, K. Yunqing, Y. Yadong, D. Huang, H. Baoqing - *Toxicological effect of ZnO nanoparticles based on bacteria.* Langmuir, 24(8), 2008, p. 4140-4144.

[12]. S. Makhluf, R. Dror, Y. Nitzan, Y. Abramovich, R. Jelinek, A. Gedanken - *Microwave-assisted synthesis of nanocrystalline MgO and its uses a bacteriocide*, Adv Funct Mater, 15, 2005, p. 1708-1715.

[13]. J. Sawai, E. Kawada, F. Kanou, H. Igarashi, A. Hashimoto, T. Kokugan, M. Shimizu - *Detection of active oxygen generated from ceramic powders having antibacterial activity.* J Chem Eng Jpn, 29, 1996b, p. 627-633.

[14]. O. Yamamoto, M. Komatsu, J. Sawai, Z. Nakagawa - *Effect of lattice constant of zinc oxide on antibacterial characteristics*. J Mater Sci: Mater Med, 15, 2004, p. 847-851.

[15]. P. K. Stoimenov, R. L. Klinger, G. L. Marchin, K. J. Klabunde - *Metal oxide nanoparticles as bactericidal agents*, Langmuir, 18, 2002, p. 6679-6686.

[16]. Y. Kikuchi, K. Sunada, T. Iyoda, K. Hashimoto, A. Fujishima - *Photocatalytic bactericidal effect of TiO_2 thin films: dynamic view of the active oxygen species responsible for the effect,* J. Photochem. Photobiol. A, 106, 1997, p. 51-56.

[17]. B. Halliwell, J. M. C. Gutteridge - *Oxygen toxicity, oxygen radicals, transition metals and disease*, Biochem. J., 219, 1984, p. 1-14.

[18]. M. Ibanescu (Busila), V. Musat, T. Textor, V. Badilita, B. Mahltig - *Photocatalytic and antimicrobial Ag/ZnO nanocomposites for functionalization of textile fabrics*, J. Alloy. Compd., 610, 2014, p. 244-249.

THE ANNALS OF "DUNAREA DE JOS" UNIVERSITY OF GALATI
FASCICLE IX. METALLURGY AND MATERIALS SCIENCE
N^0. 2 – 2014, ISSN 1453 – 083X

ASPECTS OF MATERIALS DECAY UNDER CHEMICAL ATTACK FROM THE LEACHATE TREATMENT PLANT OF THE TIRIGHINA WASTE LANDFILL[1]

Doiniţa NEAGU (PÎRVU), Lidia BENEA*, Eliza DĂNĂILĂ
Research (Competences) Centre: Interfaces-Tribocorrosion and Electrochemical Systems (CC-ITES),
Faculty of Materials and Environmental Engineering, "Dunarea de Jos" University of Galati,
47 Domneasca Street, 800008 Galati, Romania
*Corresponding author
e-mail: Lidia.Benea@ugal.ro

ABSTRACT

Human society faces a number of major problems among which the increasingly negative consequences of environmental pollution. The high uses rate of the natural resources and the large amount of waste generated tend to transform the natural environment, its feed back reactions becoming dangerous to both life and the constructive environment created. Waste is one of the best indicators that measure economic vitality and the society way of life. The economic growth and development most times generate a quantitative increase and diversification of the nature of waste produced in the processes of making community utilities. Currently, waste management and treatment have become crucial and complex issues to ensure sustainable development. Because most municipal landfills do not have a perfect waterproof foundation, leachate infiltration into the soil, subsoil and underground water may occur causing the pollution of these environmental factors. To this end the paper is focused on the collection and treatment of leachate from the municipal waste landfill by presenting modern technologies for the collection and treatment of leachate from uncontrolled municipal waste deposits.

KEYWORDS: waste landfill, leachate, corrosion aspects

1. Introduction

Due to harmonization of the national legislation with the European Union one, part of the legislation was adopted. Thus the leachate collection methods presented in the current national legislation refer only to controlled landfills.

There is no standard method for the leachate collection in order to reduce pollution of soil, subsoil and groundwater.

In accordance with the legislation in force, leachate treatment can be performed in two types of systems, namely:

- the treatment plant of the landfill allowing leachate discharge directly into the natural receptor (in this case the Siret river) in compliance with legislation in force;

- leachate pre-treatment plant for disposal in a municipal sewage treatment plant, while complying with the effluent quality parameter values.

In this respect the uncontrolled municipal landfills where there are no collection facilities or leachate treatment plants, a collection and pre-treatment technology can be applied to decrease the concentrations of salts, heavy metals and organic substances.

In uncontrolled deposits/landfills (mostly from Romania) there are no facilities for the collection and treatment of leachate.

The leachate from municipal waste landfill is generally characterized by a high concentration of organic matter and ammonia and contains potentially toxic substances.

In Fig. 1 is shown an overview of the leachate treatment plant from Tirighina waste landfill.

[1] Papers presented at the second edition of the Scientific Conference of Doctoral Schools from "Dunarea de Jos" University of Galati, CSSD-UDJG 2014, Galati, May 15-16, 2014.

Fig. 1. *Overview of the leachate treatment plant*

In some cases, existing organic substances in wastewater are easily degraded by microorganisms; other substances require a selected adapted flora for their removal and other substances are resistant to attack by microorganisms or are degraded in a long time.

A coexistence of organic substances with different capacities of resistance to the action of microorganisms causes difficulties in the biological treatment of wastewater.

In the case of waste water resulting from wastes landfills (leachate) its quality varies with: depositor age, ambient air temperature, the rainfall rate, permeability of waste, waste layer depth, waste temperature, and waste composition.

The basic characteristic of leachate is its variability. Leachate quantity increases during the rainy periods and falls under drough. Concentrations of pollutants from wastes also vary over the life of depositors so that in the early stages leachate is rich in biodegradable organic substances. With increasing depositor's age the leachate is enriched with readily biodegradable complex organic substances.

In addition, changes in leachate characteristics cannot be foreseen from the beginning, therefore no leachate is constant in time and also two leachates will never be the same. To this are added the cost and environmental risk.

The content of ammonia, the odor and the very dark colour are impediments to the introduction of leachate into the municipal treatment plants.

The main methods used to reduce ammonia nitrogen from wastewater are air stripping of ammonia, chlorine intermittent chlorination (break point), ion exchange, biological nitrification.

2. General information on leachate treatment plant from Tirighina waste landfill

In the municipal landfill of Tirighina leachate forms through waste percolation - in various stages of decay – by rain water; precipitation are responsible for producing the largest amount of leachate in the domestic waste landfill, but they are not the only source of percolation agent; a significant amount of water is contained in the domestic wastes and the decomposition of substances also generates significant volumes of water, all of which contribute to the production of additional quantities of leachate.

In the Tirighina waste landfill, leachate will be collected in a built tank of 1000 cubic meters which will accumulate a quantity of leachate produced for about 14 days, where from it is to be pumped to the treatment plant. The treated leachate, also called permeat, will be collected in the rain water retention basin and thence pumped into the Mittal Steel pipline to be further discharged into the Siret river.

The treatment plant is designed to operate a volume of 1400 cubic meters/month, at the rate of 90% availability and 52 cm/day.

Leachate treatment plant includes:

- Ammonia-stripping unit - manufacturer: Devise Engineering AE;
- Reverse osmosis unit - Wehrle Umwelt;
- Building of the chemical storage tanks, pumps and switchboard room and also the spare parts warehouse.

2.1. Description of the leachate pumping station

The pumps draw from the leachate tank and discharge into the leachate tank installed in the container of the ammonia separation plant. A pump will be continuously running and one in stand by.

The pipes inside the plant, as well as the fittings and valves, are made of stainless steel in order to avoid premature corrosion and the discharge pipe from the plant outlet to the inlet of the leachate tank of the ammonia separation unit is made of 63 mm HDPE. For the pipes passing through walls, special parts to maintain tightness have been provided.

2.2. Description of the tanks building

In the leachate plant, of particular importance is the building of chemical tanks. Considering that the leachate plant must operate at temperatures between -20 ºC and + 400 ºC and also at the freezing and boiling temperatures of the chemicals necessary for the leachate treatment technology, it was established the tanks positioning inside a building called the chemical tanks building.

In Fig. 2 is shown the building of chemical tanks which contains the substances used in the treatment of leachate.

For a good operation, the ammonia separation unit requires the following chemicals:

- Caustic soda of 25% concentration causing the pH of the leachate to raise. The caustic soda used in

the process (treatment of leachate) is a colorless clear odorless slightly viscous liquid, corrosive to metal materials (depending on the nature of the material metal) and in contact with acids it releases toxic gases.

Fig. 2. *Room tanks with chemical substances*

- Hydrochloric acid at a concentration of 38% with the aim of reducing the leachate pH at the plant outlet. The hydrochloric acid used is characterized as a pale yellow liquid of specific odor, corrosive to metallic materials and in contact with alkanes exothermic reactions occur.

- Sulphurous acid in a concentration of 96% is used in the absorption column. The sulphurous acid mentioned above is a colorless liquid, has a characteristic odor and is a very active mineral acid (not an organic acid); also it is the most important compound of sulfur and the most used in industry, also being called "the blood of the industry".

- Secondary product - ammonium sulphate, which is present in liquid form, is colorless and odorless, non-toxic and non-corrosive.

In Fig. 3 is shown the tank which contains the caustic soda of 25% concentration. It is well known that this solution represent a corrosive environment.

Fig. 3. *Tanks with caustic soda solution*

In Fig. 4 is shown the tank which contains the hydrochloric acid at a concentration of 38% and which also is a highly corrosive solution.

Fig. 4. *Tanks with hydrochloric acid solution*

In Fig. 5 is shown the tank which contains the sulphuric acid solution with a high concentration of 96%.

Fig. 5. *Tanks with sulphuric acid solution*

In Fig. 6 is shown the tank which contains the ammonium sulphate solution, which is a secondary product used in the treatment of leachate.

Fig. 6. *Tanks with ammonium sulphate resulting from the process*

Table 1. *Technical characteristics of caustic soda and hydrochloric acid tanks*

Reservoir	Vertical cylindrical, double-walled
The outer diameter of the double wall	2200 mm
The diameter of the storage tank	2000 mm
The height of the storage tank	3000 mm
The diameter inspection cover	600 mm
Leak detector placed between walls	Provided
Building material	GRP*

**Plastics (P) of glass fiber reinforced resin (GR) is a compound of at least two different materials*

The tank characteristics which contain the caustic soda solution and the hydrochloric acid are shown in Table 1.

The tank characteristics which contain the sulphurous acid solution and the ammonium sulphate solution are shown in Table 2.

Table 2. *Technical characteristics of reservoirs with a sulphuric acid and ammonium sulphate*

Reservoir	Retention tank leakage
The outer diameter of the vat	1230 mm
The diameter of the storage tank	1140 mm
The height of the storage tank	1170 mm
The diameter inspection cover	360 mm
Leak detector placed between walls	Provided
Building material	PE*

**Polyethylene (abbreviated PE) or polymethylene is a semi-crystalline thermoplastic polymer of white or semi-transparent colour, the most common plastic produced by the polymerization process; it has excellent chemical resistance to acids, bases and oxides.*

Technical characteristics of hydrochloric acid and caustic soda containers:

- cylindrical shape, double-walled;
- construction material: GRP.

The pipes and fittings are made of PE and PVC; containers are made of glass fiber reinforced pastic.

The hydrochloric acid tank (HCL 38%) has the outer cuvette made of polypropylene and glass fiber. The container and the cuvette are made by polypropylene plates soldering. The resistance of the material is adapted to resist to hydrochloric acid at a concentration of 38% and a maximum operating temperature of 40 ºC. Outside both the tank and cuvette there is PAFS reinforced (fiberglass reinforced polyester) which provides high mechanical strength.

The NaOH (25%) tank is a double-walled tank from GRP materials and inner protection PP.

The building where chemicals are stored is a metal construction, closed with heat insulation panels, fitted with electric heating, ventilation, lighting. The heat insulated panels allow for easy dismantling and removal of the tanks, if applicable.

The metallic surfaces are corrosion protected with epoxy.

With the leachate treatment plant at the Tirighina wastes landfill, due to chlorine acid vapours escape and the sulphuric acid itself, undesired reactions took place in the chemical room, monitored over time. The development of the metallic materials corrosion in the chemical tanks building was monitored at different time intervals.

From the thermodynamic point of view, the metal materials in the presence of acid solutions (in this case vapour produces systems which tend to stabilize by the formation of oxides and salts, respectively.

In the following we will pursue some places where it seems that corrosion had a somewhat higher rate.

Corrosion in this case can be regarded as an attack "intensely localized in cracks, crevices or places where the metal material was not properly covered with anticorrosive material or the treatment was not conducted at the prescribed parameters.

3. Corrosion aspect of plants and equipment

First, corrosion was monitored in the chemical tanks building on 17/10/2013.

The most common and known case of chemical corrosion is the "phenomenon of rusting" of the surfaces of iron, cast iron and mild steel; we can say that in this case the chemical corrosion is present as the vapour substances acted on the metallic materials.

At a first examination it seems a pitting corrosion, a form of localized corrosion in which metal is destroyed very quickly in certain discrete points of the surface, the remaining area being quite significantly attacked. This involves the formation of small holes of significant depths. The consequence of such an attack can be rapid and unexpected

destruction of the structures on which it occurs. The pitting is more misleading as it occurs on passive materials, which present an excellent resistance to generalized corrosion. A pitting corrosion occurs whenever a metallic material whose coating, no matter what kind, is damaged locally and comes into contact with aggressive solutions (in this case high concentrations of acids, strong acids). Pitting cannot be characterized by indicating the average corrosion rate only but by the circumstances in which localized attack occurs (in this case the acid vapour concentration). The main feature of pitting potential in this case is that metallic materials present in an aggressive environment (presence of acid vapour) get repassivated under pitting potential, and only when this potential is exceeded pitting occurs (as shown in images below).

Pitting is a complex process which takes place in several steps on the surface of metallic materials, namely:

1. destruction of the protective layer;
2. pitting initiation and formation;
3. pitting development.

The phenomenon depends on the nature of the metal or the alloy composition, the characteristics of the environment. Metallic inclusions play a decisive role in the initiation of pitting, but aggressive ions also cause pitting initiation.

The pitting growth rate depends on the composition of the material, the concentration of the electrolyte inside the pit and the potential inside pitting.

In the case of sulphuric acid the following reaction occurs:

$$Fe + H_2SO_4 \rightarrow FeSO_4 + H_2 \uparrow$$

In the case of hydrocloric acid the following reaction occurs:

$$Fe + 2HCl \rightarrow FeCl_2 + H_2 \uparrow$$

As mentioned above it is a pitting corrosion (oxidation) or the so-called point rust because of the chemicals attack (sulphuric acid, hydrochloric acid). Pitting corrosion is a localized form of corrosion that is active on metal surface on microscopic scale, while being difficult to predict and locate.

Following the reactions between metal and aggressive environment (in this case - chemicals) corrosion products on the metal surface corrosion products, also called film corrosion, still remain. The thickness of the corrosion film largely depends on the environmental temperature, process duration and aggressiveness of the corrosive environments (in this case, hydrochloric acid has very high concentrations – 96%).

Because ventilation does not work at the appropriate parameters and the ventilation ducts of the acid tanks do not run over the roof of the building to the parameters listed in the documentation, corrosion grows in time. As it can be seen, there is a so-called common general corrosion which has the effect of reducing the thickness of the metal over the entire surface or larger portions and varies depending on the material.

A pitting corrosion occurs whenever metallic material whose coating, no matter what kind, is locally damaged in contact with aggressive solutions.

In Fig.7 are shown some aspects of corrosion during the initial phase (a), (c), (e) and (g) caught on 17/10/2013 and in the final phase (b), (d), (f) and (h), on 04/03/2014. Corrosion is found on components of chemical tanks (a - b), on the parts of the support pillars (c – d), on the supporting beams circuits (e – f) and also on the body chemical feed pump (g - h).

Chemicals under the form of vapour, present in the reservoir chamber, attacked the iron (the predominant material the interior of the building is made of) to give reddish-brown oxide that does not stick (as shown in Fig. 7a-f - at metal parts above the chemical tanks), these layers are porous, allow for further oxidation of the metal and fall off. As known from various experiments, in some cases, as a result of the reaction between the metal and an aggressive environment it tends to crumble and fall, revealing the metal surface with which the air and moisture are to react again, thus resulting in loss of metallic properties.

From further monitoring the corrosion activity in the building of chemical tanks, it was found increased corrosion. During the interval for monitoring corrosion, all forms of corrosion could be seen as follows:

a) General surface corrosion - occurs when the metal surface is corroded evenly, unevenly or in patches by acidic and oxidizing solutions. In this case, on the surface of the metallic material, a dark color film is formed from compounds of cohesion (basic salts, carbonates, etc.).

b) Pitting corrosion (pinching - pitting) occurs when the chemical agent attacks the surface points (present in all phases of monitoring), while progressing the phenomenon causes deep holes and even perforation of the metal. It is difficult to assess by the number of points per unit area or by their depth.

c) Intercrystalline corrosion occurs when the attack occurs on crystalline grain boundaries, resulting in structural damage down to the disintegration of the metal, which is also present in this case.

d) Selective or internal corrosion occurs where a metal or an alloy constituent is attacked and destroyed.

Decomposition of solid solutions is often observed along with separation and attacking only of one component of the alloy, noticed on the water battery which was completely corroded.

Starting with 23/10/2013 we can speak of the notion of thickness of the corrosion films that depend heavily on the process duration and aggressiveness of the corrosive environment.

(a) Components of chemical tanks

(b) Components of chemical tanks

(c) Parts of the support pillars

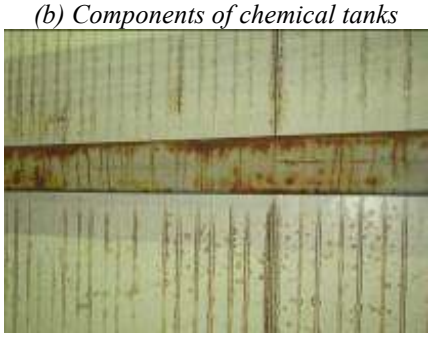

(d) Parts of the support pillars

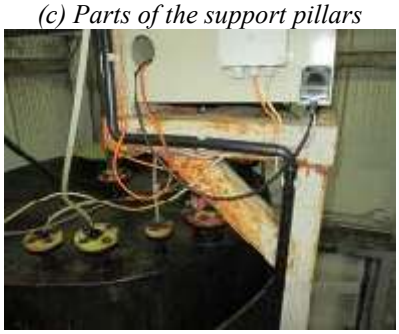

(e) The supporting beam circuit

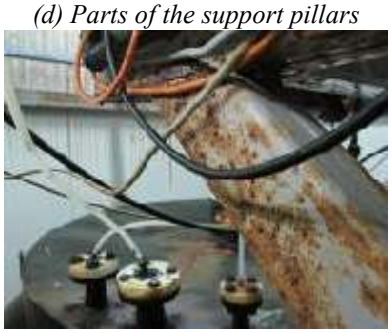

(f) The supporting beams circuit

(g) Body chemical feed pump

(h) Body chemical feed pump

Fig. 7. *Corrosion aspects*

As it is apparent, the film thickness varies within very wide limits, in stages, so one can make some classification according to it, namely:

- thin films are the invisible ones of somewhat smaller thicknesses and can be seen in the initial phase; in this case the specific colour of the metal is affected at times;

- average film thickness which is better highlighted and visible due to the interference of light and appears in slightly different colours (the phenomenon is seen in the period immediately following the initial phase) and then films turn into thick ones and also their colour is very differentiated from that of the metal.

In the case reported, the metal items exposed to the corrosive action, after installation, are no longer accessible (some of them), and not protected against corrosion, during the life of the building they will not affect its durability, but from its monitoring carried out it was found that the entire metal building was subjected to a corrosion process which would result in its destruction in time

4. Conclusion

Immediate action should be taken, for example, the realization of a fan to provide proper air ventilation of the room air thus removing the undesirable chemical or metal vapours.

Currently, methods of stagnating the corrosion process are taken into account due to the presence of high concentrations of chemical substances in this room.

As to metallic materials present in this room they apparently were not treated properly, as protection methods were not met depending on:

- technological parameters of the installation;
- the shape and size of the object to be protected;
- quality of support material;
- protected object location specific to the plant operating conditions;
- application technologies and the possibility of executing the corrosion protection.

Another measure would be anticorrosion coatings which are realized by coating the metal with a thin layer of self protecting material.

The self protecting layer has to meet the following requirements:

- to be compact and adherent;
- to be sufficiently elastic and plastic;
- its thickness to be as even as possible.

Non-metallic coatings can be organic or inorganic, obtained from varnishes, paints, enamels or plastic films, etc.

Acknowledgements

This work was financially supported by the Financing Contract *POSDRU/159/1.5/S/13896 - „Performanță sustenabilă în cercetarea doctorală și postdoctorală – PERFORM",* and partially by research project C2-02/(2012-2015) and Bilateral research project RO-FR, ANCS – Capacitati 702/30-04-2013.

References

[1]. *** - *Technical documentation of the operating system inside Tirighina waste landfill*, Galati, November 2011.
[2]. *** - *Operating handbook on collection and treatment of leachate*, Galati, November 2011.
[3]. *** - *Environmental protection legislation - GD 162/2002 - "The regulation of this activity aims to prevent or reduce as far as possible the negative effects on the environment, in particular pollution of surface waters, groundwater, soil, air, including greenhouse effect as well as any risk to the population health, during the entire life of the waste landfill and after its expiry date".*

THE ANNALS OF "DUNAREA DE JOS" UNIVERSITY OF GALATI
FASCICLE IX. METALLURGY AND MATERIALS SCIENCE
N^0. 2 – 2014, ISSN 1453 – 083X

SILICA THIN FILMS OBTAINING BY SOL – GEL DIP COATING WITH CONTROLLED OPTICAL PROPERTIES[1]

C. MIHOREANU, A. ENEŞCA, A. DUŢĂ*
RTD Center Renewable Energy Systems and Recycling, Transilvania University of Brasov,
29 Eroilor, 500036 Brasov, Romania
*Corresponding author
e-mail: a.duta@unitbv.ro

ABSTRACT

Transparent oxide films are widely employed as antireflection or high reflection coatings, band-pass filters and narrow-band-filters in various optical and electronic devices. The performances of these devices are based on interference effects obtained by alternating layers of high and low refractive indices. Different deposition techniques have been employed for coating glasses with different thin films materials. The metal oxides optical coatings can be deposed on glass substrate by CVD and PVD processes. The heterogeneity between the deposit and the glass substrate is the principal cause of the lack of durability of these coatings. Mono or multilayers materials could be used as colored glazing, which is slightly opaque to the human eye but highly transparent to solar energy. The glazing colors are based on interference in the thin-film coating(s) on the reverse side of the glass. Our research group focuses on investigation of single SiO_2 and SiO_2-TiO_2 multilayers, obtained by dip-coating (DC) deposition technique using sol-gel precursors, as suitable glazing for colored solar-thermal collectors.

By optimizing the deposition parameters (number of deposition sequences, time between deposition sequences, immersion and extraction rate, temperature) and the precursor properties (concentration, additives, etc.) we are able to tailor the morphological and optical properties of silica coated glass. Consequently the transmittance has increased up to 93% in UV-VIS and IR regions and the reflectance is < 5% in VIS and IR regions.

The samples show various morphologies (mostly dense with grains around 30-40 nm) function of the precursor composition (presence of additives) and concentration.

KEYWORDS: SiO_2, coating, sol-gel, morphology, optical properties

1. Introduction

One of the most abundant renewable energy sources is solar energy and conversion systems are developed for producing power (photovoltaic systems) or heat (solar-thermal systems). Among these, the most efficient use of solar energy is in solar-thermal systems using solar thermal collectors [1]. Many of these systems are used in order to reduce the conventional energy demand in public buildings, residential areas [2], and industrial consumers [3].

Nowadays the solar thermal collectors are systems designed to increase solar energy efficiency, quality, life expectancy and profitability.

To fulfill these requirements, but also for decreasing the related building materials costs as well as the necessary time for their installation, the implementation of low cost, high efficiency solar thermal collectors are required [4]. Additionally, for implementing such collectors in the built environment, architectural and aesthetical constraints must be fulfilled. A perfect architectural integration of common glazed or unglazed solar thermal collectors in a building is difficult to obtain.

[1] Papers presented at the second edition of the Scientific Conference of Doctoral Schools from "Dunarea de Jos" University of Galati, CSSD-UDJG 2014, Galati, May 15-16, 2014.

This would mean that the collector is part of the building's envelope or an architectural design element and can therefore not be recognized immediately as a solar collector [5]. Therefore, recent studies show more and more the tendency of coloring the solar thermal flat plate collectors that are usually recommended for buildings' implementation, as they are delivering the thermal agent at a convenient temperature of 80…110 ^{o}C. There are two main ways for coloring solar thermal collectors: by coloring the absorber plate or by coloring the glazing.

The performance criteria of the coating glazing in the solar thermal applications are connected to three factors: high transmittance in UV–VIS–NIR, low reflectance in UV–VIS and chemical stability in the operating conditions: humidity, dust and high exposure to climatic phenomena.

The thermal transmittance, solar and visible transmittance are the main parameters in studying the performance of advanced glazing systems. By adopting double and triple glasses or modern double skin facades, the ratio between transmission and reflection could be reduced [6].

On the other hand, glazing can be colored by tuning the optical properties of multi-layers with different refractive indexes. Such a combination is represented by the silica/titania multi-stacks. A method for obtaining SiO_2/TiO_2 thin films was proposed on the ion beam induced and plasma enhanced chemical deposition [7]. The authors concluded that the refractive index of the film is directly correlated with the titanium content inside the film. It was studied the possibility to integrate dielectric multilayer films of Al_2O_3/SiO_2 and TiO_2/SiO_2 as a colored glazed cover for thermal solar collectors [8]. These multilayer films have been obtained by alternative deposition of dielectric layers with high and low refractive indices.

The authors determined the optical properties of individual oxides of titanium, silicon and aluminum. They observed that the reflectivity and the solar transmission depended on the thickness and the number of alternative dielectric layers in the thickness sensitive thin layers. Cianhung Huang *et all*. prepared a neutral SiO_2/TiO_2 composite hydrosol by the coprecipitation-peptization method. They used titanium tetrachloride and silicon dioxide hydrosol as precursors.

The authors observed that the additive SiO_2 decreased the refractive index and suppressed the aggregation of TiO_2. The results showed that the lower refractive index of SiO_2/TiO_2 thin film could increase the transmittance of visible light [9].

Thus, optimized deposition should be found for each of the component layers. This paper focuses on the SiO_2 layers, where plenty of work is already reported.

Miyazaki and Goto proposed a method to obtain SiO_x film based by RF magnetron sputtering process. This method is very effective for surface modification and consists of ejecting the atoms from a target material and condensing the ejected atoms onto a substrate in a high vacuum environment [12]. In order to obtain the silica thin films, other different methods can be used: chemical vapor deposition (CVD), physical vapor deposition (PVD), reactive magnetron sputtering [13] or spray pyrolysis deposition [14].

Although performant, these reports rely on high-cost deposition methods, therefore alternative investigations should be needed. The sol–gel process represents a method to produce solid materials from small molecules and is especially used for the fabrication of the silicon and titanium oxides. This process involves the transformation of monomers into a colloidal solution (sol), which acts as a precursor for discrete particles or network polymers [10]. The method has the advantages of simplicity and low cost, it is applied at low processing temperature; it has as a result the homogeneous films on glass with high optical properties [15]. Research groups have used the sol–gel process to prepare silica/titanium hybrid films with refractive index varying from 1.44 to 2.20. This film is applied for the triple layer broadband AR coating. One mechanical performance of this film and the morphology of the obtained coating were investigated [11].

After preparing the gel, the deposition could be directly done by various methods, among which dipping represents a feasible alternative [16].

This paper reports the novel results obtained in optimizing the sol-gel SiO_2 preparation and the development of the optimized thin layers deposition by dipping, targeting optimized and performant optical properties, as a first step in obtaining colored glazing for novel flat-plate solar-thermal collectors for the built environment.

2. Experimental part

The silica hydrophilic coating sol was prepared by mixing the tetraethyl orthosilicate (TEOS, 99%), absolute ethanol (EtOH 99.5%), pure water, hydrochloric acid in the volume of (1:8:3:0.5). The mixture was then stirred at 60°C for 2h and aged for 7 days. Silica thin films were deposited on glass substrate (2.5×2 cm^2) by dip – coating technique using speed of 5mm/min. The glass substrates were cleaned previously by ultrasonic equipment in alcohol and then dried using compressed air.

In this study, the parameters that were varied are: number of dipping sequences (6, respectively 10), the amount of gel (0.5; 1; 1.25; 1.5; 1.75; 2 g) dispersed in 50 mL ethanol : water (1:1 v/v) mixture.

For improving the layers homogeneity, the addition of a surfactant was tested: dodecyl-trimethyl-ammonium bromide, DTAB. The tests were developed in parallel series, with and without DTAB addition and the optical properties were comparatively discussed.

The silica thin films obtained were introduced in an oven at 120 °C for 2 hours for drying and slightly sintering. The morphological properties of silica thin films were analyzed using Atomic Force Microscopy (AFM/STM, NT-MDT model NTEGRA Probe Nanolaboratory), in semicontact mode.

The optical properties and the thickness layer were determined by using UV–VIS–NIR spectroscopy (Perkin Elmer, Lambda 950 model, equipped with 150 mm integrating sphere).

Contact angle measurements were done using the sessile drop method (DataPhysics Instrument), and using water as wetting liquid.

3. Results and discussions

The optical properties are significantly influenced by: the layers thickness and by the surface roughness (inducing multiple reflections but also scattering). The thickness of the silica thin films increases with the number of immersions but not linearly probably because the deposited layers are going through a re-organizing process in sequential depositions, Fig.1.

For the silica thin films with DTAB an increase in the layer thickness is observed, due to the ability of the additive to improve the wetting surface and facilitating the adhesion of SiO_2 to the substrate. Thus, when using DTAB, thin films are obtained with higher thickness even if using the minimum amount of gel (0.5 g). Additionally, the mild thermal treatment allows for re-organization in the thin films that are more obvious in films obtained using larger amounts of gel.

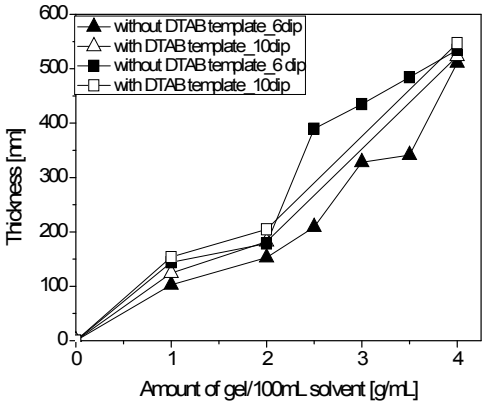

Fig. 1. *The thickness layers of the silica thin films*

It is interesting to notice that, regardless the surfactant addition and the number of immersions, the films obtained with large amount of gel (4 g gel/100 mL solvent) have an almost identical thickness, perhaps as result of reaching a stable surface aspect.

By varying the number of immersions from 6 to 10, for different gel compositions, the morphology of the thin films changed, too, Fig. 2.

The SiO_2 sample with 1 g gel/100 mL has the highest roughness value, and corresponds to a rather inhomogeneous thin film. Increasing the amount of gel leads to a slight roughness decrease up to a certain amount (2.5 g/100 mL), above which the roughness increases as result of the development of thicker, less ordered films.

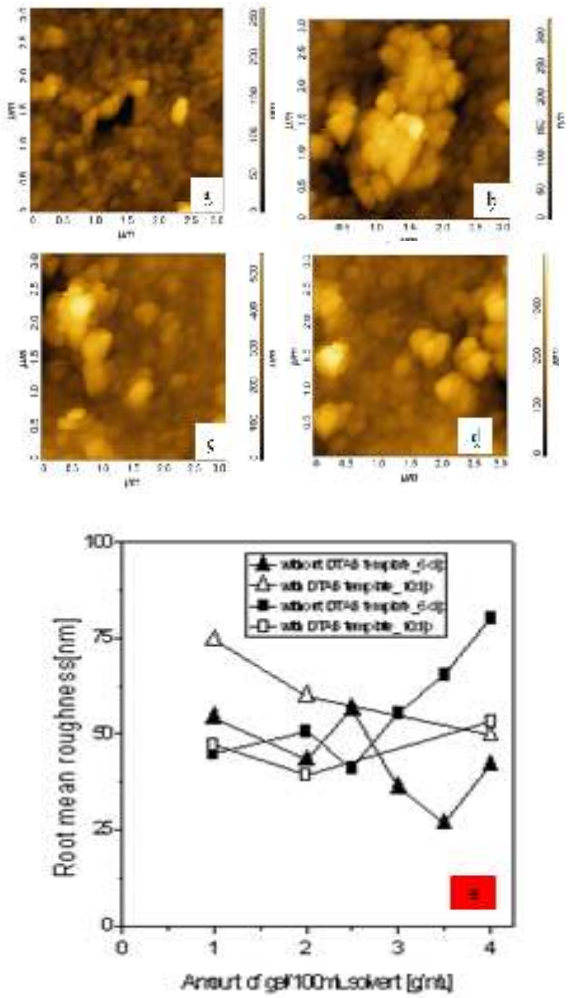

Fig. 2. *AFM images for the sample: (a) 4.0 g _6dip; (b) 2.0 g_DTAB_6dip; c) 2.0 g _10dip; (d) 4.0 g_DTAB_10dip and the variation of the root mean square roughness (RMS) with the amount of gel in 100 mL solvent (e)*

The surfactant addition has also as effect an increase in the surface roughness for the samples

obtained with higher amounts of gel, as a possible result of an "ordering" effect among the silica nanoparticles, that leads to less dense structures (with higher thickness) and with large open pores. Still, the AFM images also show the "macro-smoothening" effect of the surfactant that prevents surface agglomerations, leading to more homogeneous surfaces. The wettability of the thin films is important, as in the working environment, thin water films can condense on the grazing and lead to the distortion of the optical properties or to erosion. The values of the contact angles of water on the thin films were measured immediately after depositing the liquid drop and are presented in Table 1. The water contact angles are low, corresponding to hydrophilic (for several samples to super-hydrophilic) surfaces.

Table 1. *Water contact angle variation on the silica thin films*

Samples without DTAB addition	Contact angle [deg.]	Samples with DTAB	Contact angle [deg.]
SiO_2 0.5g_6dip	22	SiO_2 0.5g_DTAB_6dip	18
SiO_2 1.0g_6dip	15	$SiO_2$1.0g_DTAB_ 6dip	17
$SiO_2$1,25g_6 dip	25	SiO_2 1.25g DTAB_6dip	25
SiO_2 1.5g_6dip	36	SiO_2 1.5g DTAB_6dip	13
SiO_2 1.75g_6dip	11	SiO_2 1.75g DTAB_6 dip	16
SiO_2 2g _6 dip	17	SiO_2 2g DTAB_ 6 dip	9
SiO_2 0.5g_10dip	14	SiO_2 0.5g_DTAB_10 dip	17
$SiO_2$1.0g_10 dip	27	$SiO_2$1.0g_DTAB_ 10dip	29
SiO_2 _2g_10 dip	14	SiO_2 2g DTAB_10 dip	12

The results are following an almost identical trend with the roughness, proving that the morphology is mostly responsive to this behavior and not the chemical composition. As expected, surfactant addition has as result a slight lowering in the contact angle, proving its preferential adsorption on the grains surface. The most important optical properties for glazing are: in UV–VIS–NIR range (T>70%), low reflectance in UV–VIS range (R<15%), low absorbance in UV–VIS–NIR range (A<10%), and controlled refractive index. The silica thin films with and without DTAB addition were investigated by spectral analyses within the 250–2000 nm range.

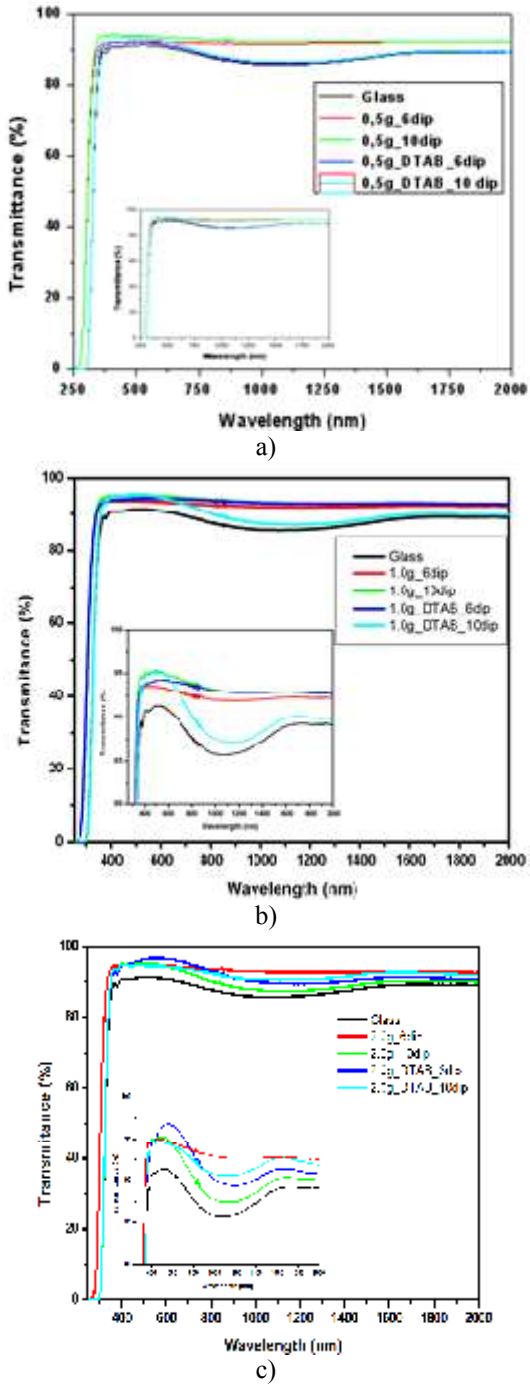

Fig. 3. *Transmittance spectra for silica thin films by dip-coating obtained using: (a): 0.5 g; (b): 1 g; and (c) 2 g gel in 50 mL mixed solvent*

In Fig. 3 there are presented the transmittance spectra for SiO_2 thin films deposited on glass substrate with and without addition of the DTAB

template. These thin films have increased transmittance in the UV range and slight modulation in the VIS and NIR regions, as compared to glass substrate (which has T = 91%). In all situations, the transmittance values are above 80%, making thin films suitable in developing competitive glazing.

The transmittance spectra register the modifications mainly due to the different thickness of the films and its correlation with the refractive index, [10]. High values of the transmittance spectra increase to shorter wavelengths, which is a positive result for solar thermal flat plate collectors that are using high energy solar radiation to convert it into heat. The highest transmittance value (94…95%) appears at 500…600 nm, in the VIS spectral region, while the lowest values correspond to NIR (86…89%). The maximum transmittance values on the three spectral regions of interest (UV, VIS, NIR) are presented in Fig. 4, correlated with the concentration of gel in the deposition suspension. The data show a general trend of decreasing the maximum transmittance values from UV towards NIR for all the films, with values above 90% for the most important spectral regions: UV and VIS.

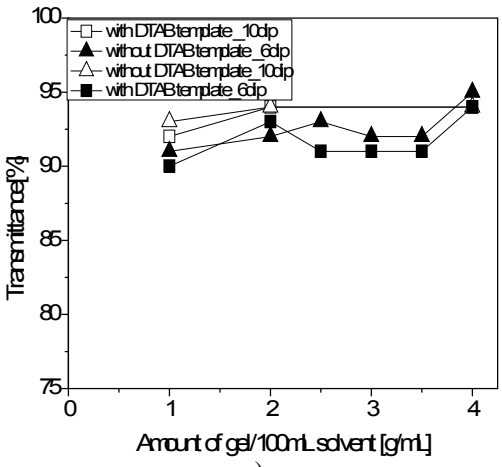

a)

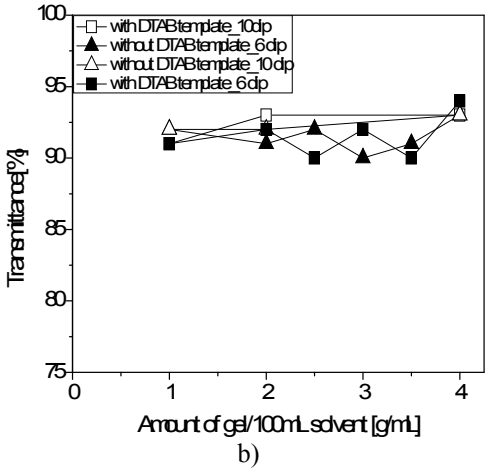

b)

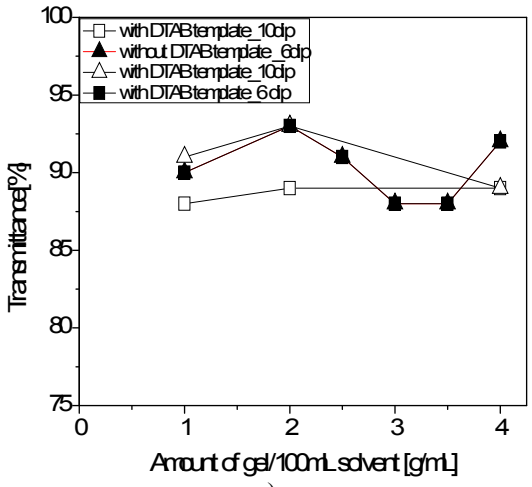

c)

Fig. 4. *Maximum transmittance of the silica thin films, within the spectral range: (a) UV, λ = 250…300 nm; (b) VIS, λ = 300…800 nm; (c) NIR, λ = 800…2000 nm*

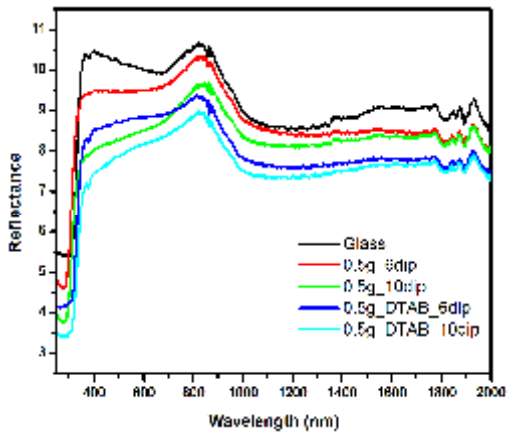

a)

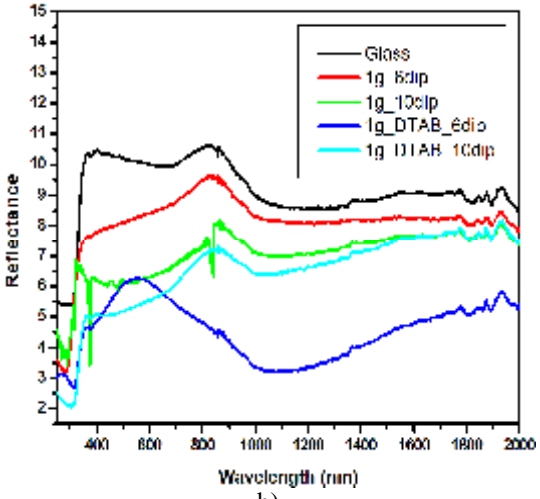

b)

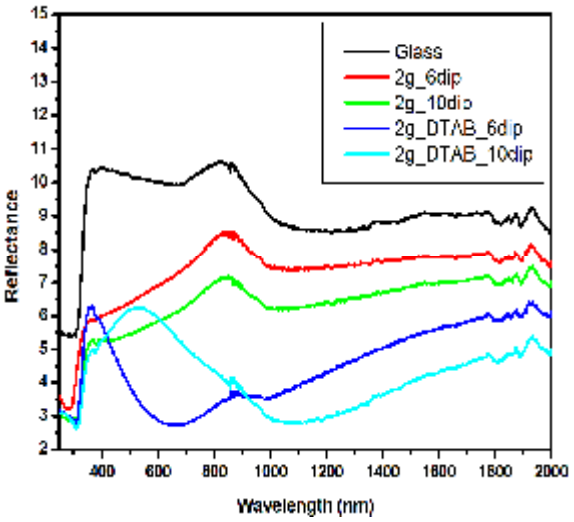

c)

Fig. 5. *Reflectance spectra of the silica thin films obtained using: (a): 0.5 g; (b): 1 g; and (c) 2 g gel in 50 mL mixed solvent*

For the sample obtained by six immersions, the DTAB addition leads to the transmittance values, mainly as consequence of the ordering effect that decreases scattering. The best transmittance values are obtained for the films containing 1g gel/50mL solvent (2g/100mL). For glazings, reflections and scattering need to be minimized as being one main cause of losses.

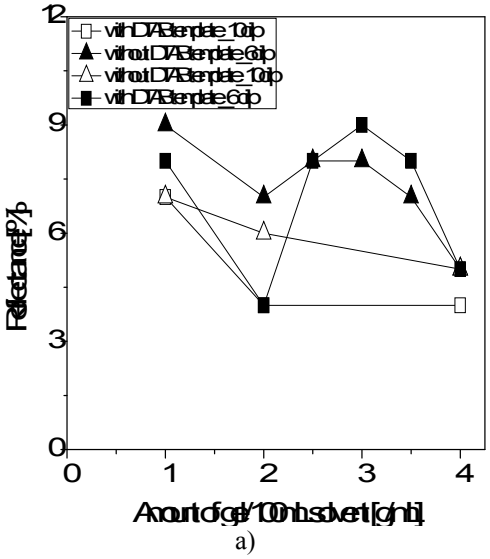

a)

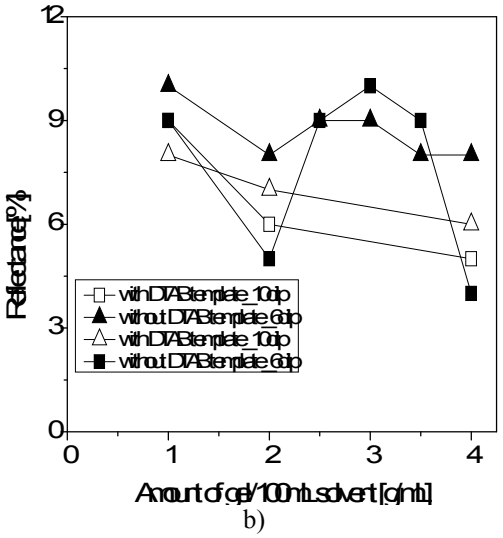

b)

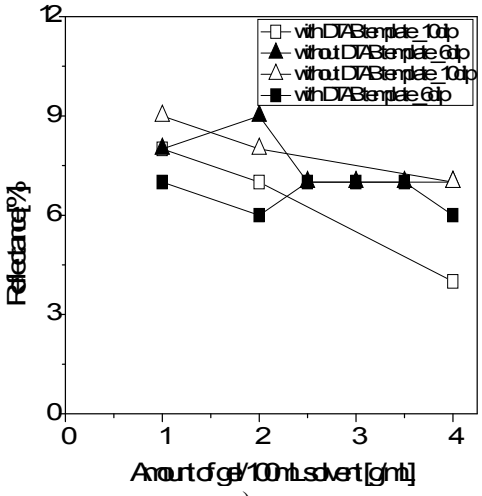

c)

Fig. 6. *Maximum reflectance of the silica thin films, within the spectral range: (a) UV, λ = 250…300 nm; (b) VIS, λ = 300…800 nm; (c) NIR, λ = 800…2000 nm*

The reflectance (R%) values are presented in Fig. 5. The results show that the films obtained using DTAB always have the lowest R% values and this could be corroborated with the lower roughness values, this lower multiple reflections.

This effect is more evident for the homogeneous presented in Fig. 5b and c. As in the case of the transmittance analyses, the best samples are those obtained using 2g gel/100mL solvent, and among these, the sample obtained with DTAB performs best.

4. Conclusions

Thin films of silica used in developing coloured glazing were obtained by using sol-gel synthesized nanoparticles and by the direct gel deposition, at various concentrations, by dipping. The results show that the number of dipping sequences and the gel concentration need to be inter-correlated, for obtaining smooth, low roughness films, with hydrophilic properties. The addition of a surfactant DTAB can improve tuning the optical properties and support optimization.

The silica thin film with good optical properties such as high transmission, low reflectance and low roughness obtained by sol–gel dip – coating methods is SiO_2 1g DTAB_6 dipping dispersed in 50 mL ethanol: water (1:1v/v) mixture.

Acknowledgements

We hereby acknowledge the structural founds project PRO-DD (POS-CCE, O.2.2.1., ID 123, SMIS 2637, no. 11/2009) for providing the infrastructure used in this work and the PNII-Cooperation project EST IN URBA, contract no. 28/2012 financed by UEFISCDI which supported the latest research here by presented.

References

[1]. Soteris A. Kalogirou - *Solar thermal applications*, Progress in Energy and Combustion Science, 30, 2004, p. 231-295.

[2]. Patrice Pinel, Cynthia A. Cruickshank, Ian Beausoleil-Morrison, Adam Wills - *„A review of available methods for seasonal of solar thermal energy in residential applications*, Renewable and Sustainable Energy Reviews, 15, 2011, p. 3341-3359.

[3]. Christian Carboni, Roberto Montanari - *Solar thermal systems: Advantages in domestic integration*, Renewable Energy, 33, 2008, p. 1364-1373.

[4]. Helena Gajbert - *Solar thermal energy systems for building integration*, Ph.D Thesis, 2008.

[5]. Stefan Martin, Virginie Hody-Le Caer, Martin Joly, Iris Mack, Peter Oelhafen, Jean-Louis Scartezzini, Andreas Schuler - *Reactively sputtered coatings on architectural glazing for coloured active solar thermal facades*, Energy and Buildings, 68, 2014, p. 764-770.

[6]. Alessandro Cannale, Francesco Fiorito, Michele Manca, Giovanni Tortorici, Roberto Cingolani, Giuseppe Gigli - *Multifunctional bioinspired sol – gel coatings for architectural glasses*, Building and Environment, 45, 2010, p. 1233-1243.

[7]. F. Garcia, F. Yuberto, J. P. Hogado, J. P. Espinos, A. R. Gonzales Elipe, T. Girardeau - *SiO_2/TiO_2 thin films with variable refractive index prepared by ion beam induced and plasma enhanced chemical vapor deposition*, Thin Solid Films, 500, 2006, p. 19-26.

[8]. J. Boudaden, P. Oelhafen, A. Sculer, C. Roecker, J.-L. Scartezzini - *Multilayered Al_2O_3/SiO_2 and TiO_2/SiO_2 coatings for glazed colored solar thermal collectors*, Solar Energy Materials & Solar Cells, 89, 2005, p. 209-218.

[9]. Chainhung Huang, Hsunling Bai, Yaoling Huang, Shuling Liu, Shaoi Yen, Yaohsuan Tseng - *Synthesis of Neutral SiO_2/TiO_3 Hydrosol and Its Application as Antireflective Self-Cleaning Thin Film*, International Journal of Photoenergy, 10, 2012, p. 1-8.

[10]. S. Permpoon, M. Houmard, D. Riasetto, L. Rapenne, G. Berthome, B. Baroux, J. C. Joud, M. Lauglet - *Natural and persistent superhydrophilicity of SiO_2/TiO_2 and TiO_2/SiO_2 bi-layer films*, Thin Solid Films, 516, 2008, p. 957-966.

[11]. Longqiang Ye, Yulu Zhang, Xianxiang Zhang, Teng Hu, Rui Ji, Bin Ding, Bo Jiang - *Sol – gel preparation of SiO_2/TiO_2/SiO_2-TiO_2 broadband antireflective coating for solar cell cover glass*, Solar Energy Materials&Solar Cells, 111, 2013, p. 160-164.

[12]. H. Miyazaki, T. Goto - *SiO_X films prepared using RF magnetron sputtering with a SiO target*, Journal of Non-Crystalline Solids, 352, 2006, p. 329-333.

[13]. Y. He, L. Bi, J. Y. Frug, Q. L. Wu - *Properties of Si – rich SiO_2 films by RF magnetron sputtering*, Journal of Crystal Growth, 280, 2005, p. 352-356.

[14]. M. Dudita, L. M. Manceriu, M. Anastasescu, M. Nicolescu, M. Gartner, A. Duta - *Coloured TiO_2 based glazing obtained by spray paralysis deposition for solar thermal applications*, Ceramics International, 40, 2014, p. 3903-3911.

[15]. S. Kirtay, E. Oktay, V. Gunay - *Glass strengthening SiO_2-TiO_2 organically modified silica coating*, Thin Solid Films, 515, 2006, p. 2145-2152.

[16]. Hiroaki Uchiyama, Ryosuke Sasaki, Hiromitsu Kozuka - *Evaporation-driven self organization of photoluminiscent organic dye-doped silica-poly (vinylprrolidone) hybrid films prepared by low-speed dip-coating*, Colloid and Surfaces A: Physicochem. Eng. Aspects, 453, 2014, p. 1-6.

THE ANNALS OF "DUNAREA DE JOS" UNIVERSITY OF GALATI
FASCICLE IX. METALLURGY AND MATERIALS SCIENCE
N^0. 2 – 2014, ISSN 1453 – 083X

EFFECT OF ZnO NANOPARTICLES ON THE ANTICORROSION PROPERTIES OF EPOXY COATING[1]

Viorel PANAITE*[1,2], Viorica MUȘAT[1]
[1]Centre of Nanostructures and Functional Materials, Faculty of Materials and Environment Engineering, "Dunarea de Jos" University of Galati, 47 Domneasca Street, RO-800008, Galati, Romania,
[2]Bureau Veritas Romania Controle International Galati, Brailei Street, 165b, RO-800310, Galati, Romania
*Corresponding author
e-mail: panaite_viorel@yahoo.com

ABSTRACT

Homogeneous epoxy coating obtained by embedding ZnO nanoparticles (≤50 nm) in the epoxy matrix, was applied on Grade A naval steel substrates by dip-coating method. The morphology and microstructure of the coatings were characterized by optical microscopy, scanning electron microscopy with electron diffraction spectroscopy (SEM-EDS) and X-ray diffraction (XRD) analysis. The effect of nanoparticles on the corrosion resistance of the hybrid coatings was investigated by potentiodynamic polarization method. The coated steel samples were electrochemically monitored over the 30 days of immersion in 5 wt.% NaCl solution. The incorporation of a small amount of ZnO nanoparticles (1 wt.%) has a beneficial effect, significantly improving the anticorrosion behavior of coating in terms of polarization resistance and corrosion rate, parameters estimated from Tafel curves.

KEYWORDS: ZnO nanoparticles, epoxy coating, Tafel curves, corrosion parameters

1. Introduction

Epoxy based coatings have been used for a long time and appear to be the most convenient method for preventing corrosion and fouling of steel surfaces, structures which work in very severe conditions. Generally, epoxy coatings reduce the corrosion of a metallic substrate subject to an electrolyte, in two ways: they act as a physical barrier layer against the ingress of a deleterious species; second, they can serve as a reservoir for corrosion inhibitors to aid the steel surface in resisting to the attack initiated by aggressive species [1]. Unfortunately, the epoxy coatings have susceptibility to damage by surface abrasion and wear [2, 3] and also they show poor resistance to the propagation of cracks [4].

The defects appeared on coating surface can act as pathways, accelerating the ingress of water, oxygen and chloride anions onto metallic substrate. Being hydrophilic in nature, the epoxy coatings have large volume shrinkage upon curing and can absorb water from surroundings [5, 6], leading to the increasing of the number of pores and crevices, defects that create corrosion products.

The barrier features of epoxy coatings can be enhanced by the incorporation of nanosized inorganic filler particles, dispersed within the epoxy matrix, to form an epoxy based nanocomposite.

Thereby, the following benefits can be obtained:

- improving of the integrity and durability of coatings by dispersion of fine particles in the cavities of epoxy matrix [7-9].
- preventing epoxy disaggregation, obtaining a more homogeneous coating, due to the tendency of nanoparticles to occupy small hole defects, interconnecting more molecules, reducing total free volume and increasing cross-linking density [10-12].
- offering significant barrier properties for corrosion protection [13-14] and reducing the tendency of coating for blistering or delaminating.

[1] Papers presented at the second edition of the Scientific Conference of Doctoral Schools from "Dunarea de Jos" University of Galati, CSSD-UDJG 2014, Galati, May 15-16, 2014.

In this paper, we present the effect of ZnO nanoparticles on the surface morphology and anticorrosion parameters of epoxy coatings for better understanding the mechanisms through which nanoparticles interact with epoxy matrix, for obtaining coatings with high performances in the corrosion protection of steel.

2. Experimental details

2.1. Materials

The epoxy resin, the hardener and the solvent used for coating deposition, commercially known as DER 353, I 3100 and D 309 respectively, were obtained from S.C. "Policolor" S.A. (Bucharest). The DER 353 liquid epoxy resin is an aliphatic glycidyl ether modified bisphenol A/F based epoxy resin, whereas I 3100 hardener is a polyaminoamidic hardener. ZnO nanoparticles with diameter below 50 nm were purchased from Sigma Aldrich (Steinheim, Germany).

Sodium chloride (NaCl) used for corrosion test was purchased from S.C. Silal Trading S.R.L. (Bucharest). As substrates were used rectangle steel samples (50x20 mm) of grade S235JR+AR according to EN 10025-2004 with the following composition: 0.12% C, 0.48% Mn, 0.015% Si, 0.013% P, 0.006%S, 0.039% Al, 0.016% Cu, 0.029% Cr, 0.024% Ni, 0.001% V, 0.003% Mo, 0.001% Ti, 0.001% Nb and Fe.

2.2. Sol preparation and coating deposition

The hybrid sols were prepared in two steps. In the first step was prepared the epoxy precursor solution with a weight ratio of 1.6:1 epoxy resin to hardener. To the obtained solution were added ZnO nanoparticles (1 wt.%) under energical stirring (1400 rpm) and sonnication. Before the deposition of coatings, the steel substrates were cleaned with acetone, sand-blasting to the grade "Sa 2½" and finally immersed in acetone and dried. To remove the microparticles remained on the surface after sand-blasting, the substrates were sonicated in acetone for 10 minutes.

The coatings were deposed by dip-coating technique, using a home-made dip-coater. After each layer deposition, the samples were kept at room temperature for 30 min, placed in an oven (Model FN 055 Nüve) at 90ºC for 30 min and then again at room temperature for 30 min.

In order to compare the effect of the nanoparticles, unmodified epoxy coating (*type I*) and ZnO-modified epoxy coating (*type II*), with approximately the same thickness, around 5 0µm, have been prepared.

2.3. Characterization of coatings

The film thickness (Dry Film Thickness - DFT) was measured by a nondestructive testing method, using a 345 type Elcometer device.

The surface morphology and chemical composition of the coatings were analyzed by Scanning Electron Microscopy with Electron Diffraction Spectroscopy (SEM-EDS) using a Zeiss EVO MA 15 model microscope. *The anticorrosive behaviour* of the nanocomposite coatings was investigated by potentiodynamic weak polarization method. The samples were kept immersed in corrosive solution (5 wt.% aqueous NaCl solution) over the 30 days and the measurements of corrosion parameters were carried out periodically using Voltalab PGP 201 Radiometer Analytical equipment, with three electrodes: the epoxy coated steel sample served as the working electrode, whereas the counter electrode and the reference electrode were used a platinum plate and Ag/AgCl, respectively. A special cell assures the reproducibility of the experimental parameters, especially the distances between electrodes and the free sample surface (0.5024 cm^2) in contact with the corrosive solution. The steel was polarized around its corrosion potential, in general in the potential range of -1000 mV÷ +200 mV by a direct current (DC) signal, at a scan rate of 2 mV/s. The results were processed with the VoltaMaster software application-version 4, using the following experimental parameters: diameter of the free surface of the sample (8 mm), solution exposed surface aria (50.24 mm^2), steel sample density (7.8 kg/dm^3) and iron valence (2).

3. Results and discussion

3.1. Structure and morphology

Optical top-view images of the investigated samples are shown in Figure 1, which indicates that the cured epoxy coating has a relatively homogeneous morphology, without cracks (Figure 1a) and the ZnO modified epoxy coating is slightly rough and apparently showed no sign of nanoparticles agglomeration (Figure 1b). *Topographic analysis* of deposited films was realized by the technique of obtaining and overlapping of three-dimensional imaging (Figure 2). One can observe that simple epoxy coating has a smaller surface roughness than the nano-ZnO modified epoxy coating, thing that can be explained by the presence of a higher number of layers deposited. In Figure 3 are shown SEM images of the surface of nano-ZnO modified epoxy coating (Figure 3a) and chemical EDX analysis on the selected area (Figure 3b); one can observe the presence of some agglomeration of nanoparticles

inside the coating, but no crack. The results of elemental EDX analysis in the area marked are displayed in Figure 4. Although SEM image of agglomerated nanoparticles is observed, EDX mapping on the same area shows a uniform distribution of zinc and oxygen, demonstrating a good dispersion of ZnO nanoparticles inside the composite coatings.

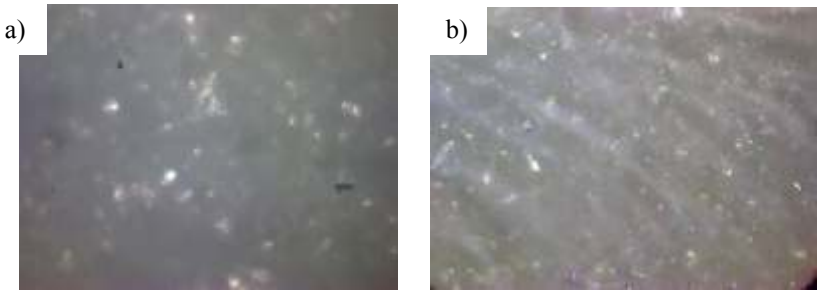

Fig. 1. *Optical micrographs of: simple epoxy coating (type I) (a); nano-ZnO modified epoxy coating (type II) (b) (magnification 12.5x8x)*

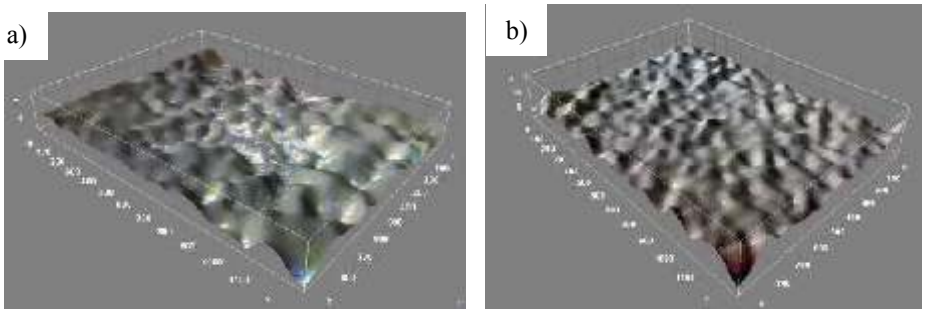

Fig. 2. *3D image of: simple epoxy coating (type I) (a); nano-ZnO modified epoxy coating (type II) (b)*

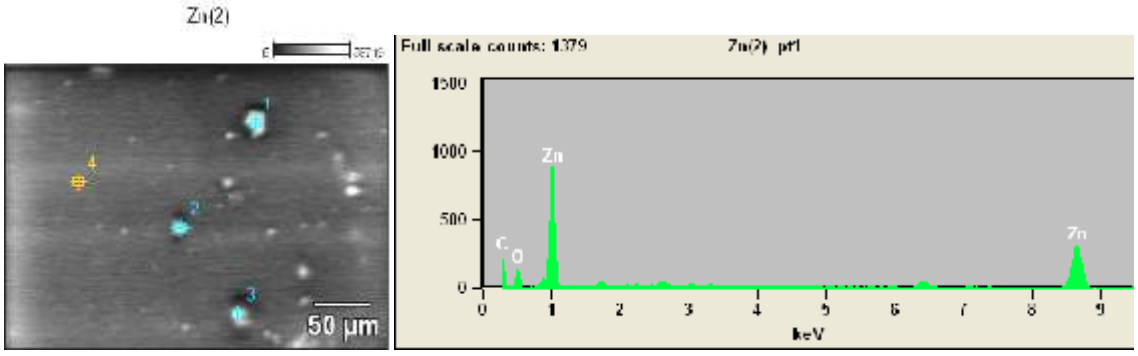

Fig. 3. *SEM image of nano-ZnO modified epoxy (type II) coating (a); chemical analysis specific to region 1 (b)*

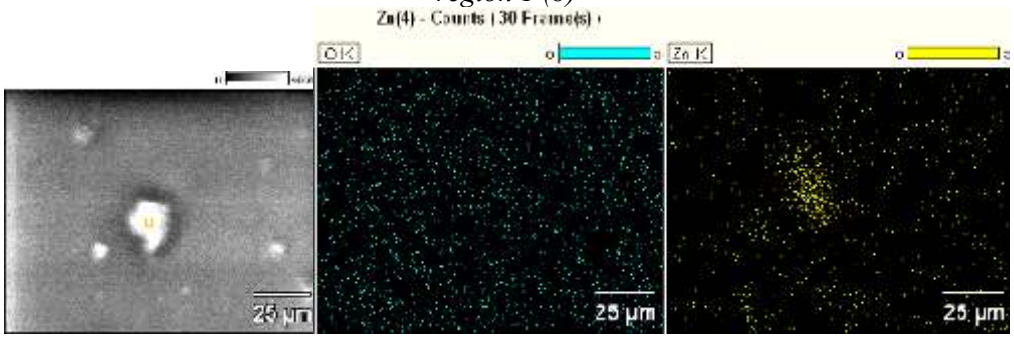

Fig. 4. *Elemental contents of oxygen and zinc mapped by EDX on an area of the nano-ZnO modified epoxy coating (type II)*

The film thickness (DFT)

The medium values obtained for thickness of two epoxy coatings, unmodified (*type I*) and modified with ZnO nanoparticles (*type II*) were of 43 µm and 50 µm, respectively.

3.2. Effect of nanoparticles on the corrosion resistance of the coated steel

The experimental corrosion parameters (corrosion potential, corrosion current, polarization resistance and instantaneous corrosion rate) of the steel samples coated with metal oxide-epoxy nanocomposite were estimated from Tafel curves. Figure 5 shows the temporal evolution of instantaneous corrosion rate (Figure 5a) and polarization resistance, Rp, (Figure 5b) of the steel samples coated, during more than 30 days of immersion in 5 wt.% NaCl solution.

One can notice that both diagrams show that in case of simple epoxy coating there is a continuing trend of increasing instantaneous corrosion rate (Figure 5a), respectively of decreasing polarization resistance (Figure 5b).

This could be attributed to the fact that in the case of this type of coating, once activated the destruction of physical barrier, the corrosion process continuously develops.

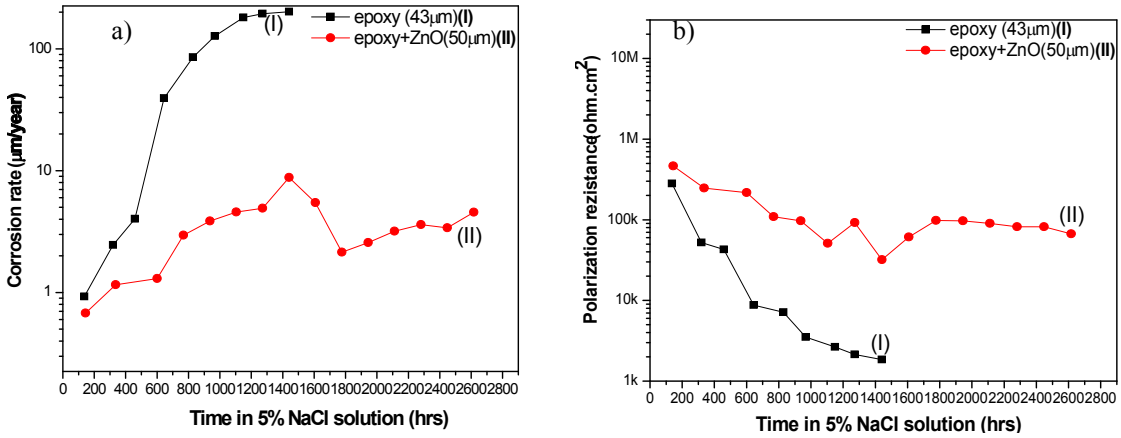

Fig. 5. *Time evolution of: corrosion rate (a) and polarization resistance (b), of epoxy-coated steel in 5 wt.% aqueous NaCl solution, at different time of immersion*

In case of nano-ZnO modified epoxy coating, for both diagrams in Figure 5 one can distinguish three steps: from the beginning to around 800 hours of immersion (Step I) in which the corrosion rate grows up in an accelerated way from 800 to about 1400 hours of immersion (Step II) in which there is a lower growth of instantaneous corrosion rate and the last (Step III) in which the corrosion rate decreases or it is maintained within close limits. Consequently, the trend of decreasing is similar in case of polarization resistance. The incorporation of a small amount of ZnO nanoparticles (1 wt.%) into the epoxy coating significantly reduced the corrosion rate of the epoxy-coated steel over the 30-day immersion in 5 wt.% NaCl solution, by 2 to 40 times, after 1272 hours and consequently leads to the adequate improving corrosion resistance of the epoxy-coated, by 2 to 43 times, for the same period of immersion.

The tendency of nano-ZnO modified epoxy coating to keep a constant good level for anticorrosion resistance on long-term (until 2600 hours of immersion) could be explained both by the occurrence of corrosion products that can slow the corrosion process but also by the beneficial presence of ZnO nanoparticles which can act as reservoir for corrosion inhibitors of the steel surface in resisting to the attack of aggressive species.

4. Conclusions

ZnO nanoparticles were successfully dispersed in epoxy resin matrix at a concentration of 1%. The samples obtained after dipping the steel substrate into the hybrid sol show smooth surface and compact coating, a good compliance and adherence to the substrate, no cracks and no boundaries between the deposited layers. The electrochemical monitoring over the 30 days of immersion in 5 wt.% NaCl aqueous solution suggested the beneficial role of nanoparticles in significantly improving the corrosion resistance of the coated steel. For future research, it is important to investigate ways to improve the dispersion of a mix of nanoparticles to provide different features of the epoxy coating, to increase the content of ZnO nanoparticles and the potential application of the nanoparticles as reservoirs of corrosion inhibitors.

References

[1]. D. M. Yebra, S. Kiil, K. D. Johansen - Prog. Org. Coat., 50, 2004, p. 75.
[2]. B. Wetzel, F. Haupert, M. Q. Zhang - Compo. Sci. Technol., 63, 2003, p. 2055.
[3]. M. Q. Zhang, M. Z. Rong, S. L. Yu, B. Wetzel, K. Friedrich - Macromol. Mater. Eng., 287, 2002, p. 111.
[4]. S. Yamini, R. J. Young - Polymer, 18, 1977, p. 1075.
[5]. D. Perreux, C. Suri - Compo. Sci. Technol., 57, 1997, p. 1403.
[6]. C. Loos, G. S. Springer - J. Comp. Mater., 13, 1979, p. 131.
[7]. K. Lam, K. T. Lau - Compo.Struc., 75, 2006, p. 553.
[8]. G. Shi, M. Q. Zhang, M. Z. Rong, B. Wetzel, K. Friedrich - Wear, 254, 2003, p. 784.
[9]. Hartwig M. Sebald, D. Putz, L. Aberle - Macromol. Symp., 221, 2005, p. 127.
[10]. F. Dietsche, Y. Thomann, R. Mulhaupt - J. Appl. Polym. Sci., 75, 2000, p. 396.
[11]. N. Huong - *Improvement of bearing strength of laminated composites by nanoclay and Z-pin reinforcement*, PhD. Dissertation, University of New South Wales, Australia, 2006.
[12]. O. Becker, R. Varley, G. Simon - Polymer, 43, (16), 2002, p. 4365.
[13]. L. H. Yang, F. C. Liu, E. H. Han - Prog. Org. Coat., 53, 2005, p. 91.
[14]. S. V. Lamaka, M. L. Zheludkevich, K. A. Yasakau, R. Serra, S. K. Poznyak, M. G. S. Ferreira - Prog. Org. Coat., 58, 2007, p. 127.

THE ANNALS OF "DUNAREA DE JOS" UNIVERSITY OF GALATI
FASCICLE IX. METALLURGY AND MATERIALS SCIENCE
N^0. 2 – 2014, ISSN 1453 – 083X

OBTAINING AND STUDYING TENSILE STRENGTH FOR NON-PRECIOUS ALLOYS BASED COBALT

Mirabela Georgiana MINCIUNĂ, Petrică VIZUREANU, Dragoş Cristian ACHIŢEI, Viorel GOANȚĂ, Ștefan TOMA, Mădălina Simona BĂLȚATU
Gheorghe Asachi Technical University from Iaşi
e-mail: mirabela.minciuna@yahoo.ro

ABSTRACT

This paper presents aspects of obtaining non-precious dental alloys of Co-Cr-Mo alloys system and experimental tests to determine tensile strength, carried on standard flat specimens.

KEYWORDS: non-precious alloys, medical applications, casting, electrical discharge

1. Introduction

The use of metals and alloys in medicine applications has been known science ancient times, when they were designed and manufactured artificial substitutes that were implanted in the mouth.

Metals were used to fix the replacement teeth on the original teeth, with ligature wire from silver or gold, technique described by Hippocrates in the treatise "Epidemia" [1].

The oldest complete denture was made in Japan and it was found at Ganjyoji Temple (Kii Province). It was made of Buxus wood [2].

In 1932 was obtained the first alloy from Co-Cr-Mo alloys system, and since that time, the conditions of use of materials in medicine have been determined by three main factors [3]:

- Increasing the share of use of non-precious dental alloys due to the increasing price of noble alloys;
- Ongoing improvements made in the creation of new dental materials with special properties;
- Continuously changing manufacturing technology prosthetic devices.

The developments that we see in medicine are due to specialists in areas such as materials engineering, mechanical engineering, chemistry, physics, electronics and so on, thus making the complex links between these scientific fields that have the common goal to improve the people's health [4].

Co-Cr-Mo alloys referred to as "stellite" system are cobalt-based alloys resistant to wear, abrasion, corrosion, oxidation and erosion.

At higher temperatures up to 800°C, they keep their properties including high hardness and are less complex than nickel - based alloys [5].

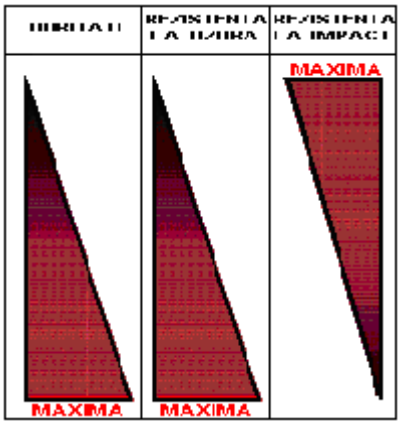

Fig. 1. *Values of properties of the alloys of cobalt* [6]

Cobalt-based alloys are difficult to manufacture and therefore their use has been limited but constant research has led to the development of specific casting methods [7].

Co-Cr-Mo system for casting alloys are widely used for making various devices surgically implanted in the body, their use always continues to extend [8].

Since 1949 it is estimated that over 80% of partial dentures were made of Co-Cr-Mo alloy system, and by 1969, over 87% [9].

Currently, almost all the metal plates of partial dentures are made of Co-Cr-Mo alloy systems.

2. The material used in experimental research

The material used in the research is a commercial alloy Co-Cr-Mo system, which belongs to the class of non-precious dental alloys, for medical applications.

The chemical composition of the alloy according to product data sheets is shown in Table 1.

Table 1. *The concentrations of the alloying elements for the Co-Cr-Mo commercial alloy*

Alloying element	**Co**	**Cr**	**Mo**	**C**	**Si**	**Mn**
% Mass	65	29	5	0.4	0.35	0.25

The materials used to produce these alloys of high purity and are appropriately selected in terms of chemical composition and grain size analysis.

The size of the ingots are chosen such that to be executed in well-positioned in the wells with water-cooled copper plate of the plant.

Mechanical characteristics for the studied alloy are the described in Table 2.

Table 2. *Mechanical characteristics for the studied alloy*

Yield stength	$R_{p0,2}$	560 N/mm^2
Tensile strength	R_m	760 N/mm^2
Elongation	A	3 %
Modulus of elasticity	E	219000 N/ mm^2
Hardness	HB	380
Density		8.26 g/cm^3
Melting range		1330…1400 ^{o}C

The process aims to achieve rapid melting to a maximum allowable current.

In terms of melting intensities we took into account a number of metallurgical considerations related to gas metal purification and non-metallic inclusions. The melted cobalt-based ingots have a good chemical and structural homogeneity [13].

3. The technological flow for the obtaining of cobalt-based alloys

The obtaining of material, submitted to research, was performed using arc remelting facility, MRF vacuum ABJ 900, followed by remelting of the alloy for 7 times for refining and homogenizing the structure in the same installation.

Work parameters for RAV installation are the following:

- Pressure on site 10^{-4} mbar;
- "Flooding" of the working chamber with argon purity 99.99%, which carries out an on-site oxygen content of approx. 60 ppm;
- Melting power: 55 kVA;
- Melt flow of 650 A.

Advantages of this furnace are:

- High temperatures are reached in just a few seconds;
- Creating alloys with a uniform composition due to the strong stirring effect realized by an electric arc melting;
- Possibility of mixing the components with different melting temperatures.

Fig. 2. *Remelting installation with electric arc, under vacuum, type MRF ABJ 900*

During the melting and casting operations can be achieved an atmosphere of vacuum or inert gas to prevent reaction with oxygen or nitrogen in the furnace atmosphere.

The technological flow of obtaining cobalt-based alloys consisted of the following steps:

- Preparation of commercial CoCrMo alloy;
- Degreasing volatile organic solvents to remove the surface grease, which could affect the quality of the protective atmosphere inside the kiln and the quality of the alloy obtained by casting process;
- Weighing "ingots" of commercial Co-Cr-Mo alloy under the charge calculation;
- Loading of raw materials in the crucible furnace;
- A vacuum system and achieving controlled argon atmosphere inside the melt;
- Batch melting by the heat of the arc, followed by remelting for 7 times;
- Extraction of molded samples obtained.

4. Commercial Co-Cr-Mo alloys remelting

This phase included the remelting of commercial alloy, from Co-Cr-Mo system. Melting was performed by using the arc created between the tungsten-thorium electrode and metal charge placed in the wells of different sizes, formed in the base made of copper and cooled with water.

Co-Cr-Mo alloy system has been introduced under the form of "ingot", which has been melted by the heat from the electric arc. To ensure a high homogeneity of the alloys, the load was remelted at least 7 times with successive turns of micro-ingot formed in each well after each remelting.

Fig. 3. *Commercial Co-Cr-Mo alloy prepared during elaboration process*

The alloys obtained were classified by sample weight, keeping weight to a quasi-constant value in each category.

Fig. 4. *Melting of commercial Co-Cr-Mo alloy*

After solidification of the commercial alloy, from Co-Cr-Mo system, we obtained five samples of various weights and shapes (Figure 5).

Fig. 5. *Commercial Co-Cr-Mo alloy after solidification – casting samples*

The structure of remelted samples is compact, uniform, with dendrites oriented in direction of the sense thermal gradient.

Concentric zonal segregation showed that a difference in grain occurs at melting with higher intensities. To limit the formation of casting losses at the end of ingot, remelting has dwindled towards the end of the current intensity.

To calculate the metal load (load dosing) levels were taken into account theoretical assimilation of the elements melt and vaporization any losses. The metallurgical process takes place in vacuum or controlled atmosphere of argon.

Evaporation losses are reduced because "ingots" do not contain impurities, development performed in controlled atmosphere of vacuum and argon.

Melting occurred evenly and smoothly throughout its duration and at the end of the process, with a gradual reduction for the current intensity and in the work chamber was introduced an inert gas (argon), until the pressure reached about 10^{-4} mbar.

After elaboration of the first batch molded samples were obtained various sizes. Batch size has been chosen so that, after each sample, preparation can be used for different tests.

Table 2. *Calculation of charges for commercial alloy from Co-Cr-Mo system*

Nr.	Charge	Co	Cr	Mo	Ni	Si	Mn	Fe	W	S	P
	[g]										
1	171.34	107.410	45.924	10.217	4.974	1.371	0.723	0.550	0.195	0.009	0.002
2	105.48	66.123	28.272	6.290	3.062	0.844	0.445	0.339	0.120	0.005	0.001
3	253.78	159.090	68.021	15.133	7.367	2.030	1.071	0.815	0.289	0.013	0.003
4	72.36	45.361	19.395	4.315	2.101	0.579	0.305	0.232	0.082	0.004	0.001
5	33.56	21.038	8.995	2.001	0.974	0.268	0.142	0.108	0.038	0.002	0.000

5. Samples cutting by electric discharge

Processing of specimens, required for this study, was done by electric discharge and the removal of excess material is based on the erosive effects of electric discharges impulse, primed repeatedly between object processing and electrode.

Processing plant Japax electro JAPTI (Fig. 6) is composed of: machine itself, the water basin with a capacity of 120 liters and control panel.

Fig. 6. *Japax Japt with wire cutting machine, to cut the samples*

During the electric discharge processing, dielectric (de-ionized) water is heated and thus it pollutes the particles collected, with the possibility of short circuits.

To remove these unwanted phenomena, the plant has in its system cooling and filtering the dielectric and washing the work gap.

6. Tensile tests

We used tensile testing because we can determine many mechanical properties that allow us to make an accurate assessment of the behavior of the material that will be used in the application [15].

To highlight the differences between the various parameters obtained as a result of tensile testing, investigations were conducted on flat specimens with a total length of 54 mm in accordance with specific standard tests.

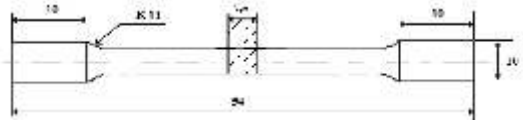

Fig. 7. *Flat sample which used tip tensile test [16]*

Determination of mechanical testing was performed on Instron 3382 machine, computer-aided record tensile curves being automatically made according to the established protocol traction experiment, monitored by the traction machine program.

Fig. 8. *Samples after tensile test*

The tests were carried out at ambient temperature. Curves of tensile stress (MPa) were plotted function of tensile strain (%).

For each alloy were performed 4 tensile tests to reveal better mechanical properties and to obtain the most accurate results.

Table 3 contains the values provided by the traction machine program for the mechanical properties of commercial CoCrMo alloy samples.

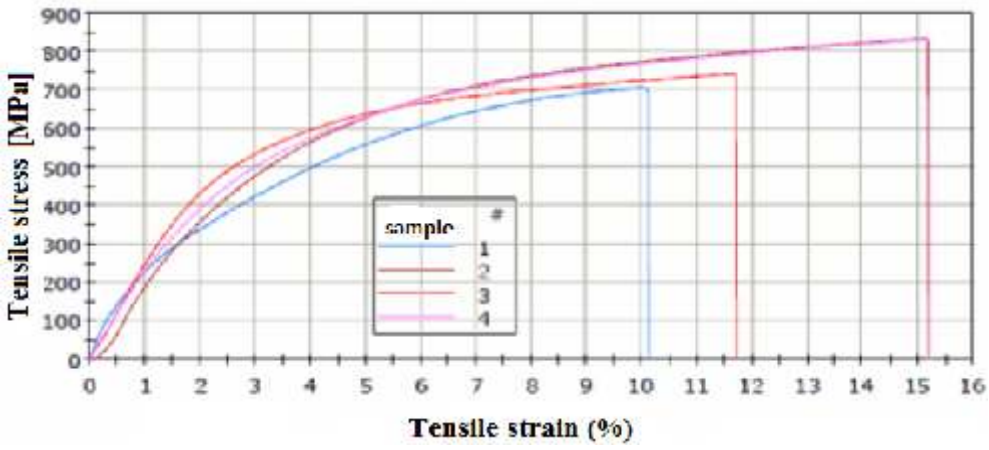

Fig. 8. *Tensile stress vs Tensile strain, curves obtained for commercial Co-Cr-Mo alloy*

Table 3. *Mechanical properties measured by tensile test for Co-Cr-Mo alloy*

Tensile stress vs. Tensile strain	Maximum load	Tensile strain at Break (Standard)	Modulus (E-modulus))	Tensile stress at Tensile Strength	Tensile stress at Yield (Offset 0.2 %)
	[N]	[%]	[MPa]		
CoCrMo (1)	7079.35	10.12	20059.03	707.60156	281.17
CoCrMo (2)	8343.83	15.17	21644.17	833.73578	358.56
CoCrMo (3)	7436.92	11.71	23809.56	742.39044	428.73
CoCrMo (4)	8316.70	15.20	20900.89	830.25531	386.32

The Co-Cr-Mo alloy system shows a linear behavior up to rupture. Given the behavior of the alloy, it belongs to the category of fragile materials which are characterized by the following traits:

- ❖ Rupture occurs suddenly and without prior plastic deformation;
- ❖ Characteristic tension-strain (σ-ε) is linear;
- ❖ They do not distinguish a deviation from linearity of the characteristic curve which means that plastic deformations, if they exists, are limited;
- ❖ As the elongation is observed that there is a greater dispersion of this size, probably due to sample processing defects;
- ❖ Maximum tension for Co-Cr-Mo alloy system is 833.73 [MPa]. At this level of deformation tension is relatively small, which implies that all deformation was elastic rupture, breaking effort with a maximum of 428.73 [MPa];
- ❖ Rupture occurred due to crack propagation from a preexisting defect and not due to displacement, dislocation accumulation and agglomeration planes additional obstacle;
- ❖ The examination and cross-sectional area measurement, after fracture, pointed out that they remain plane and perpendicular to the direction of application. The crystallographic plans do not change its original shape and very little his size;
- ❖ This aspect of the results, after fracture surfaces, is characteristic to the brittle behavior of materials;
- ❖ The modulus of elasticity was deduced from the slope of the voltage curve approximation - specific strain (σ - ε), given the linearity of the curve up to breaking;
- ❖ Thus, Co-Cr-Mo alloy system for the maximum elastic modulus was 23809.56 [MPa].

7. Conclusions

If Co-Cr-Mo alloys are commonly used in medicine, their detailed study has an important role in determining the structural stability, size and variation of properties in different processing conditions.

The study of the mechanical properties of the system of Co-Cr-Mo alloys was performed using dedicated laboratory tests to assess their potential use as biomaterials for medical applications.

Depending on the properties and areas of application, the study continues as cobalt -based alloys and their production technologies ensure the development of new applications of scientific and engineering requirements of the present time.

The modulus of elasticity is a controversial matter. It is a measure of the elastic deformation and is inversely proportional to its amplitude.

A high modulus of elasticity, the minimum deformation means and the forces are taken to full bridge abutments, and as such will be overworked.

On the other hand, a low modulus of elasticity means and the high deformations under the action of forces can lead to mobilization of abutments.

The modulus of elasticity of the alloy based on cobalt 200-234 GPa is two times higher than that of the noble alloys, which gives a certain advantage and aesthetic designs can be achieved at the same time soft and rigid.

As the modulus of elasticity is higher, with both the mechanical parts made from Co-Cr-Mo alloys, can be made thinner.

References

[1]. Alsaran A., Bayrak O., Celik A., Kaymaz, A. F. Yetim - Surf. Coat. Technol., 2008, 202, p. 2433.
[2]. Blatter A., Eschler Luthy H. P. Y., Reclaru L., Susz C. - Biomaterials, 26, 2005, p. 4358-4365.
[3]. Ghiban B. - *Structural aspects of cobalt-base alloys for biomedical implants*, Ovidius University Annals of Mechanical Engineering, vol. 3, nr. 3, 2001.
[4]. Bugliosi S., Faga M. G., Maina G., Spriano S., Verne E. - *Surface treatment on an implant cobalt alloy for high biocompatibility and wear resistance*, Wear 259, 2005, p. 919-925.
[5]. Craig R. G., Powers J. M. - *Restorative Dental Materials*, 11thed. Mosby, 2002, p. 480-492.
[6]. Burny F., Donkerwolcke M., Muster D. - *Biomaterials education: a challenge for medicine and industry in the late 1990s*, Mater. Sci. Eng. A 199, 1995, p. 53-59.
[7]. Castano O., Michiardi A., Navarro M., Planell J. A. - *Biomaterials in orthopaedics*, J. R. Soc. Interface 5, 2008, p. 1137-1158.
[8]. Chen Y., Hsu R. W., Huang C., Yang C. - *Electrochemical corrosion studies on Co–Cr–Mo implant alloys*, Mater. Chem. Phys. 93, 2005, p. 531-538.
[9]. Dowson D., Neville A., Yan Y. - Tribology International, 40 2007, p. 1492.

[10]. Devine T. M., Wulff J. - Journal of Biomedical Materials Research 9, 1975, p. 151.
[11]. www.eramet.ro.
[12]. Geantă V., Voiculescu I., Ştefănoiu R., Chiriţă I. - *Obtaining and Characterization of Biocompatible Co-Cr as Cast Alloys*, Key Engineering Materials vol. 583, 2014, Trans Tech Publications, Switzerland, p. 16-21.
[13]. B. Avitzur, *Metals Forming: Processes and Analysis*, R. E. Krieger Publishing Company, Huntington, New York, 1979.
[14]. L. Zaharia, R. Chelariu, R. Comaneci - *Multiple direct extrusion: A new technique in grain refinement*, Materials Science and Engineering: A, vol. 550, 30 July 2012, p. 293-299.
[15]. L. Zaharia, R. Comaneci, R. Chelariu, D. Luca - *A new severe plastic deformation method by repetitive extrusion and upsetting*, Materials Science and Engineering, vol. 595, 10 February 2014, p. 135-142.

THE ANNALS OF "DUNAREA DE JOS" UNIVERSITY OF GALATI
FASCICLE IX. METALLURGY AND MATERIALS SCIENCE
N^0. 2 – 2014, ISSN 1453 – 083X

RESEARCH ON ABRASIVE WEAR BEHAVIOUR OF LASER CLADDING LAYERS WITH ALUMINUM BRONZE POWDERS

Simona BOICIUC
"Dunarea de Jos" University of Galati, Romania
e-mail: simonaboiciuc@yahoo.com

ABSTRACT

The paper presents the wear behaviour on rotating disk with abrasive paper of laser cladding layers with aluminum bronze powders compared with steel samples and aluminum bronze classically quenched. The hardness and wear mass variation were monitored.

KEYWORDS: laser cladding, aluminum bronzes, powder, injection

1. Introduction

With the rapid growth of laser applications and the reduced cost of laser systems, laser material processing has gained increased importance in a variety of industries. Navy, aerospace, automotive, defence and many other sectors are widely adapting laser technology for welding, cutting and hardening [1].

Laser cladding can be used to good effect in processes which require a high productivity combined with flexibility without compromising quality.

A high and uniform quality with a low heat input makes this process suitable for a wide range of applications in which minimum distortion is desired. Examples of industrial laser cladding applications are [2]: improved wear resistance of bearings, valves, axles, cutting tools and other parts where the working conditions are very severe; improved corrosion resistance; repairing turbine parts, moulds, tools; building up complex geometries.

Laser cladding can be used to improve resistance to wear and corrosion of components in the metallurgical industry.

Laser cladding was defined as a process used to melt a material having different metallurgical properties on a substrate by means of laser beam [3].

Thus it was found that by altering the power density, duration of laser action, feed speed, powder feed speed, granulation and powder density, the complex of physico – mechanical properties within the superficial layers of preset size. Also a good quality of the layers deposited implies lack of cracks, of porosity, good bond with the substrate and a low dilution of the material covering the substrate and minimum roughness [3].

Copper alloys with 9-11% Al features, in addition to high corrosion resistance, good casting and hot forming properties and heat treatment hardening capacity of martensitic quenching and tempering.

Classical quenching consists of [4], heating at temperatures of 980-1000 °C followed by rapid cooling in water. Subsequent tempering to 400-550 °C, has hardening effect. Thus the $CuAl_{10}Fe_4Ni_4$ alloy after quenching from 980 °C in water and tempering to 400 °C, increases its hardness from 170-200 HB to over 400 HB.

In the special Cu-Al alloys there are additions of Fe, Ni, Mn, which change the solubility of aluminum in copper and lead to new phases. Iron polishes granulation and improves mechanical and antifriction properties. In Fe-rich alloys it may occur an intermetallic compound $FeAl_3$ with hardening and embrittlement effect. Nickel and manganese increase corrosion resistance and provide further hardening by solid solution alloying [5-7].

Multilayer deposition of aluminum bronze powders injected onto the laser melted surface has the advantage of making thick layers with uniform chemical composition and properties throughout the section.

The paper presents the wear behaviour on rotating disk with abrasive paper of laser cladding layers with aluminum bronze powders compared to steel samples and aluminum bronze classically quenched.

2. Experimental conditions

For deposition, use was made of powder of bronze with alluminum ,,Rototec Proces FRIXTEC

CASTOLIN U.S.A.", having the following chemical composition: 9.5% Al; 2.2% Fe; rest Cu.

Since the coating with aluminum bronze on the steel support indicated a low quality of the deposited layers geometry (rough surface, thin deposit and micro-cracks), its deposition on a buffer layer of nickel alloy has been experienced and a very good deposition on steel substrate was found.

The Nickel based alloy used in the laser cladding is Ni-Cr-B-Fe-Al with the following chemical composition: 8.9% Cr, 4.5% Fe, 5.1% B 2.4% Al, 0.6% Cu, rest Ni.

The basic material used in the experimental research is steel 1C45, SR EN 10083-1:1994.

Laboratory experiments were conducted on a CO_2 continuous wave system, type 1400 W Laser GT (Romania), with working mass in x-y-z coordinates and computer programming of the working regime, provided with a powder injection system on the melted surface by means of laser, existing in SC UZINSIDERENGINEERING Galaţi.

Laboratory tests used a 1.8 mm diameter laser beam, which made partially overlapping parallel strips. Final thickness of the layer was achieved by superposition of five layers. To determine the optimum deposition regime the added material flow rate was varied, Q, from 53 to 150 mg/s, beam power, P, from 900 to 1200 W, surface scanning speed, v, from 5-7 mm/s and transverse movement step, p, 1 to 2 mm. The nickel alloy buffer layer was deposited by the superposition of two layers, under the following conditions: Q = 53 mg/s, P = 1100 W, v = 7 mm/s, p = 1 - 2 mm. Table 2 shows the experimented working regimes and thickness, h, of the deposits obtained. Deposition regime was characterized by energy density factor K = P / d * v, which ranged within 79.3 ÷ 100 J/mm^2.

The characterization of particles shapes was made on the optic microscope, analyzing the free particles of the powders distributed into a single particles layer, between two glass plates. For the purpose of metallographic analysis, the powder was embedded by cyano-acrylate adhesive and prepared by grinding, polishing and chemical attack with Nital 2% or ferric chloride and examined at optical microscope Olympus BX51M Japan, with digital acquisition of image. To determine the micro hardness of the powder particles micro hardness, apparatus PMT-3 with penetration loading by 100 g was used. Vickers microhardness was calculated according to the SR EN ISO 6507-1:2002 standard. Results are presented as a mean of three measurements.

Microstructural analysis was performed on samples cross-section, perpendicular to the direction of laser processing. The microstructure of the samples was observed by optical microscopy Olympus BX 51 M.

The abrasive wear behavior of laser deposited layers with aluminum bronze powder has been studied according to STAS 9639-81. The method uses a connection of peg/disk friction of class IV-1. The method consists in pressing sequentially, under identical conditions, two samples of dimensions 6.2 x 6.2 mm, one of the material examined deposited by laser and the other from a material chosen for comparison purpose – improved aluminum bronze classically quenched on a rotating disk covered with grinding paper of 120 grains. A mechanism for radial displacement of the tube with 0.5 mm/r provides a spiral movement on the surface of the rotating disk.

A device for implementing a load of 8.387 N ensured perpendicular pressing of the sample on the grinding paper at the pressure of 0.215 N/mm^2. At disk speed of 25 rpm, a number of 131 rotations have provided a length path of 82 m.

3. Results and discussions

Fig. 1. shows the aspect of the powders used. The powders have a spherical shape caused by atomization of gas.

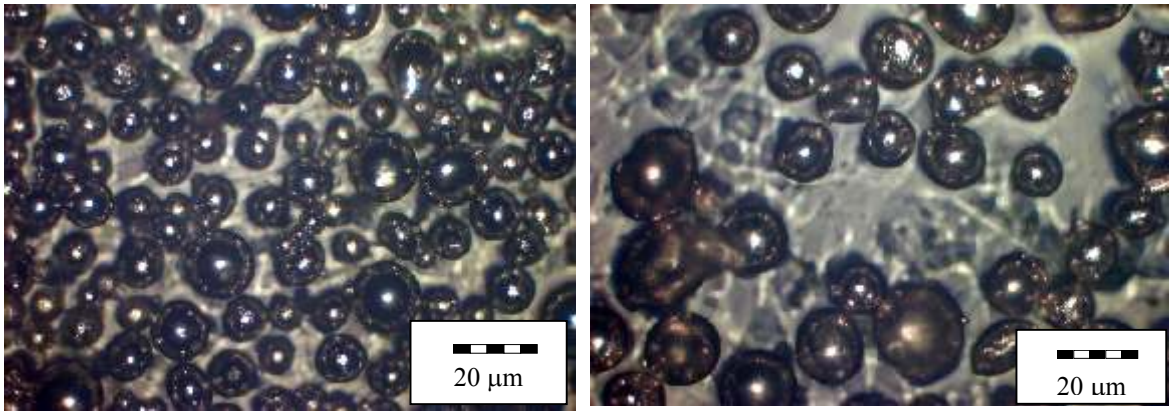

a. ***b.***

Fig. 1. *Aspect of nickel base powder – a, and copper base powder - b*

In the case of nickel base powder, the **microscopic analysis** on samples embedded, polished and attacked with Nital 2% highlights the relative compactness. Particle microstructure consists of numerous intermetallic compounds (NiB, Ni_2B, CrB, Cr_3B_4 and FeB) distributed in a very fine martensitic matrix [3].

Microhardness determined on the polished section of the particles under 100g load was HV0.1 = 9522.2 MPa.

In the case of copper base powder, the microscopic analysis on samples embedded, polished and attacked with ferric chloride reagent highlights the microstructure of particle.

Their structure consist of intermetallic compound Fe - Al distributed in a very fine matrix [4].

Microhardness determined on the polished section of the particles under 100g load was HV0.1 = 2766.5 MPa.

Macroscopic analysis of the laser deposition of aluminum bronze highlights the deposited layer surface quality, thickness and adhesion to the support.

Thick layers with plain surface of cladded layer (Figure 2) may be remarked.

The layer thickness was h = 0.38 – 1.23 mm.

The surface layer is rough (Figure 2) and requires subsequent removal by machining of a relatively large layer.

Macrostructures of the laser deposition of aluminum bronze show a low adhesion to carbon steel support, which can be explained by the poor metal link due to the low solubility of solid copper in iron.

Fig. 2. *Surface of samples cladded by thick layers of aluminum bronze*

The layer thickness strongly depends on the sweeping speed and additional material injection volume. The maximum thickness was found where the sweeping speed was minimum and additional material injection volume was maximum. As laser beam mainly gives the energy required to melt the additional material, the sweeping speed has to be correlated to the additional material flow. The higher the additional material flow, the smaller the sweeping speed which ensures maximum deposited layer thickness.

The decrease in the added material flow rate to 53 mg/s and the use of a buffer layer of nickel alloy, unlimitedly soluble as solid in both iron and copper, increased the adhesion to the steel support and to the deposited layer. The layer quality was significantly improved as this becomes uniform, compact, without solidification shrinkage cracks and with practical applicability. Note that when using a 1.8 mm diameter laser beam on the surface being processed, the max. layer thickness is obtained on a step of the transverse movement of the 1.5 mm sample.

Figure 3 shows the microstructure of the deposited layer for sample with Ni alloy middle layer (Q = 53 mg/s, P = 1100 W, v = 7 mm/s, p = 1 mm, K = 87.30 J/mm^2, h = 0.64 mm). Good support adherence of the deposited layer is visible. At the fusion limit there are no compactness defects or inclusions of metal.

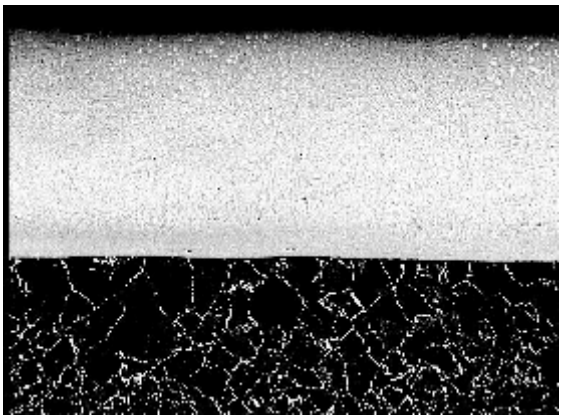

Fig. 3. *Microstructure of the deposited layer with Ni alloy middle layer, general view, x500*

The microstructure of the deposited layer results from melting and ultra-fast solidification of the added material, followed by a partial self-tempering in the overlapping area of the strip deposited i.e sub-layer tempering when an additional layer is deposited.

The microstructure is fine, columnar dendritic, locally with needle type appearance specific to hardening martensitic structures with interdendritic separation of an intermetallic compound Fe - Al.

The microhardness of the laser cladding layer was HV0.1 = 3500 – 8000 MPa. Microhardness maximum corresponds to a working regime – Q = 86 mg/s, P = 1000 W, v = 7 mm/s, p = 2 mm, K = 79.36 J/mm^2, h = 0.38 mm, due to the presence of compound $FeAl_3$ in large amount and stability of the martensitic structure to the quick tempering process.

The regime considered optimum – Q = 53 mg/s, P = 1100 W, v = 7 mm/s, p = 1.5 mm, K = 87.30 J/mm^2, h = 0.74 mm, was used to study the behaviour to the abrasive wear of the laser cladding. Table 1 presents results from wear tests (mass wear, mass wear/length of path covered) in rotating disk with abrasive paper for both laser cladding samples and those classically hardened in volume and the support. The results are the average of three determinations.

It may be noted that the laser cladding alloy is more resistant to abrasive wear than samples classically hardened, and than the support. This is due to higher hardness obtained after laser cladding.

In Fig. 4 – 6, 3D images are presented made with an Image J software, of the sample areas obtained from the abrasive wear test.

Table 1. *Abrasive wear behaviour of the support, the deposit aluminum bronze powder, and the classically hardened aluminum bronze*

Material	Initial mass [g]	Final mass [g]	Mass wear [g]	Length run [m]	Wear/length run U/L [g/m]
1C45	2.9150	2.7270	0.188	82	0.00229
Laser cladding aluminum bronze	3.1638	3.0818	0.082	82	0.001
Aluminum bronze classical quenching	2.6625	2.5379	0.1246	82	0.00152

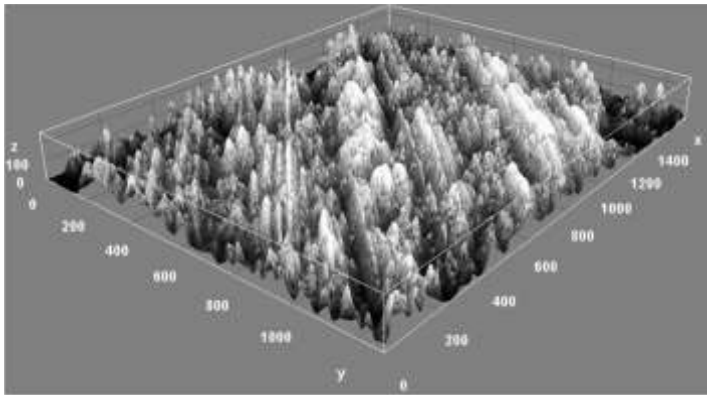

Fig. 4. *3D image of the 1C45 surface subjected to abrasive wear*

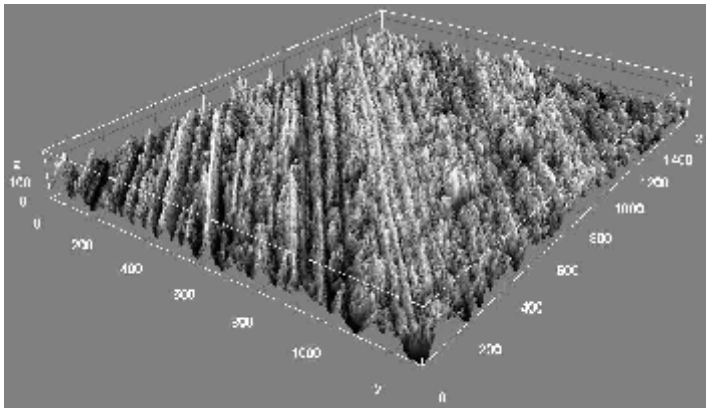

Fig. 5. *3D image of the laser cladding surface subjected to abrasive wear*

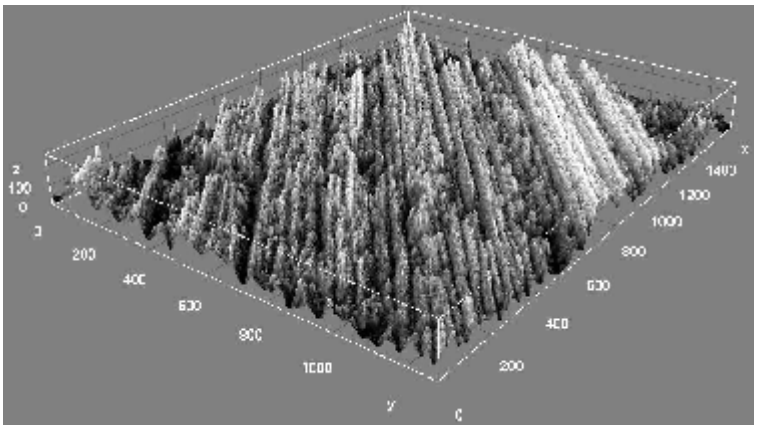

Fig. 6. *3D image of the classically hardened aluminium bronze surface subjected to abrasive wear*

4. Conclusions

When using multi layers coating by continuous wave laser beam, thick layers of copper alloy from the Cu-Al-Fe system may be achieved featuring higher wear resistance, and good density and adherence to the under layer through a thin dilution layer.

Laser coating by powder injected into a melt bath is a complex process of mass and heat transfer, which is efficient when associated with a powder injection system in continuous steady flow. With the coating process by laser beam of given power and dimensions, hardness and thickness of the deposited layer depend on the additional material flow, surface sweeping speed, initial sample temperature, number of superimposed layers and the extent of laser strips superimposition.

The optimum deposition regime was nickel alloy middle layer, regime – Q = 53 mg/s, P = 1100 W, v = 7 mm/s, p = 1.5 mm, K = 87.30 J/mm^2, which ensured a 0.74 mm thick layer with a microhardness HV0.1 = 3895 MPa. The microstructure of the deposited layer is fine, columnar dendritic, with interdendritic separation of an intermetallic compound Fe - Al.

Abrasive wear behaviour of laser cladding layers of aluminum bronze showed a higher resistance compared to steel 1C45, and aluminum bronze classically quenched.

References

[1]. Ehsan Toyserkani, Amir Khajepour, Stephen Corbin - *Laser cladding*, CRC Press LLC, 2005.
[2]. Jan Lodewijk de Mol van Otterloo - *Surface engineering with lasers*, Thesis, Shell Research and Technology Centre, Amsterdam, 1996.
[3]. Simona Boiciuc - *Research regarding laser cladding with injected powder*, Ph. D. Thesis, University of Galati.
[4]. H. Schumann - *Metallographie*, 1974, p. 514-516.
[5]. Dan Levcovici, Sanda Levcovici, Simona Boiciuc - *New technologies to increase the normal use of equipment, parts and aggregates*, project no. 10/839782/ 2007 – 2009, S.C. UZINSIDER ENGINEERING S.A. and ,,Dunarea de Jos'' University of Galati.
[6]. Shi Z, Bloyce A, Sun Y, Bell T. - *Effect of Processing Parameters on Structure and Properties of Surface Melted Aluminum Bronze*, Euromat 1995, vol. E+D, p. 365-371.
[7]. Sanda Levcovoci, Dan Levcovici, M. M. Paraschiv - *Laser Hardening of Aluminum Bronzes*, Materials and Manufacturing Processes, vol. 17, 2002, p. 13-22.

THE ANNALS OF "DUNAREA DE JOS" UNIVERSITY OF GALATI
FASCICLE IX. METALLURGY AND MATERIALS SCIENCE
N^0. 2 – 2014, ISSN 1453 – 083X

CORROSION BEHAVIOR OF ZINC ALLOY LAYERS

Tamara RADU, Anișoara CIOCAN,
Gina Genoveva ISTRATE
"Dunarea de Jos" University of Galati, Romania
e-mail: tradu@ugal.ro

ABSTRACT

The alloying of zinc with some additional elements in specific quantities could be reliably used in the hot-dip coating process. These elements conferr substantially improved performance to the end-product specially by improving corrosion resistance.

In this paper the influence of adding different percentages of aluminum and bismuth into the zinc bath was researched.

The technological conditions for obtaining zinc-bismuth-aluminium coatings with 0.27% - 0.52% bismuth and 0.11% Al are presented. The degree of micro-alloying and assimilation in the zinc bath was determined by spectrometric analysis of alloy samples, taken from the melt at different time intervals.

Corrosion resistance of the layers was assessed by two types of tests: corrosion behaviour in seawater for a period of five weeks and electrochemical tests in 3% NaCl solution. Both applied corrosion tests show an increase in corrosion resistance to bismuth content increasing and metallographic analysis of samples corroded shows a general corrosion process.

KEYWORDS: coating, bismuth, aluminium, corrosion

1. Introduction

The improvement of the corrosion resistance is the main objective in the improvement of the metallic coatings, being the defining characteristic of the protective coatings. Rate of corrosion can be modified by the addition of an alloying element. The sense of the modification will depend on the proportion of the alloying element in the base metal, its valence, the concentration and the nature of its characteristic lattice defects [1].

The corrosion behavior of the coat also depends on various factors such as: the coat chemical composition, thickness, adherence, uniformity, porosity [2-4].

To increase the corrosion resistance, adherence, limiting pollution and zinc-iron reaction, it is used more and more micro alloyed zinc melts with various elements: aluminum, nickel, titanium, tin, bismuth, etc. There is a great interest in carrying out research, which explores the influence of the alloying elements in zinc melt on coating layers characteristics and the characteristics of the melt.

In this paper the influence of adding different percentages of aluminum and bismuth into the zinc bath was researched.

In the interest of environment and health safety there is a trend in reducing or even eliminating altogether lead from zinc baths. In North America 25% of zinc coating plants have zinc baths without lead [5] and in Western Europe and Canada this percent is even higher. Lead has an important role in zinc baths [6, 7] that must be taken over by another micro-alloying element and the research in this area suggests the use of bismuth. The bismuth isn't toxic [8] like lead. The role of bismuth in zinc coating/galvanizing baths is still controversial. Most authors believe that bismuth increases zinc melt fluidity, reduces surface tension and increases zinc drainage onto the steel support [9, 10].

It may be added at a concentration of 0.1-1% below 0.5% most likely [11] bismuth influence on the protection layer is still questionable. It is believed to reduce film thickness as an effect of melt fluidity without changing the typical structure of a zinc deposition [11].

Aluminium is added to the galvanizing bath, in a continuous flow of the steel strips/plates, at a rate of 0.1-0.3% (optimal 0.14-0.17% [12]). Aluminium is added primarily to act as a brake to the reaction between zinc and steel support. Reducing the iron-zinc reactions it results a decrease in the brittle

intermetallic compound layer which has a negative impact on the layer adhesion and plasticity.

Because, compared to zinc, it has a higher affinity to iron, the aluminium present in the zinc bath will quickly form the $Fe_2Al_{5-X}Zn_X$ compound on the steel surface. This ternary compound arranged in a thin layer onto the steel support will limit the diffusion processes leading to the formation of Fe-Zn intermetallic compounds [13]. The aluminium content in the layer will be much higher than that in the zinc bath. At 0.14% Al in the bath, the entire zinc coating (including the ternary alloy layer) contains about 0.20% Al [13].

Also, the aluminium reduces the layer thickness, increases its brightness and increases the corrosion resistance. The presence of aluminium in the molten zinc leads to increased fluidity, oxidation speed reduction and decrease iron content (and consequently the amount of dross). Aluminium zinc alloying to improve zinc-coating layer can reach high percentages like galfan (5% Al) and galvalumme (55% Al).

2. Experimental research

For the preparation of the galvanizing bath pure zinc was used (99.996 wt.%).

Micro alloying with bismuth was made directly, using metallic pieces, finely crushed, followed by mechanical mixing. Laboratory experiments at the micro alloying zinc melts were performed in the temperature range typical galvanizing processes, working at 450-460^{o}C. Assimilation process of bismuth in the melt was stable, maximum efficiency is obtained. Aluminium alloying was made with Al-Zn alloy with 5% Al.

The presence of aluminium in the galvanizing bath, even at low contents (0.11% Al) leads to the formation of Al_2O_3 thin films on zinc bath surface thus preventing the formation of ash that can adhere to the coating surface causing defects. Also in the presence of aluminium coatings of very fine dendrites and metallic brilliancy [14] up to lustre are obtained (Figure 1).

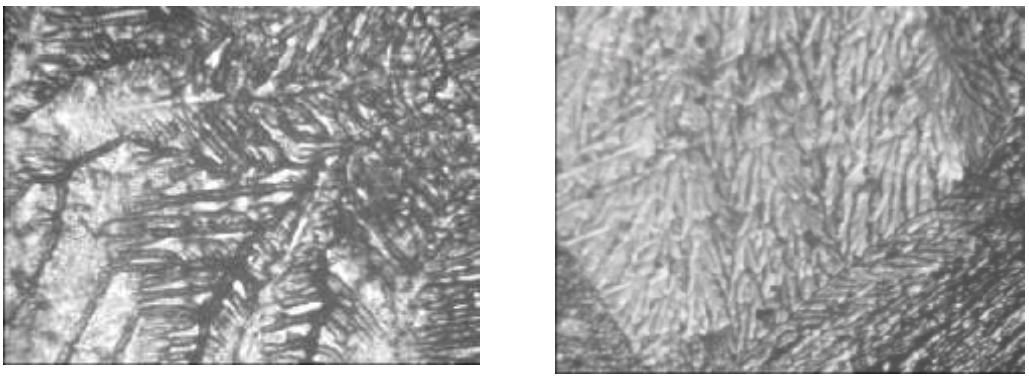

Zn-Bi Zn –Bi-Al

Fig. 1. *Morphology of the surfaces (bath temperature 450 ºC, immersion 7 s) x100*

The determination of the chemical composition of the obtained alloy was done using an X-ray spectrometer on solidified samples (taken from the melt after homogenization and at different times).

The chemical composition of the obtained alloys is presented in Table 1.

The composition of the steel samples support is presented in Table 2.

Table 1. *The chemical composition of the Zn-Bi-Al alloys*

Alloy	Bi wt.[%]	Al wt.%	Zn wt [%]	Other items wt. [%]
Zn-Bi-Al 1	0.27	0.11	99.35	Bal.
Zn-Bi-Al 2	0.36	0.11	98.75	Bal.
Zn-Bi-Al 3	0.52	0.11	99.02	Bal.

Table 2*. The chemical composition of the steel straps, wt. [%]*

C	Si	Mn	P	S	Al	As	Ti	V	Cu	Ni	Cr	Mo
0.025	0.015	0.210	0.013	0.010	0.046	0.004	0.002	0.001	0.005	0.008	0.025	0.001

The practical cooling conditions with a cooling speed much higher than that of equilibrium conditions [15] together with the low content of bismuth in the studied alloys lead to a biphasic structure formed from polygonal grains of zinc and fine crystals of bismuth uniformly spread in the zinc matrix (Fig. 2a). At higher bismuth content the proportion of the crystals dispersed in the zinc mass gets higher, and also their dimensions are larger, as it can be seen in Fig. 2b.

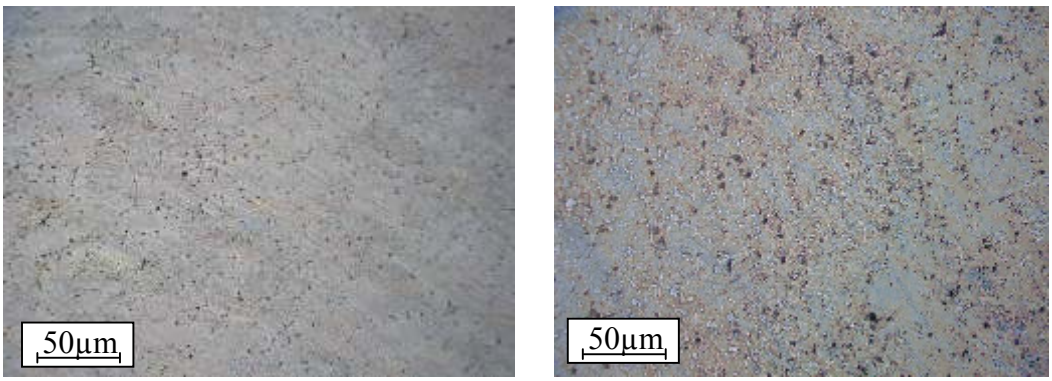

a) b)

Fig. 2. *Microstructure of zinc micro-alloyed with bismuth a) 0.27% Bi; b) 0.52% Bi* [11]

Micro-alloying the zinc with bismuth doesn't change significantly the aspect of the microstructure of the coating layer compared to coating with pure zinc (Fig. 3 a and b).

Bismuth yet acts on the layer made of iron-zinc alloys in the sense of thinning it down by the formation of a mechanical barrier between the intermetallic compounds phase and the liquid zinc phase. For higher bismuth content a small decrease in iron-zinc reactions is observed, the layer of intermetallic compounds from the steel-coating interface is thinner compared to its thickness when it is coated with pure zinc (Fig. 3b).

Having a higher affinity for iron than for zinc, aluminum will form at the surface of the steel support a thin microscopic film, out of Fe_2Al_5 compounds.

This layer, dense and compact, exerts a strong braked effect on the growth of the iron-zinc intermetallic compounds and microstructure of the coating layer shows a fine and uniform layer of intermetallic compounds at the interface steel/coating (Fig. 3c).

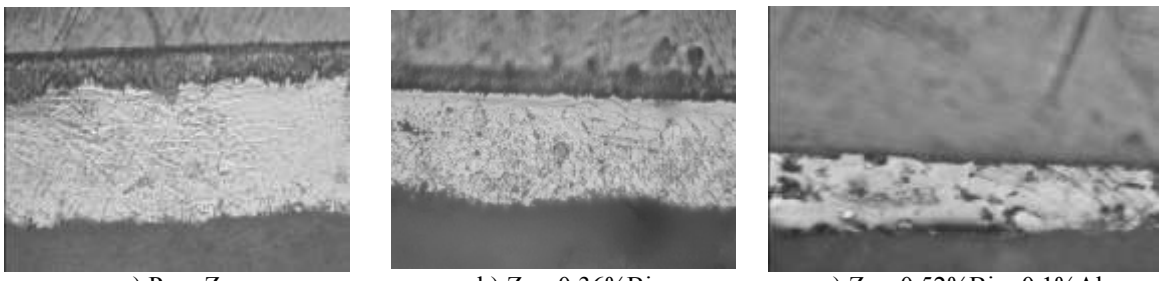

a) Pure Zn b) Zn - 0.36%Bi c) Zn - 0.52%Bi – 0.1%Al

Fig. 3. *Microstructure of the layers, (bath temperature 450 ºC, immersion 9s) x100*

Regarding the thickness of the layer (as shown in Fig. 3) bismuth and especially aluminum decrease the coating thickness. This effect is given by the increase in fluidity of the melt when bismuth and aluminum are added.

Corrosion resistance of the layers was assessed by two tests, gravimetric indices for corrosion behaviour in seawater for a period of five weeks and electrochemical tests in 3.5 wt% NaCl solution.

To determine the corrosion rate in sea water samples were sampled from every type of coating applied on the steel strip. These samples were immersed individually in recipients containing solution that imitates sea water: NaCl – 27 g/L; $MgCl_2$ – 6 g/L; $CaCl_2$ – 1 g/L; KCl- 1g/L; pH = 6.5-7.2, at room temperature.

The following steps have been covered: surface degreasing, weighing, immersing into sea-water containers, with a similar surface exposure to the corrosive agent. After each week the samples were washed, dried and weighed to determine the mass variation.

For the calculation of corrosion rate the following relation was used:

$$V_{corr} = \frac{\Delta m}{S \cdot t}[g \cdot m^{-2} \cdot h^{-1}] \quad (1)$$

where:

Δm – the weight loss by corrosion, [g];

S – the surface area of the corroded surface, [m^2];

t – the corrosion time, [h].

Results are presented in Figure 4. After seven days of exposure to corrosive environment the loss in weight of the samples was comparable.

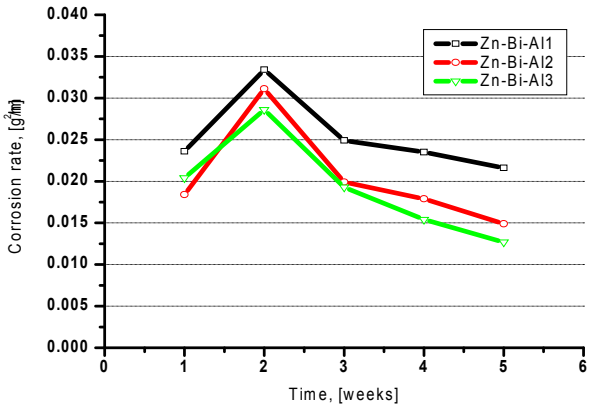

Fig. 4. *The variation of the corrosion rate as a function of the exposure time to the corrosive environment*

After 14 days, the corrosion speed is modified according to the accurrence of the corrosion products and to their intrinsic characteristics.

Thus the Zn-Bi-Al 1 has, in this case, the highest corrosion rate (0.0334 g/m^2·h) and the best behavior is observed at the sample coated with zinc micro-alloyed with 0.36% Bi – 0.11% Al (0.0286 g/m^2·h). In the third week the corrosion rate significantly decreases for all samples and decreases continuously for the next two weeks. Generally, the corrosion resistance increased with bismuth content.

The microscopic analysis of the surface shows the evolution of the corrosion process in time until the generalized corrosion of the surface at the end of the testing period as it can be seen in Fig. 5.

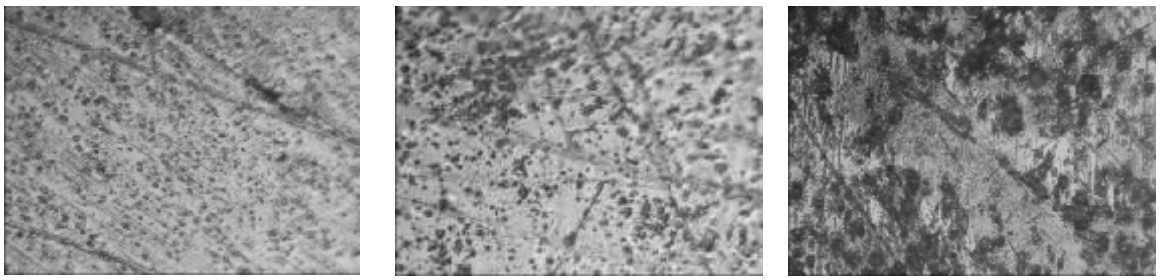

Week one Week two Week five

Fig. 5. *The modification of the surface during the corrosion process for sample Zn-Bi-Al 1, x100*

For the electrochemical tests, the corrosive environment used was a NaCl solution 30 g/L. A three-electrode cell, consisting of working electrode (Zn-Bi-Al coating samples) with an exposed area of 2 cm^2, an Ag/AgCl electrode as reference electrode and a platinum plate as a counter electrode, were used. Potentiodynamic polarization curves were recorded in the potential range from -1000 mV to -100 mV, at the scan rate of 2 mV/s. All measurements were performed at room temperature.

Before experiments samples were cleaned with water and acetone. Fig. 6 shows the Tafel curves. These curves were processed and the results shown in Tab. 4.

Table 4. *Electrochemical corrosion result by Tafel Method*

Coating	i_{cor}[μA/cm^2]	Rp[Ω cm^2]	v_{cor} [mm/y]
Zn-Bi-Al 1	19.6300	673.46	0.208
Zn-Bi-Al 2	15.0741	918.68	0.181
Zn-Bi-Al 3	13.9972	889.23	0.166

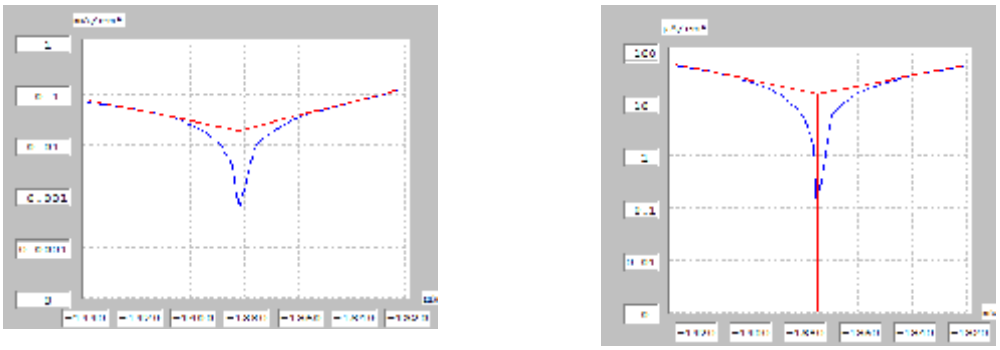

Fig. 6*. a) Tafel curve for Zn-Bi-0.36%Bi coating b) Tafel curve for Zn-Bi-0.11%Al coating*

Electrochemical test shows the same trend of decreasing corrosion rate when the bismuth content increases.

Increased corrosion resistance can be caused by the cumulative effects of bismuth and aluminum to the zinc melt characteristics and their products corrosion.

3. Conclusions

- Bismuth has a melting temperature lower than zinc and it is easily assimilated in galvanizing bath;
- Microstructure of alloy samples, taken from the galvanizing bath, reveals a homogeneous structure with polygonal grains of zinc and fine crystals of bismuth, uniformly spread in the zinc matrix;
- Layers microstructure shows a decrease in thickness in the presence of bismuth and aluminum especially;
- In the presence of bismuth and aluminum reactions between iron and zinc are strongly braked;
- The corrosion rate in seawater for a period of five weeks shows a similar variation for the three types of layers studied;
- The most significant corrosion rate is achieved for all the samples in the second week and then decreases continuously in the next weeks;
- Metallographic analysis of samples corroded shows a general corrosion process;
- Both applied corrosion tests show an increase in corrosion resistance to bismuth content, increasing from 0.2% to 0.52%.

References

[1]. F. C. Porter - *Zinc handbook: properties, processing, and use in design*, Marcel Dekker, New York, 1991.

[2]. Khadoudj Guessoum, Delphine Veys-Renaux, Emmanuel Rocca, Kamel Belhamel - *Corrosion behaviour of zinc–cerium alloys: Role of intermetallic phases*, Corrosion Science, vol. 53, Issue 5, May 2011, p. 1639-1645.

[3]. Lijing Yang, Yangming Zhang, Xuduo Zeng, Zhenlun Song - *Corrosion behaviour of superplastic Zn–Al alloys in simulated acid rain*, Corrosion Science, vol. 59, June 2012, p. 229-237.

[4]. Shengqiang Ma, Jiandong Xing, Dawei Yi, Hanguang Fu, Guofeng Liu, Shengchao Ma - *Microstructure and corrosion behavior of cast Fe–B alloys dipped into liquid zinc bath*, Materials Characterization, vol. 61, Issue 9, September 2010, p. 866-872.

[5]. John Zervoudis, Graeme Anderson - *A Review of Bath Alloy Additives and their Impact on the Quality of the Galvanized Coating*, Teck Cominco Metals Ltd. 120 est, Suite 1500 Toronto, Ontario, Canada, p. 4.

[6]. *** **-** *Galvanising Reactive Steels*, a guide for galvanizers and specifies, International Lead Zinc Research Organisation, Research Triangle Park, NC.

[7]. Xinhua Wang, Jintang Lu, Chunshan Che, Gang Kong - *The behavior of lead during the solidification of Zn–0.1Al–0.1Pb coating on batch hot-dipped steel*, Applied Surface Science, vol. 254, Issue 8, 15 February 2008, p. 2466-2471.

[8]. Gagne M. - *Zinc Bismuth Alloys for After Fabrication Hot Dip Galvanizing*, American Galvanizers Association Tech Forum 1997, Houston, TX.

[9]. J. Pedersen - *Latest developments in nickel-zinc galvanizing*, Cominco Ltd Ontario, Canada, on line.

[10]. Pistofidis N., Vourlias G., Pavlidou E., Stergioudis G. - *Effect of Ti, Ni and Bi addition to the corrosion resistance of Zn hot-dip galvanized coatings,* Journal of optoelectronics and advanced materials 2007, vol. 9, no. 6, p. 1653.

[11]. Tamara Radu, Florentina Potecasu, Maria Vlad - *Research on obtaining and characterization of zinc micro-alloyed with bismuth coatings*, Metalurgia International, nr. 1/2011, ISSN 1582-2214, p. 44-48.

[12]. *** **-** *The Role of Aluminium in Continuous Hot-Dip Galvanizing*, GalvInfoNote 1.9, Rev 1.0, mar. 2009.

[13]. *** **-** *Zinc Bath Management on Continuous Hot-Dip Galvanizing,* GalvInfoNote 2.4.1 Rev 1.0 Aug-09.

[14]. S. Sepper, P. Peetsalu, M. Saarna - *Methods for evaluating the appearance of hot dip galvanized coatings*, Agronomy Research Bio system Engineering Special Issue 1, 2011, p. 229-236.

[15]. *** **-** ASM Metals Hand Book Alloy Phase Diagrams.

THE ANNALS OF "DUNAREA DE JOS" UNIVERSITY OF GALATI
FASCICLE IX. METALLURGY AND MATERIALS SCIENCE
N^0. 2 – 2014, ISSN 1453 – 083X

GEOPOLYMERS OBTAINED WITH RED MUD FROM ALUMINA MANUFACTURING

Ilenuța SEVERIN (SPĂTARU), Maria VLAD
"Dunarea de Jos" University of Galati, Romania
e-mail: severin_ilenuta@yahoo.com

ABSTRACT

Getting reusable aluminosilicate materials, based on the geopolymerization reaction mechanism of some physical and mechanical material particular, has been imposed in the recent years in building materials.

This paper presents the physico-chemical and structural characteristics of the red mud from alumina (Al_2O_3) manufacturing through the Bayer process, material that can be investigated in order to obtain geopolymeric materials. Geopolymers made from red mud are eco- friendly on the one hand because their synthesis reuses waste from industries as raw materials, and on the other hand, because the conditions through which they can be obtained are more economics and cheap.

KEYWORDS: geopolymers, residue, red mud, construction materials

1. Introduction

Considering the problem of pollution in the entire planet, the demand for cement used in construction of the momentum buildings, getting Portland cement and other types of building materials using concrete, are a source of pollution with a strong impact on the environment. Both in terms of technology and production of the raw material, large-scale production of cement, namely a building material by conventional technologies, poses a threat. Therefore, to minimize the negative effect was taken into account obtaining other materials which fulfill the same role at the same time as environmentally friendly as the technology of production and layout while.

After analyzing some specialty papers, it was concluded that the creation of waste by the geopolimerization process, a building material with a minimum of cost of raw material and production technology is an intelligent and effective reuses of these types of waste. This article deals with the process of getting geopolymer cement with solid waste as raw material (clay, ash) or semi-solids such as sludge, in this case, the red sludge resulting from the Bayer process, the basic requirement for achieving this material being a high content of crystalline aluminosilicate phase.

In the cement industry, in an attempt to protect the environment was already partially replaced the amount of solid aggregate, non-renewable raw materials with ash from power plants that run on fossil fuels [1-3], or slag from the manufacture of iron [4-6] with very good results, so that the properties of the obtained geopolymers may be comparable to that of Portland cement. Being highly successful in this regard, researchers attempts were not limited to these conditions but we tried to replace the unit with other solid waste. In this sense, changing the source of aluminosilicate was achieved with red mud, but because there are no known conditions that ensure its maximum properties, thorough research are needed.

1.1. The concept of geopolimer

The term of geopolimer assigned as a building material was first introduced in the academic language by the French researcher J. Davidovits in 1979, [7] and was defined as a "polymeric mineral made by geochemistry or geosyntesis "aluminosilicate materials dissolved in the basic medium. In this context, the term refers to a inorganic three-dimensional geopolymeric structure with a high content of aluminosilicates which is structurally similar with natural aluminosilicates, respectively zeolites. The general formula for a geopolymer is: [8] $_{\cdot}\mathbf{Mn[-(SiO_2)_z\text{-}AlO_2]_n}\cdot\mathbf{wH_2O}$ in which **n** is the degree of polycondensation or polymerization; **z** is the ratio Si/Al and may be 1, 2 or 3; **M** is a cation such as Na^+ or K^+, and **w** is the number of water molecules in the geopolymeric structure. The inorganic polymeric material formed by SiO_4 and AlO_4 tetrahedral units is arranged in a three-dimensional structure and the link between these units is balanced by alkali ions.

Geopolimerization reaction mechanism involves the following steps [9]: the dissolution of aluminosilicates in alkaline solution refocuses ions in the network and generates the formation of geopolymer. Figure 1 shows the block diagram for obtaining a geopolymer.

Fig. 1. *The block diagram for obtaining a geopolymer*

1.2. Geopolymers made from recyclable materials

In the recent years, teams of researchers have highlighted the importance of reuse of industrial by-products that are generated in large amounts as in the case of red mud.

Researcher Liu X.and his team [10] analyzed the red mud samples with a length of three years, resulting from the calcination of bauxite ores. The samples were previously subjected to drying in an oven at 100 °C they comminuted to obtain a powder which was subjected to calcination in an electric furnace at a temperature between 400 °C and 900 °C. The powder was obtained by ball milling with an average diameter of about 23 μm. They mixed a quantity of 50% calcined red mud with 45% clinker and 5% gypsum and obtained a mortar which has undergone testing according to current standards, and the results are satisfactory and comparable to those of Portland cement.

Geopolymers obtained in laboratory by researcher A. Van Riessen *et al.* [11] have been made in order to reuse the solution resulting from the Bayer process alumina production. They compared the geopolymeric cement paste that was obtained with pure NaOH solution and the solution of synthetic red mud processed (Bayer solution) in order to determine the effectiveness of the Bayer alumina source solution and at the same time, the quality of the cement alkaline source, respectively of a resulting slurry. There have been geopolymeric pulp samples in which the source of alkaline substituted, NaOH at various concentrations, with the following chemical composition: Al_2O_3 (15%), Na_2O (24%) and H_2O (61%). After analyzing the different methods, they concluded that the Bayer liquore did not influence the solution properties of cement paste made with Bayer solution compared to pure NaOH solution and the solution made synthetically.

To obtain a binder for geopolimeric materilas of construction debris mixed with ash class F, a team of researchers led by Saeed Ahmari [12] analyzed the effect of mineralogy to specify the amount of waste, the concentration of the alkaline solution and the amount of calcium effect on the binder composition. Since in the structure of geopolymer, besides the quantity of calcium hydrate and silica hydrate, there are calcium and aluminum, it has been shown that increasing the amount of calcium compound based on the base material may improve the mechanical properties of geopolymer. In his work, L. Reig *et al.* [13] have used waste (red brick) from the demolition of buildings, an impressive amount that can be reused to make a cement paste and mortar. In this case, alkali activators used were sodium hydroxide and sodium silicate. It has been found that a mixture of the 45/6.0/1.6 mole ratio is one that has shown the best mechanical properties. The samples obtained were dried at a working temperature of 65 °C for 7 days, and were used to compare the geopolimeryzation waste material resulting from the initial to the difference between the initial properties and the subsequently obtained properties. Thus it can be stated that physical characterizations of geopolymers obtained from different sources of alkali activated aluminosilicate in different quantities and chemical and mineralogical characterization provides valuable information on how to obtain the best mechanical properties not only thereof.

Thus, it has been found in many studies that in order to obtain a diffusion of the aluminate and

silicate waste from the original source, it is necessary that the source has a high degree of fineness, the reactivity of the mixture increases in proportion to changes in particle size, [14] activation of the concentration of the solution of the formulation [15, 16] and the amount of water in the system. Also, knowing the exact chemical composition is advantageous for adjusting the recipe to get those elements and chemical species without which you can not achieve cementitious material properties required for use in construction. Mineralogical composition provides information about existing minerals and their influence on the structure of geopolymers prescription.

2. Red mud

The use of red mud filler material as a material for obtaining various geopolymeric materials is comparable to the quality of the materials obtained by extraction from ore an easy process, both from the point of view of therapy and financial processing. Because aluminum demand is very high in Romania and elsewhere in the world by producing one ton of aluminum resulting approximately two tons of wet waste, ie red mud, which amount exceeds its reuse. [17]. Therefore, it is imperative that the waste to be used in other directions, thus solving some of the issues raised after storage in the open landfill (transport of particulate matter infiltration of substances into groundwater, etc.).

Red mud is a semi-solid waste produced during the extraction of alumina from bauxite ore by the Bayer process. They use several terms that define the same structure ie bauxite waste; tailings resulting from the Bayer process; or tailings resulting from the processing of bauxite. The investigations concluded that the waste due to the high content of aluminosilicate is a source of raw material that can replace some, or all solid units that go into a building material.

Generation of red mud in the production of alumina takes place in the first stages by means of acid or alkaline leaching of the sinter ore or bauxite, or other materials with a high content of alumina, which are generally in the form of aluminosilicates, such as nefelinele, oil shale, subjected to physico-chemical process for extracting aluminum hydroxide or other aluminum compounds which ultimately will result in ignition alumina [18]. In Figure 2 is shown schematically how it is obtained that the alumina and red mud from bauxite by the Bayer process. Tailings recovered from the filtering process called red mud are collected, washed and directed to storage area which can be: a lagoon, a large area, disused mines or landfills.

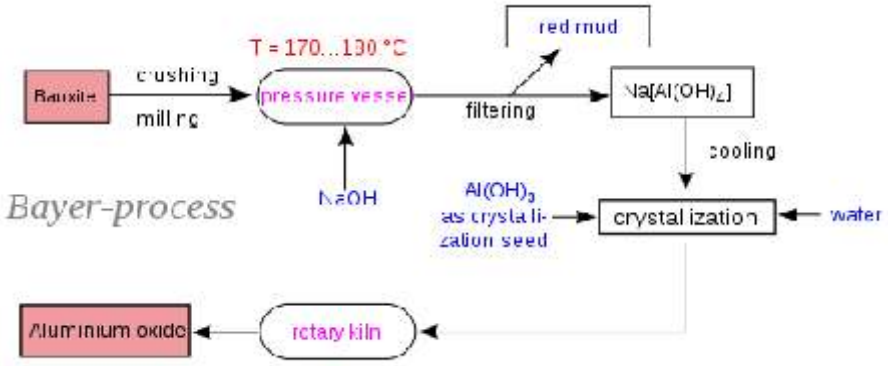

Fig. 2. *The Bayer process* [19]

Regardless of ore with a high aluminum content processing and extraction technology used alumina, red mud result raises environmental issues locally and globally. Re-use of the red mud is based on the following: the origin of the ore, the treatment, the water content, the amount of radioactive metal slurry composition, the alkalinity of the particle size, mineralogy. There are several technologies for obtaining of red mud geopolymers, each depending on both the amount of red mud is used and the future direction of the use thereof. In construction, the red mud is used in large quantities together with other wastes, in the form of binder [20-22], mortar, [23], reinforced concrete [24, 25] concrete [26, 27], amendment of pollutants in solid and liquid phases [28], building bricks [29], bricks [30] aggregate in building materials [31], or recipes for the manufacture of ceramics [32, 33], glazes [34], in the extraction of heavy metals [35, 36], as an adsorbent for the removal of H_2S from industrial emissions [37]. In Figure 3 are shown the potential applications of red mud.

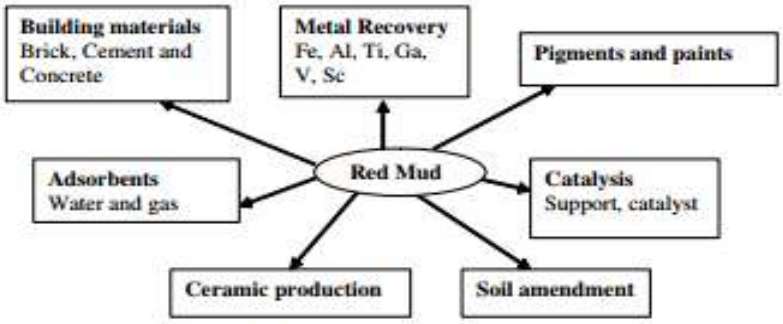

Fig. 3. *Potential applications of red mud* [38]

3. Physico-chemical and structural properties of red mud

3.1. Physico-chemical properties

Bauxite tailings semi-solid material has a brick-red color due to the high amount of iron oxide, iron sulfate, silicoaluminates, titanium dioxide, etc. The red mud particle size is characteristic of each type of ore bauxite and varies between limits below 100 mm and 200 micrometers. Red mud is a mixture of mineral and chemical composition which depends on the bauxite ore (diaspore, boehmite, gibbsitic) containing alumina, in which the solid phase is about 20% to 80% of the total quantity of sludge. Minerals with the highest weight are, in order, the following: Hematite (α-Fe_2O_3), Goethite (α-FeOOH), Magnetite (Fe_3O_4) as iron oxides with an average of 40.9%; followed by the Boehmite (AlOOH-γ), Gibbs, (γ-Al $(OH)_3$), Diaspora (γ-AlOOH), aluminum oxides as an average of 16.3%. The silicon oxide content averages 9.6%, respectively: Sodalite ($Na_6[Al_6Si_6O_{24}]2NaOH$, $Na_2SO_4]$), Cancrinite ($Na_6[Al_6Si_6O_{24}]2[CaCO_3]$-$O[H_2O]$), Quartz ($SiO_2$) and other, Illite, Muscovite. Titanium oxides are embedded in smaller quantities, 8.8% minerals form: Rutile (TiO_2) Anatase (TiO_2), Perovskite ($CaTi^{iv}O_3$), Ilmenite, ($Ti^{IV}Fe^{ii}O_3$). Other minerals are small amounts of oxides from sodium and calcium. Also found in traces the next: K, Cr, V, Ni, Ba, Cu, Mn, Pb, and Zn [39].

3.2. Materials and methods

Red mud used in this study was made from bauxite manufacturing by the Bayer process, ALUM Tulcea, namely dried red mud dumped in the related plant. Firstly raw red mud dried was sieved using a set of sieves grain of 125 µm. For the experiment were weighted 3.5 g of red mud grain of 125 µm with an analytical balance. A sample was subjected to calcination in a furnace-type Lenton Thermal Design at a calcination temperature of 600 °C, at a heating rate of 10 °C/minute, a hold time of 45 minutes. Following the calcination process, resulted 2.1 g of red mud, which is a weight loss by eliminating natural water of about 60%.

3.3. Analytical methods

Uncalcined an calcined samples, were subjected to thermogravimetric analysis (TGA) and (DTG), differential scanning calorimetry analysis (DSC), and analysis to determine the structure and chemical composition by electron microscopy (SEM).

It is very important to know the thermal behavior of red mud because according to this process can specify a future use of its as a construction binder or other geopolimeric type material.

4. Experimental data and literature

The reaction temperature is very important for obtain a geopolimer from any source of aluminosilicates materials, the red mud has been characterized from the point of view of the thermal effects, physical and chemical processes taking place in state of uncalcined sample and calcined sample at 600 °C. Differential scanning calorimetry analyzes were performed in the laboratory of UDJG nanostructures, the analyzer Q20 found in the laboratory, which is provided with a platinum crucible, the temperature is in the range of 20 °C-400 °C, with a heating rate of 10 °/min in an inert atmosphere (nitrogen). The sample was weighed and then subjected to analysis.The resulting curves are shown in Figure 4a and in Figure 4b.

The DSC technique, differential scanning calorimetry curves that determined the changes of heat and mass due to physical and chemical degradation of red mud compounds entering the structures analyzed. With this technique were evaluated faster interactions between components based on changes of endothermic and exothermic peaks of the device. The literature mentions the main

minerals contained in red mud [39], and temperatures at which phase transformations occur [40]. The analyses made the following considerations: in the temperature range of 40 °C to a maximum temperature of 68 °C it appears to be little loss of water due to the hygroscopic nature of the calcined and uncalcined sample. Also, in the temperature range of 230 °C there is another peak which is explained by loss of chemically bound water of the peak maximum at around 279 °C or transformation of the silica into tridymite lower Cristobalite (metastable phase) at around 275 °C which further will change under the temperature action in higher Cristobalite [40]. Other exothermic changes after analyzing samples are the reduced of magnetite to iron and with CO and forming CO_2 with a maximum peak at 321 °C [41]. For the corresponding temperature peak of 380 °C, the appearance of the DSC curve is assigned to the formation of sodium carbonate, Na_2CO_3, after the interaction between NaOH and CO_2.

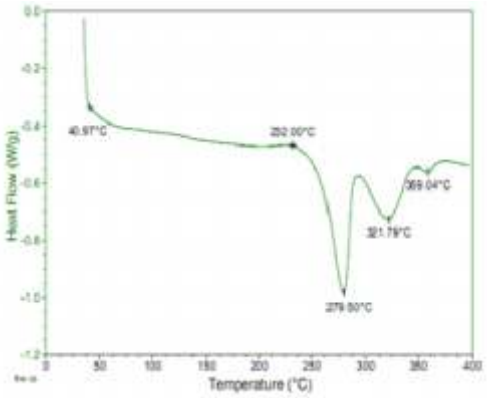

Fig. 4a. *DSC curve of a non-calcined sample*

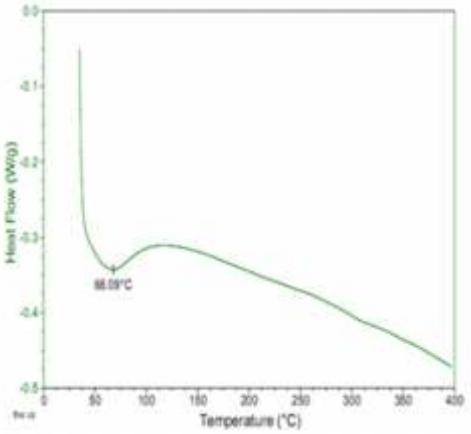

Fig.4b. *DSC curve of a calcined sample*

Thermal gravimetric analysis curves were made with thermogravimetric analyzer, Q5000 IR with air purified 5.0, under an inert atmosphere of nitrogen, with 12.5 mg of the uncalcined sample weight and 13.33 mg of calcined sample.

The thermogravimetric curves are shown in Fig. 5 a) and Fig. 5 b), and they highlight the changes that occur as a result of phase transformation or formation or dissociation of chemical combinations in the mass of the sample.

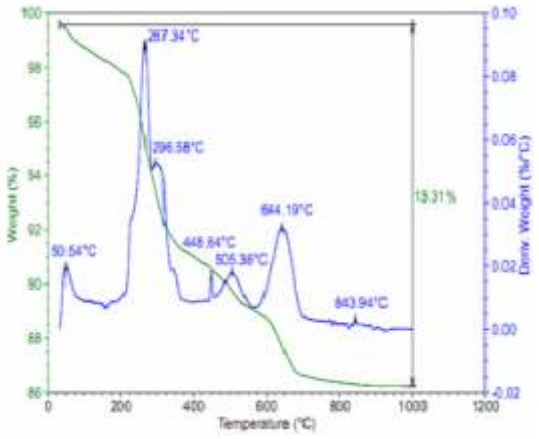

Fig. 5a. *TGA, DTG curves of a non-calcined sample*

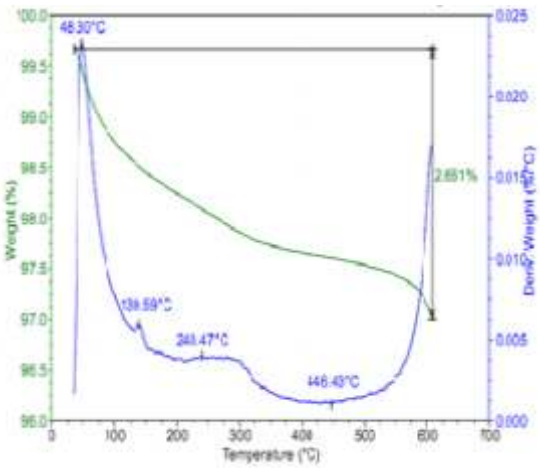

Fig. 5b. *TG , DTG curves of a calcined sample*

As the temperature in sample increases linearly with time, mass loss occurring due to physical or chemical processes in red mud as a result of temperature increase and the decrease of mass is initially 2.66% for the calcined sample and 10.96% for the uncalcined sample. As observed in the DSC curve and the DTG, there is a little peak around the temperature of 50 °C which demonstrates the removal of water of hydration and water of crystallisation at temperatures above 170 °C with a maximum peak of 267 °C in DTG curve. And for the thermogravimetric curves occurring specific peaks of the phase transformation of silica from tridymite into inferior Cristobalite, but in this case, phase transformation is

evidenced by the temperature about of 296 °C [40] and also the conversion of the magnetite into Fe with the releasing of CO_2 [41] in the temperature about of 300 °C. It is noted that the peaks which appear at temperatures superior to 400 °C, temperatures to which other already started process occurs or are continued if necessary (such as cristobalite which has continued its transformation up to temperatures approaching of 1000 °C) [40]. Thus, at temperatures above 450 °C there is a bit that can be attributed to the formation of sodium carbonate (Na_2CO_3). At temperatures above 550 °C begins the calcination of aluminum hydroxide into γAl_2O_3. Also in the temperature range of 600 °C can take place the decomposition reaction of calcium carbonate ($CaCO_3$) from the red mud.

Thus, is resulted from the analysis of diagrams, that many of exothermic reactions presented on scanning calorimetry curves and on the thermogravimetric analysis curves are due, in general, to the chemical and physical losses of bound water; phase transformations or other chemical processes between the red mud components, or to the processes of decomposition of the components.

4.1. SEM analysis

Scanning microscopic structure analyses, SEM were made in the laboratory UDJG, the type QUANTA analyzer 200, which is provided with an EDX analyzer type. These tests were carried out on samples annealed at 600 °C and non-calcined samples in order to emphasize the structural changes that occur as a result of the heat treatment applied.

In Figures 6a and b are shown SEM images of the non-calcined samples with particle size of 12.5 μm in the sizes of 500x, 5000x and Fig. 7a or b are shown SEM images of the sample annealed and their respective sizes 500x and 5000x.

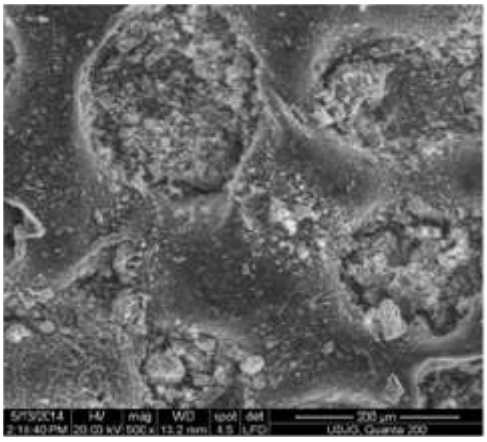

Fig. 6a. *SEM image of the non-calcined sample 500x*

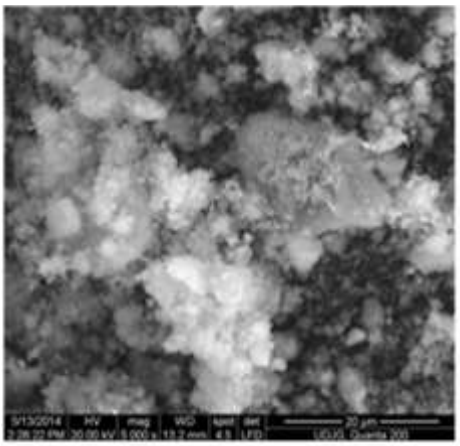

Fig. 6b. *SEM image of non-calcined sample 5000x*

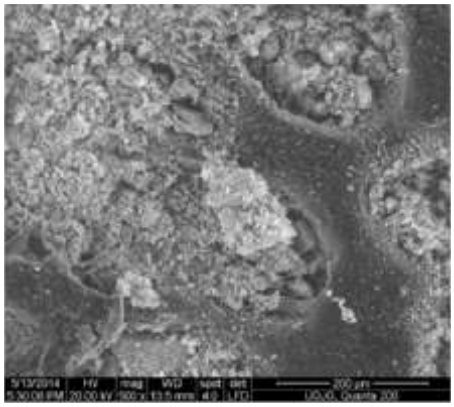

Fig. 7a. *SEM image of the calcined sample 500x*

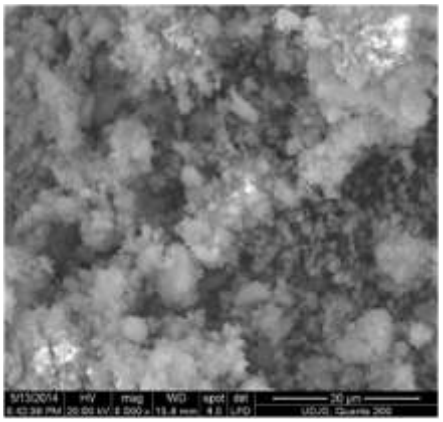

Fig.7 b. *SEM image of calcined sample 5000x*

Figures 8a and 8b shown the non-calcined sample spectra and calcined sample, respectively, and Fig. 9a and 9b maps the layout elements of an non-calcined and calcined samples.

In Table 1 and Table 2 are shown the elemental composition of uncalcined and respectively calcined sample.

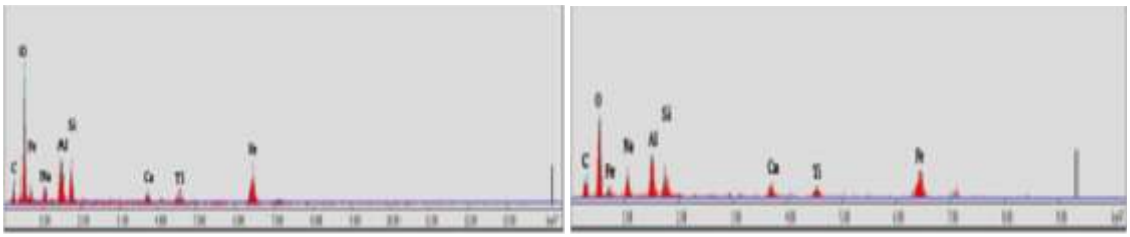

Fig. 8. *a) Non-calcined sample spectrum; b) Calcined sample spectrum*

Tabel 1. *The elemental composition of non-calcined sample*

Element	Wt%	At%
C	21.38	33.30
O	40.47	47.33
Na	3.97	3.23
Al	6.66	4.62
Si	5.56	3.70
Ca	2.43	1.13
Ti	2.58	1.01
Fe	16.96	5.68

Tabel 2. *The elemental composition of a calcined sample*

Element	Wt%	At%
C	21.10	34.44
O	33.03	40.49
Na	6.78	5.78
Al	8.62	6.26
Si	4.76	3.32
Ca	3.28	1.61
Ti	3.78	1.55
Fe	18.65	6.55

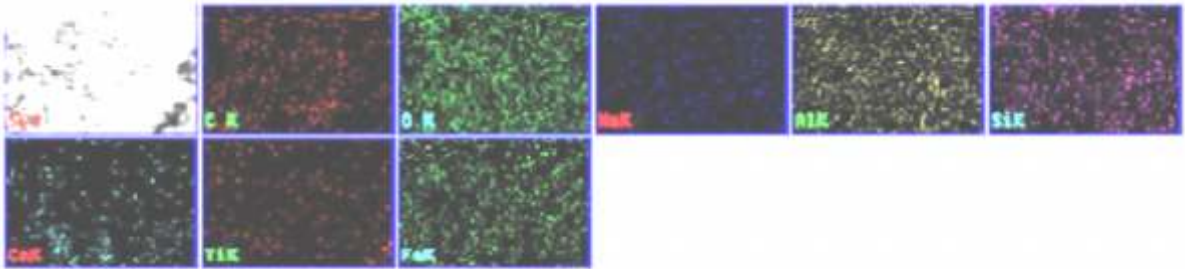

Fig. 9a. *The distribution map of the main chemical elements in the non-calcined sample, 5000 X*

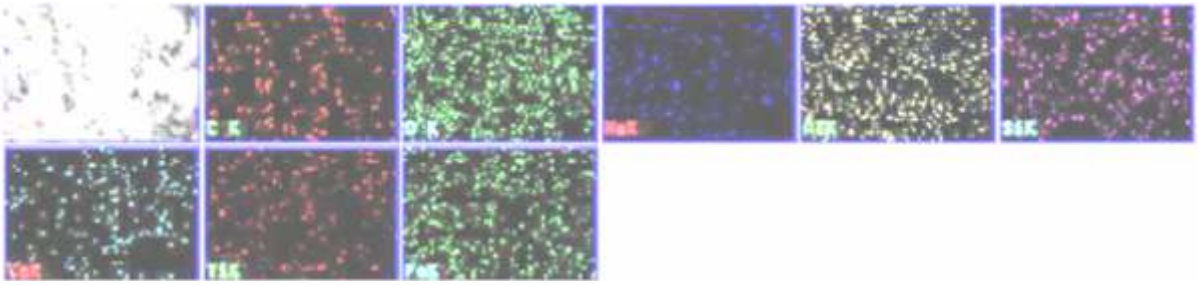

Fig. 9b. *The distribution map of the main chemical elements in the calcined sample, 5000 X*

From the analysis of scanned images by scanning electron microscopy it was observed that the metallographic structure of uncalcined sample reveals fewer crystallized phases compared to the sample that was subject to the calcination treatment, which shows that after calcination took place and transformations phase, passage of silica from tridymite into inferior Cristobalite, or of the amorphous phases into crystalline phases.

5. Conclusions

Geopolymers are inorganic polymers, alkali-activated aluminosilicates, from different materials characterized by a high content of oxides of aluminum, silicon, calcium, and their complexes, which are employed in various industrial fields. Red mud is one of these sources of aluminosilicate (among other materials) used to obtain geopolymers.

Due to the great demand for aluminum and the very high amount of red mud generated , the demands for building materials, the solution to reuse of this waste is the best way to solve both environmental issues and socio-economic issues related to obtaining cheap and durable buildings materials.

In order to know the properties of a material it is important to know the chemical composition, physical properties, namely the structure of the material. Therefore in this study were performed chemical analysis, thermal, and structural for the uncalcined samples and calcined samples. From thermal and structural analysis has emerged a picture of the behavior of the temperature variation of the red mud. Thus, by analyzing DSC, DTG and TGA was observed a mass loss due to removal of physically bound water or crystallization water and other chemical processes or specific material phase transformations.

The SEM analysis showed a difference in structure and surface morphology of the uncalcined sample compared to the calcined sample, difference is explained by the fact that when the heat treatment is applied, crystalline phases occurring are important in the reuse of the red sludge for the various materials used in construction.

Acknowledgements

The work was funded by the Sectoral Operational Programme Human Resources Development 2007-2013 of the Ministry of European funds by financial agreement POSDRU/159/1.5/S/132397.

References

[1]. C. A. Rees, J. L. Provis, G. C. Lukey, J. S. J. van Deventer - *ATR-FTIR analysis of fly ash geopolymer gel ageing*, Langmuir, 23 (15), 2007, p. 8170-8179.

[2]. I. García-Lodeiro, A. Palomo, A. Fernández-Jiménez - *Alkali–aggregate reaction in activated fly ash systems*, Cem. Concr. Res., 37 (2), 2007, p. 175-183.

[3]. J. M. Miranda, A. Fernández-Jiménez, J. A. González, A. Palomo - *Corrosion resistance in activated fly ash mortars*, Cem. Concr. Res., 35 (6), 2005, p. 1210-1217.

[4]. W. Mozgawa, J. Deja - *Spectroscopic studies of alkaline activated slag geopolymers*, Journal of Molecular Structure, 924–926, 2009, p.434-441.

[5]. M. Komljenovic´, Z. Bašcarevic´, N. Marjanovic´, V. Nikolic - *External sulfate attack on alkali-activated slag*, Construction and Building Materials, 49, 2013, p. 31-39.

[6]. A. Natali Murri, W. D. A. Rickard, M. C. Bignozzi, A. van Riessen - *High temperature behaviour of ambient cured alkali-activated materials based on ladle slag*, Cement and Concrete Research, 43, 2013, p. 51-61.

[7]. Davidovits J. - *Properties of geopolymer cements,* In: First international conference on alkaline cements and concretes, 1994.

[8]. Zhang G. P., He J. A., Gambrell R. P. - *Synthesis, characterization, and mechanical properties of red mud-based geopolymers*, Transp Res. Rec., 2167, 2010, p. 1-9.

[9]. Xiaoming Liu, Na Zhang, Henghu Sun, Jixiu Zhang, Longtu Li - *Structural investigation relating to the cementitious activity of bauxite residue - Red mud*, Cement and Concrete Research, 41, 2011, p. 847-853.

[10]. Arie van Riessen, Evan Jamieson, Catherine S. Kealley, Robert D. Hart, Ross P. Williams - *Bayer-geopolymers: An exploration of synergy between the alumina and geopolymer industries*, Cement & Concrete Composites, 41, 2013, p. 29-33.

[11]. Saeed Ahmari, Xin Ren, Vahab Toufigh, Lianyang Zhang - *Production of geopolymeric binder from blended waste concrete powder and fly ash*, Construction and Building Materials, 35, 2012, p. 718-729.

[12]. L. Reig, M. M. Tashima, M. V. Borrachero, J. Monzó, C. R. Cheeseman, J. Payá - *Properties and microstructure of alkali-activated red clay brick waste*, Construction and Building Materials, 43, 2013, p. 98-106.

[13]. Ubolluk Rattanasak, Prinya Chindaprasirt - *Influence of NaOH solution on the synthesis of fly ash geopolymer*, Minerals Engineering, 22, 2009, p. 1073-1078.

[14]. R. E. Lyon, P. N. Balaguru, A. Foden, U. Sorathia, J. Davidovits, M. Davidovics - *Fire-resistant aluminosilicate composites*, Fire Mater., 21 (2), 1997, p. 67-73.

[15]. Shaotao Cao, Haijun Ma, Yi Zhang, Xiaofan Chen, Yifei Zhang, Yi Zhang - *The phase transition in Bayer red mud from China in high caustic sodium aluminate solutions*, Hydrometallurgy, 140, 2013, p. 111-119.

[16]. Vladimır Zivica - Effects of type and dosage of alkaline *activator and temperature on the properties of alkali-activated slag mixtures,* Construction and Building Materials, 21, 2007, p. 1463-1469.

[17]. Benny Joseph, George Mathew - *Influence of aggregate content on the behavior of fly ash based geopolymer concrete*, Scientia Iranica, 19, 2012, p. 1188-1194.

[18]. M. Gräfe, G. Power, C. Klauber - *Bauxite residue issues: III. Alkalinity and associated chemistry*, Hydrometallurgy, 108, 2011, p. 60-79.

[19]. * -** http://en.wikipedia.org/wiki/Bayer_process.

[20]. P. E. Tsakiridis, S. Agatzini-Leonardou, P. Oustadakis - *Red mud addition in the raw meal for the production of Portland cement clinker*, Journal of Hazardous Materials, 116, 2004, p. 103-110.

[21]. Maneesh Singh, S. N. Upadhayay, P. M. Prasad - *Preparation of iron rich cements using red mud*, Cement and Concrete Research, 27, 1997, p. 1037-1046.

[22]. Yiannis Pontikes, Ruben Snellings - *Handbook of Recycling*, 2014, p. 219-229.

[23]. L. Senff, R. C. E. Modolo, A. Santos Silva, V. M. Ferreira, D. Hotza, J. A. Labrinchae - *Influence of red mud addition on rheological behavior and hardened properties of mortars*, Construction and Building Materials, 65, 2014, p. 84-91.

[24]. D. V. Ribeiro, J. A. Labrincha, M. R. Morelli - *Effect of the addition of red mud on the corrosion parameters of reinforced concrete*, Cement and Concrete Research, 42, 2012, p. 124-133.
[25]. D. V. Ribeiro, J. A. Labrincha, M. R. Morelli - *Effect of the addition of red mud on the corrosion parameters of reinforced concrete*, Cement and Concrete Research, 42, 2012, p. 124-133.
[26]. W. Hajjajia, S. Andrejkovičová, C. Zanelli, M. Alshaaer, M. Dondi, J. A. Labrincha, F. Rocha - *Composition and technological properties of geopolymers based on metakaolin and red mud*, Materials Design, 52, 2013, p. 648-654.
[27]. Abhishek H. N., M. U. Aswath - *Strength studies of red mud based geopolymers concrete*, Int. Juo.of Em. Trends in Eng. and Dev., 6, 2012, p. 10-32.
[28]. Yanju Liu, Ravi Naidu, Hui Ming - *Red mud as an amendment for pollutants in solid and liquid phases*, Geoderma, 163, 2011, p. 1-12.
[29]. Shaoxin Yang, Yihe Zhanga, Jiemei Yu, Taizhong Huana, Qi Tang, Paul K. Chu, Lei Qi - *Multi-functional honeycomb ceramic materials produced from bauxite residues*, Materials Design, 59, 2014, p. 333-338.
[30]. Anuj Kumar, Sanjay Kumar - *Development of paving blocks from synergistic use of red mud and fly ash using geopolymerization*, Construction and Building Materials, 38, 2013, p. 865-871.
[31]. Jaana Sorvari, Margareta Wahlstrom - *Handbook of Recycling*, 2014, p. 231-253.
[32]. L. Pérez-Villarejo, F. A. Corpas-Iglesias, S. Martínez-Martínez, R. Artiaga, J. Pascual-Cosp - *Manufacturing new ceramic materials from clay and red mud derived from the aluminium industry*, Construction and Building Materials, 35, 2012, p. 656-665.
[33]. Y. Pontikes, C. Rathossi, P. Nikolopoulos, G. N. Angelopoulos, D. D. Jayaseelan, W. E. Lee - *Effect of firing temperature and atmosphere on sintering of ceramics made from Bayer process bauxite residue*, Ceramics International, 35, 2009, p. 401-407.
[34]. Nevin Yalçın, Vahdettin Sevinç - *Utilization of bauxite waste in ceramic glazes*, Ceramics International, 26, 2000, p. 485-493.
[35]. Indrani Ghosh, Saumyen Guha, R. Balasubramaniam, A. V. Ramesh Kumar - *Leaching of metals from fresh and sintered red mud*, Journal of Hazardous Materials, 185, 2011, p. 662-668.
[36]. Laura Santona, Paola Castaldi, Pietro Melis - *Evaluation of the interaction mechanisms between red muds and heavy metals*, Journal of Hazardous Materials, B136, 2006, p. 324-329.
[37]. Ramesh Chandra Sahua, Rajkishore Patel, Bankim Chandra Ray - *Removal of hydrogen sulfide using red mud at ambient conditions*, Fuel Processing Technology, 92, 2011, p. 1587-1592.
[38]. Shaobin Wang, H. M. Ang, M. O. Tadé - *Novel applications of red mud as coagulant, adsorbent and catalyst for environmentally benign processes, a review*, Chemosphere, 72, 2008, p. 1621-1635.
[39]. Roach G. D., Jamieson, E., Pearson N., Yu A. B. - *Effect of particles characteristics on the solids density of Bauer red mud slurries*, Light Mnetlas, Anjier, J. L. Ed. TMS, New Orleans, 2001, p. 51-58.
[40]. Grafe M., Power G., Klauber C. - *Review of bauxite residue alkalinity and associated chemistry*, Light Metals, CSIRO Document DMR-3610, May 2009.
[41]. Florea Oprea, I. Constantin, R. Roman, D. Taloi - *Teoria proceselor metalurgice*, Editura Didactică şi Pedagogică Bucureşti, 1978, p. 372.

THE ANNALS OF "DUNAREA DE JOS" UNIVERSITY OF GALATI
FASCICLE IX. METALLURGY AND MATERIALS SCIENCE
N^0. 2 – 2014, ISSN 1453 – 083X

IMPROVING BIOCOMPATIBILITY OF Co-Cr ALLOY USED IN DENTISTRY BY SURFACE MODIFICATION WITH ELECTROCHEMICAL METHODS – CORROSION OF UNTREATED Co-Cr ALLOY IN SOLUTION WITH DIFFERENT pH

Eliza DĂNĂILĂ[1], Iulian BOUNEGRU[1,2], Lidia BENEA[1,*]
Alexandru CHIRIAC[2]

[1]Research (Competences) Centre: Interfaces-Tribocorrosion and Electrochemical Systems(CC-ITES), Faculty of Materials and Environmental Engineering, Dunarea de Jos University of Galati, 47 Domneasca Street, 800008 Galati, Romania
[2]Faculty of Medicine and Pharmacy, Dunarea de Jos University of Galati, 47 Domneasca Street, 800008 Galati, Romania
[*]Corresponding author
e-mail: Lidia.Benea@ugal.ro

ABSTRACT

The use of metals and alloys in dentistry has seen remarkable progress due to the deep research on their biocompatibility or the application of advanced technologies to improve surface properties by controlling material/environment interactions occurring in the mouth. The biocompatibility of metals and alloys is a consequence of the presence of the surface oxide layer. The chemical properties and therefore the interface chemical processes are determined precisely by this oxide layer and not the metal itself. The material response to changes in pH, to the application of force or the degrading effects of fluids may impair biocompatibility. Corrosion resistance, an important feature of the biocompatibility, can be verified by studying the electrochemical behaviour of metals and alloys in specific environments. This paper presents some research results on the corrosion behaviour of Co-Cr biomaterial composition in aqueous solutions with different pH (Fusayama - Meyer artificial saliva, Hank's and Ringer's solutions, citric acid) given that many of chemical reactions in the mouth are extremely sensitive to the environmental pH. The electrochemical methods used (free potential, potentiodynamic curves and cyclic polarization) are relevant methods for studying interactions of materials - specific environment of use/exploitation. Research has shown different behaviour of the alloy according to the pH, the chloride content and the oxidizing nature of the environment.

KEYWORDS: Co-Cr dental alloy, pH values, corrosion resistance, simulated saliva, electrochemical methods

1. Introduction

Metallic biomaterials are the most suitable for replacing failed hard tissue up to now. Co-base alloys are generally used in applications which require wear resistance, corrosion resistance and/or thermal resistance.

Cobalt chromium alloys can be basically categorized into two types: one is the castable Co-Cr-Mo alloy, which usually has been used for many decades in dentistry and recently, in making joints, and the other is the wrought Co-Ni-Cr-Mo alloy which is a relative newcomer now used for making the stems of prostheses for heavily loaded joints such as the knee and hip [1, 2].

Modern alloys based on Co-Cr due to superior mechanical properties and advantageous cost prices have replaced noble alloys of class IV in conventional technology (metal-polymer) and modern (metal and metal-ceramic composite). They are alloys with a high content of cobalt and their main alloying element is chromium.

Co-Cr alloys have an excellent corrosion resistance, which is provided by a thin adherent layer

and passive of chromium-based oxides with additions of Mo on the surface even in chloride environments [3-6]. Ly *et al.* [7] in their study report the identification of different Cr and Co species in the passive films formed under different potentiostatic conditions, which play important roles in alloy passivation. In this work was studied the corrosion behaviour of the Co-Cr alloy, in aqueous solution with different pH values, in particular as metallic biomaterial, because it is well known that in the body all vital processes take place at exact pH values.

2. Materials and methods

Electrochemical tests were performed on Co-Cr biomaterial alloy intended to be used for dentistry having the chemical composition and mechanical properties shown in Table 1.

In order to perform the corrosion tests, to the Co-Cr samples were applied contacts with copper conductors. After that, the samples were polished successively with waterproof abrasive paper with grain size from 320 - 4000 mm, with diamond paste of dimensions 3 - 1 μm and a suspension of SiO_2 (particle size 0.04 μm), finally achieving a mirror surface. Polished samples were cleaned with ethanol and then dried with hot air and stored in a desiccator. The active surface of the Co-Cr samples tested for corrosion was 0.5 cm^2. The electrochemical cell (Fig. 1b) used for corrosion experiments consisted of: biomaterial – Co-Cr alloy which served as the working electrode (WE), an Ag/AgCl electrode (saturated solution of KCl, E=200 mV/NHE) as reference electrode (RE) and a Pt-Rh grid as the counter electrode (CE). The composition of the tested solutions used in the corrosion experiments is presented in Ttable 2. Three types of simulated body fluids (SBF) were selected, namely Fusayama Meyer artificial saliva (pH = 5), Hank's solution (pH = 7.4) and Ringer's solution (pH = 6.6) in order to study the corrosion behaviour of the Co-Cr alloy as metallic biomaterial. The reason of using another type of environment (other than SBF), such as citric acid is that this medium is a powerful oxidant and has a lower pH value (pH = 1.8). This acid environment can influence the state (the formation, growth) of the oxide layer on the surface of the sample. Citric acid was also selected to study the corrosion of the alloy with biomedical destinations as it is found in citrus juice, apples, pears, cherries, raspberries, currants, in conifers, fungi, leaf tobacco, wine and even in milk, and can affect the composition change and the pH of the mouth cavity. For the investigation of the corrosion processes there have been used different analysis techniques such as: open circuit potential of the electrode (OCP), potentiodynamic polarization curves (PD) and cyclic polarization curves (CV). These testing techniques of corrosion were applied with a potentiostat/galvanostat VoltaLab PGZ 100, with interface to computer - soft VoltaMaster 4 (Fig. 1a).

Table 1. *Chemical composition and mechanical properties of the Co-Cr alloy Co-Cr alloy*

Chemical composition, [%]								
Standard EN 10204 -3.1B	Co	Cr	Mo	Mn	C	Fe	Si	Sonstige
Max. [%]	63	29.4	5.95	0.6	0.29	0.05	0.7	0.1
Phisico-mechanical Properties								
Density [g/cm^3]		Hardness, HV10		Modulus of elasticity, (E) [MPa]				
8.3		420		230				

Table 2. *The chemical composition of the electrolyte used in the corrosion tests*

Components	**Hank's solution**	**Ringer's solution**	**Saliva Fusayama Meyer (SFM)**	**Citric acid**
NaCl	8.8 g/L	8.4 g/L	0.4 g/L	-
KCl	0.4 g/L	0.3 g/L	0.4 g/L	-
$CaCl_2$	0.14 g/L	0.29 g/L	0.8 g/L	-
$NaHCO_3$	0.35 g/L		-	-
$C_6H_6O_6$ (glucose)	1 g/L		-	-
$MgSO_4$ x $7H_2O$	0.2 g/L		-	-
KH_2PO_4 x H_2O	0.1 g/L		-	-
Na_2HPO_4 x $7H_2O$	0.06 g/L		-	-
NaH_2PO_4	-		0.79 g/L	-
Urea	-		1 g/L	-
$C_6H_8O_7$	-		-	0.5 M
pH	**7.4**	**6.6**	**5.0**	**1.81**

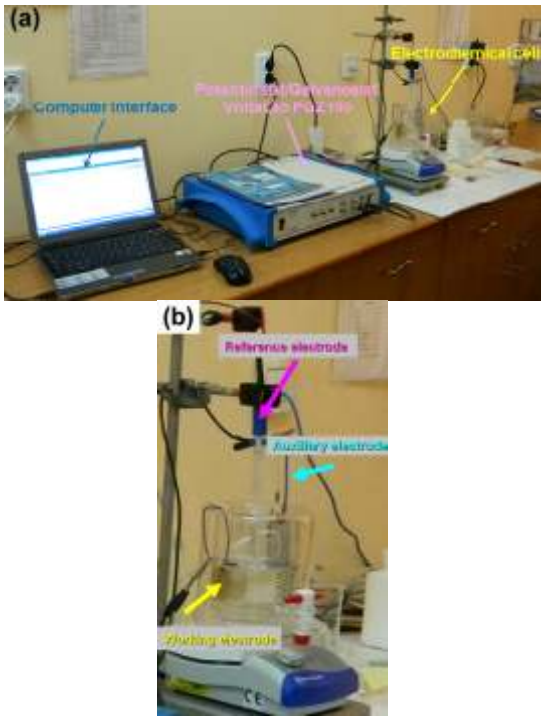

Fig. 1. *(a) Set-up used at the investigation of corrosion with the potentiostat/galvanostat VoltaLab PGZ 100 and (b) Electrochemical cell used during corrosion experiments*

3. Results and discussions

3.1. Evolution of open circuit potential during immersion

One of the ways to study the corrosion behaviour of the untreated Co-Cr alloy is to check the open circuit potential (OCP) as a function of time. This method indicates the oxidation tendency of a material to a corrosive environment. The potential can vary with time, as changes occur at the electrode surface (oxidation, formation of the passive layer or immunity). The potential-time measurements of the Co-Cr alloy in Hank's solution, Ringer's solution, Fusayama – Mayer saliva and citric acid, during 30 min. immersion time are shown in Fig. 2.

In Fig. 2 it can be seen a shift of the Co-Cr electrode potential towards electropositive values, which confirms the formation on the surface of a protective oxide film, for all studied environments. Also it is observed that in the case of citric acid solution, due to its composition without chlorides, even if the pH of the solution is reduced, this environment is a strong oxidant which leads to a shift of the Co-Cr electrode potential to more electropositive (more noble) values. As regards the three simulated body fluids (Hank's, Ringer's and SFM) due to different pH values and different chloride content, there are three levels with different values of potential stabilization. These values are inversely proportional to the pH values and directly proportional to the chloride content of solutions.

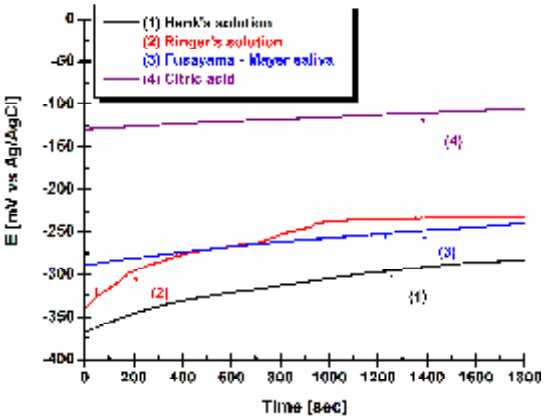

Fig. 2. *OCP time plots obtained for Co-Cr alloy in: (1) Hank's solution, (2) Ringer's solution, (3) Fusayama – Mayer saliva and (4) citric acid, during 30 min. immersion time*

Lower values of the OCP in Hank's solution, Ringer's solution and Fusayama – Mayer saliva can be explained by the presence of chloride ions that can be generated in long-term localized corrosion on passive alloys.

3.2. Potentiodynamic polarization curves

In order to assess the kinetics of the corrosion processes for the studied material, potentiodynamic polarization (PD) curves were measured at a scan rate of 5 mV/s, in the potential range between -1500 mV to +1200 mV vs. Ag/AgCl. Fig. 3 presents the polarization curves, current - potential (i - E) for the Co-Cr biomaterial studied immersed in the four solutions tested.

From this representation (Fig. 3) the Co-Cr alloy immersed in all four aqueous environments presents extended passive domains but between different potential domains corresponding to SBF environments, compared to citric acid solution. This behaviour of the Co-Cr alloy Co-Cr alloy in SBF environments indicates immunity to corrosion from the electrochemical point of view.

This type of diagrams (intensity-potential curves) recorded in a wide range of potential, from cathodic to anodic potential with a constant scan rate allow us to make some predictions on the material and testing environment. In these diagrams can be distinguished four domains, namely:

- cathodic domain, where the passive film is destroyed by hydrogen evolution;

- critical domain, where the passive film is formed in competition with the dissolution of the metal, being an instability domain;
- passive domain, where the passive film is formed and is characterized by a passive current density;
- transpassive domain, where dissolution of material takes place through the passive film.

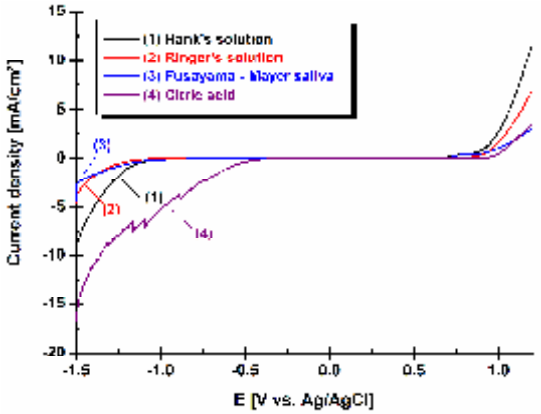

Fig. 3. *PD (current - potential) curves obtained for Co-Cr alloy in: (1) Hank's solution, (2) Ringer's solution, (3) Fusayama – Mayer saliva and (4) citric acid*

Usually the passive state is studied with respect to corrosion protection. If the passive state covers a higher potential domain and the passivation current value is smaller, then the metal or alloy shows a high corrosion resistance [8].

In Fig. 4 which shows a zoom of potentiodynamic polarization curves in the passive zone are observed the passive domains corresponding to tested solutions indicated by vertical arrows and their corresponding values. In Fig. 4 it can be seen a broad passivity domain for all three SBF studied, which is greater than 1 V, while the citric acid reveals a passive domain below 1 V. For the citric acid solution, the lower passivity domain around 0.972 V indicates that the Co-Cr alloy Co-Cr alloy is more susceptible to corrosion. The potential values in different domains and solutions are given in Table 3. Also the table provides the passivation current density of the Co-Cr alloy in the tested solutions according to passivation domain.

From these last diagrams (Figures 3 and 4) is noted the importance of solution composition and pH values on the passivity domain (immunity) of Co-Cr alloy biomaterial.

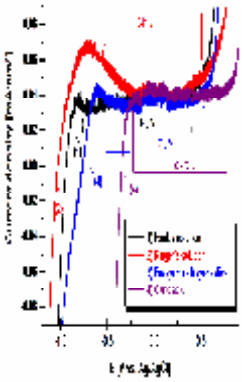

Fig. 4. *Identifying the passive domains on the PD curves for the biomaterial Co-Cr alloy immersed in four aqueous environments*

For the simple corrosion systems the corrosion reactions are strictly controlled by the charge transfer and the corrosion current density (i_{cor}). I_{corr} can be correlated with the polarization resistance (R_p) by the following relation:

$$i_{cor} = \frac{B}{R_p}$$

which represents the Stern – Geary equation for the evaluation of the corrosion resistance (in this case the corrosion rate is expressed in A/cm^2) and where B is a constant of the material – medium system given by the relation:

$$B = \frac{b_a|b_c|}{2{,}303(b_a + b_c)}$$

where, b_a and b_c are the Tafel slopes for the anodic and cathodic corrosion reactions.

Increasing the polarisation resistance means lower corrosion current density and thus a lower rate of corrosion.

Table 4 shows the results obtained for the polarization resistance and corrosion rates in the four solutions used.

Table 3. *The potential domains and the passivation current density of Co-Cr alloy for tested solutions*

Solution	Potential Domain, E [mV vs Ag/AgCl]				
	Cathodic domain	Critical Domain	Passive domain		Transpassive domain
			E	i_{pasiv} [μA/cm^2]	
Hank	< -940	-940 to -749	-749 to +394	36	> +394
Ringer	< -1030	-1030 to -533	-533 to +508	42	> +508
Fusayama Meyer saliva	< -764	-764 to -512	-512 to +524	36	> +524
Citric acid	< -344	-344 to -206	-206 to +766	41	> +766

Table 4. *The values of polarizations resistance and corrosion rates of Co-Cr alloy for tested solutions*

Solution	Polarization Resistance R_p [kohms cm^2]	Corrosion potential E [mV vs Ag/AgCl]	Corrosion rate i_{cor}	
			i_{cor} [mA/cm^2]	µm/year
Hank	3.0	-938	17.27	187.0
Ringer	3.08	-1027	36.80	398.8
Fusayama Meyer (SFM)	0.443	-902,6	14.16	153.3
Acid citric	1.69	-345	32.99	357.2

3.3. Cyclic polarization curves

By cyclic polarization method are recorded cyclic voltammograms on a selected potential range (typically starting from a negative value to a positive one) with a constant scan rate. If the reverse branch of the cyclic voltammograms shows lower currents than those of direct branch, then the material studied has a very stable passive behaviour. If the reverse branch shows higher current than those of direct branch at the same potential values it means that the surface is susceptible to pitting corrosion.

On the linear polarization diagrams are shown the different domains, current densities and corresponding potential states of "activity" and "prepassivity", followed by the "passive" (stable) and "transpassive" ones. Potential range for the passive state is between $E_p - E_{tp}$ with the passivation current density I_p. In the transpassive domain, the current density increases, because occurs a transpassive dissolution. In this domain, the passive film loses its protection properties and even disappears at higher potentials. From a practical point of view, the relative width of each domain and associated values depend directly on the material/environment system. The same material behaves differently in solutions with different pH.

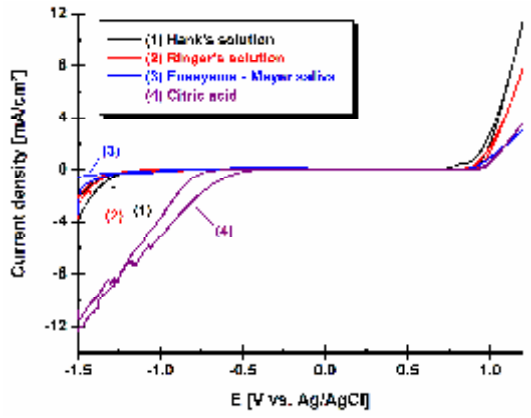

Fig. 5. *Cyclic voltammetry curves of the Co-Cr alloy immersed in four solutions with different pH*

Comparative cyclic polarization curves for the four tested solutions with different pH are presented in Fig. 5. Highlighting the localized corrosion susceptibility in the presence of chloride ions in the solutions can be seen very well due to the specific hysteresis aspect (Fig. 6) which presents the anodic transpassivation part of the curves from Fig. 5.

Localized corrosion or pitting corrosion is confined to a point or small hole within the metal. Pitting can initiate at sites where there are small surface defects such as a scratch or a dent, a small change in chemical composition of the alloy or damage to the oxide film. In the pit there is a rapid depletion of oxygen, and the pit behaves as a net anode, undergoing rapid dissolution. This anodic reaction produces electrons that are used further in oxygen reduction reactions at the external surface.

In Fig. 6 it is clearly observed that the Co-Cr alloy biomaterial shows pitting corrosion behaviour in Hank's solution, because of the specific hysteresis aspect. This behaviour can be explained by the presence of chloride ions in a higher concentration, which can generate in long-term localized corrosion on passive alloys.

The sizes of hysteresis domains are inversely proportional to the pH values and directly proportional to chloride content of solutions.

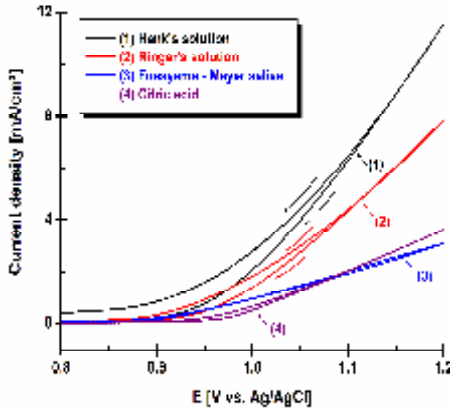

Fig. 6. *Cyclic voltammetry curves of the Co-Cr alloy immersed in four solutions with different pH: Zoom on the anodic part with the transpassive domain*

The generation of metal ions in the pit cavity leads to a net positive charge into the pit, resulting in an influx of chloride ions to maintain the charge balance. Hydrolysis of metal cations causes a decrease in pH. These factors promote pit growth, as high concentrations of chloride and hydrogen ions promote metal dissolution.

4. Conclusions

Material corrosion is a very important process to consider when choosing a material that must operate in a specific environment. Electrochemical methods used (open circuit potential, potentiodynamic polarization and cyclic polarization) are relevant methods to the study materials/operating environment interactions.

This paper presents the corrosion behavior in different simulating body fluids environments of Co-Cr alloy, biocompatible metallic material intended for dentistry. The interpretation of results according to open circuit potential and potentiodynamic polarization curves for the Co-Cr alloy biomaterial, immersed in four aqueous media, reveals that there are different levels of stabilization of the potential and different current densities depending on the pH value.

The Co-Cr alloy biomaterial showed a different behavior of corrosion tests in solutions with different pH, different content of chlorides and different oxidizing character.

The Co-Cr alloy biomaterial is very sensitive to localized corrosion (pitting) in Hank's solution, the localized corrosion being visible on the cyclic polarization curves even after the first hours of immersion.

Future work

The development of a new composite biomaterial suitable for bone implants by controlled anodic oxidation followed by electrodeposition of chitosan/hydroxyapatite. The anodisation of Co-Cr alloy leads to formation of a nanoporous oxide layer. By electrodeposition of chitosan/hydroxyapatite can be improved the capability of the interface for osseointegration, having simultaneously the protective properties of anodic growth oxide layer.

Acknowledgements

This work was financially supported by the Financing Contract *POSDRU//159/1.5/S/13896 - „Performanţă sustenabilă în cercetarea doctorală şi postdoctorală – PERFORM",* and partially by the research project PN II –PCE-10/2013 (HyBioElect) and Bilateral research project RO-FR, ANCS – Capacitati 702/30-04-2013 (CorrBioMat).

References

[1]. M. B. Nasab, M. R. Hassan - *Metallic Biomaterials of Knee and Hip - A Review*, Trends Biomater. Artif. Organs, 24, 2010, p. 69-82.

[2]. K.-H. Frosch, K. M. Stürmer - *Metallic Biomaterials in Skeletal Repair*, European Journal of Trauma, 2, 2006, p. 149-159.

[3]. J. Alvarado, R. Maldonado, J. Marxuach, R. Otero - *Biomechanics of hip and knee prostheses*, Mech., Mater.–I, INGE, 4011, 1, 2003, p. 1-17.

[4]. M. Navarro, A. Michiardi, O. Castaño, J.A Planell - *Biomaterials in orthopaedics*, J. R. Soc. Interface, 5, 2008, p. 1137-1158.

[5]. J. J. Ramsden, D. M. Allen, D. J. Stephenson, J. R. Alcock, G. N. Peggs, G. Fuller, G. Goch - *The Design and Manufacture of Biomedical Surfaces*, CIRP Annals-Manufacturing Technology, 56, 2007, p. 687-711.

[6]. R. Zupančič, A. Legat, N. Funduk - *Electrochemical and mechanical properties of cobalt-chromium dental alloy joints*, Materiali in tehnologije/Materials and technology Mater. Tehnol., 41, 2007, p. 295-300.

[7]. Y. S. Li, K. Wang, P. He P., B. X. Huang, P. Kovacs - *Surface - enhanced Raman Spectroelectrochemical Studies of Corrosion Films on Implant Co-Cr-Mo Alloy in Biosimulating Solutions*, J Raman Spectrosc, 30, 1999, p. 97-103.

[8]. L. Benea, E. Mardare-Danaila, M. Mardare, J.-P. Celis - *Preparation of titanium oxide and hydroxyapatite on Ti–6Al–4V alloy surface and electrochemical behaviour in bio-simulated fluid solution*, Corrosion Science, 80, 2014, p. 331-338.

THE ANNALS OF "DUNAREA DE JOS" UNIVERSITY OF GALATI
FASCICLE IX. METALLURGY AND MATERIALS SCIENCE
N^0. 2 – 2014, ISSN 1453 – 083X

WEAR BEHAVIOR OF CARBURIZING ON POWDER METALLURGY ALLOYS

Mihaela MARIN, Florentina POTECAŞU, Petrică ALEXANDRU, Octavian POTECAŞU, Elena DRUGESCU
"Dunarea de Jos" University of Galati, Romania
e-mail: mihaela.marin@ugal.ro

ABSTRACT

In this paper is studied the influence of wear behavior of carburizing in fluidized-bed on sintered alloys produced by powder metallurgy route. In powder metallurgy, carburization is a thermochemically treatment that occurs in the temperature range of 850-950 ºC and had a great importance to establish the correlation between porosity and carbon diffusion.

KEYWORDS: powder metallurgy**,** sintering, fluidized bed carburizing, abrasive wear

1. Introduction

Powder metallurgy is an alternative technology of lower cost process. The parts produced by powder metallurgy are of complex shapes and closed to final form, widely used, especially in the automotive industry [1].

The main problem of powder metallurgy products is the presence of pores. The pores acts as potential crack initiation sites, and can also guide and propagate cracks through the material. The properties of sintered powder metallurgy alloys can be improved by increasing the density, reducing pore size, or by adding alloying elements [2-4]. Copper, nickel, molybdenum, manganese and phosphorus are the most common alloying element added in powder form because of its low cost, availability and ability to improve the properties of alloys. Cu increase the toughness and density of the alloys by filling the pores due to melting during the sintering process (copper melts at 1083 °C). Another way to improve the properties of these alloys is by applying heat, thermochemical or mechanical treatments [5-13].

Fluidized bed carburizing is a thermochemical treatment that provides high heat and mass transfer. Due to the acceleration of the chemical reactions and diffusion, the fluidized bed has a rapid heating rate [7-10].

In this paper, the wear behavior of carburized in fluidized bed sintered alloys are analyzed.

2. Experimental procedure

The specimens studied in this paper are represented by atomized iron powder and pre-alloyed iron base powder. The chemical composition of the powders, pure iron and iron-based prealloyed powder with Cu, Ni and Mo is presented in table 1.

After being blended, the powders were uniaxially compacted into specimens, using an universal mechanical testing machine at ambient temperature The samples were pressed in a mold using uniaxial pressing. The applied pressure was 600 MPa and the disc specimens have the dimensions of $\phi 8 \times 6$ mm. The samples were mixed with 1% zinc stearate.

Table 1. *Chemical composition of analyzed powders*

Powder type	Cu	Mo	Ni	C
P_1	0.096	0.008	0.046	<0.01
P_2	1.50	0.50	4.00	<0.01

After compaction, the green samples were subjected to sintering. The sintering temperature was approximately 1.150 °C and the sintering time was 60 minutes. After cooling to room temperature the samples were subjected to gas carburizing treatment. The fluidized bed carburizing conditions were heating

at 900 °C during 60 minutes. Specimens were then air-cooled to room temperature. The samples subject to fluidized bed carburizing were tested for abrasion wear test (Fig. 4b). The SiC particles on the abrasive papers were the size of 80 µm and the load applied was 855 g. The distance traversed in each case was limited to 150 cycles corresponding to 76.5 m. The samples were cleaned and weighed using a precision balance before and after each test. Also, after the abrasive wear tests, the worn surfaces were examined by optical microscope, to evaluate the wear mechanism of the material. Also, the microhardness values of the sintered and carburized in fluidized bed alloys were analysed to correlate the wear behavior of this specimens.

3. Results and discussions

Optical micrographs representative of carburized samples are presented in figures 1 and 2. The microstructure of carburized samples was observed by optical microscopy (Olympus BX 50). Due to prolonged time in carburized, the samples were completely enriched in carbon. In sample P_2 with 4%, were evidence the presence of Ni-enrich areas.

Microstructures of specimens subject to carburized in fluidized bed consist in ferrite with pearlitic grains, cementite and Ni-enrich areas.

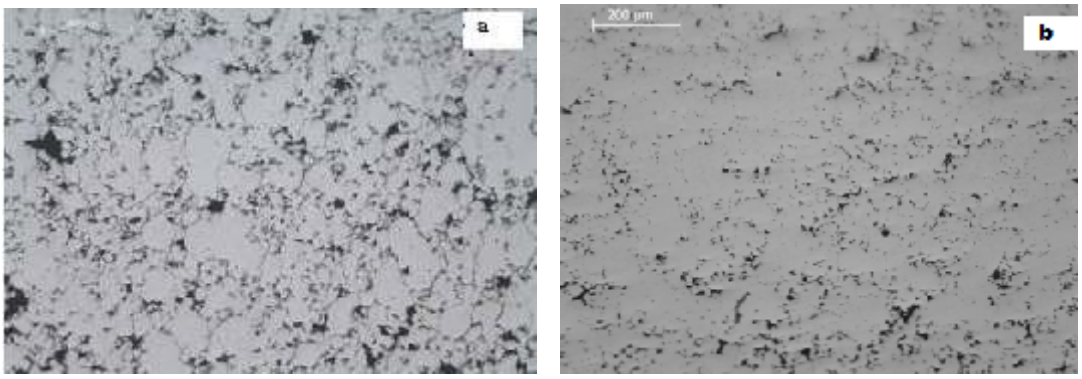

Fig. 1. *Image of the microstructure of carburized samples, unetched, 200x: a) P_1, b) P_2*

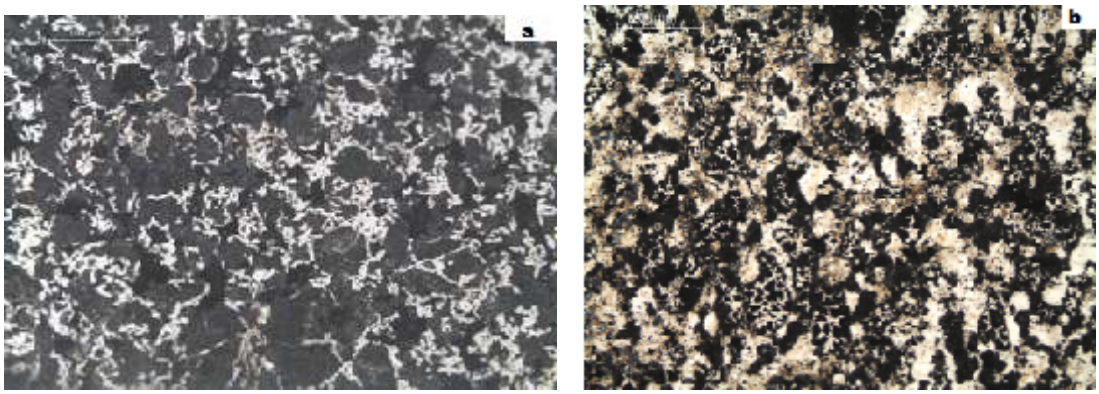

Fig. 2. *Image of the microstructure of carburized samples, etched Nital 2%, 200x: a) P_1, b) P_2*

Microhardness values of the sintered and carburized in fluidized bed alloys were analysed. The microhardness tests were performed by measuring Vickers microhardness, the applied load was 100 and the penetrator was a diamond pyramid. The microhardness was the average of three indentations on the top and anothers three on the bottom surfaces of each samples. Table 2 reports the values of microhardness of studied specimens. It is obvious that the sample P_2 with 4% Ni has the highest microhardness value because the Ni-enriched areas offers local ductility and have a positive influence on hardness and strength of sintered and carburized materials [18]. The worn surfaces of carburized samples after abrasion tests were examined in optical microscope, the typical aspects of abraded surfaces are represented in figure 3. The depth and width of wear grooves of carburized samples P_1 are greater compared to samples P_2.

The wear rate of carburized in fluidized bed specimens was measured as the weight loss, sample P_2 provided the less weight loss.

Table 2. *Microhardness values of sintered and carburized samples*

Sample type	Microhardness Vickers values for sintered samples [daN/mm^2]	Microhardness Vickers values for carburized samples [daN/mm^2]
P_1	161	403
P_2	178	709

Table 3 presents the weight loss of the carburized samples tested to abrasive wear.

Table 3. *Weight loss of carburized samples*

Sample type	Weight loss [g]
P_1	0.16
P_2	0.98

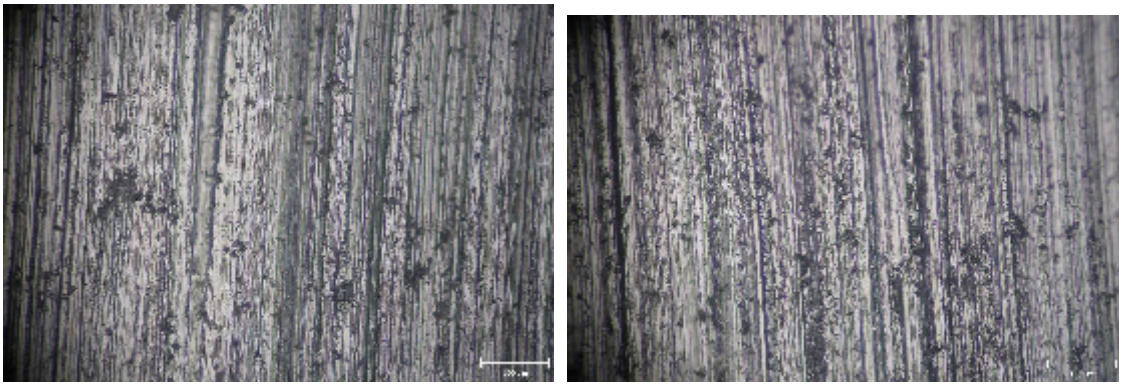

Fig. 3. *Optical photomacrographs of worn surfaces for carburized in fluidized bed samples (x200): a) P_1, b) P_2*

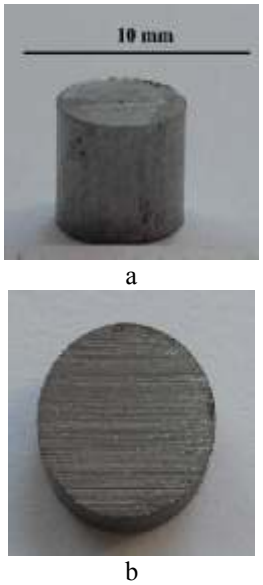

a

b

Fig. 4. *Aspect of initial and worn surface after the abrasion test of carburized in fluidized bed specimens*

4. Conclusions

The following main results were obtained:

- Abrasive wear surfaces for both types of powders presents deeper traces in unalloyed sample and finer trace in samples alloyed P_2, according with the aspects of the surface.

- The carburized sample P_1 presents a depth and width of wear grooves greater, thus there is a possibility of less resistance offered.

- The sample P_2 with 4% Ni has the highest microhardness value because the Ni-enriched areas offers local ductility and have a positive influence on hardness and strength.

- The weight loss is less for the sample P_2 subject to carburized in fluidized bed.

References

[1]. G. B. Jang, M. D. Hur, S. S. Kang - *A study on the development of a substitution process by powder metallurgy in automobile parts*, J Mater Process Technol, 110-5, 2000.

[2]. M. W. Wu, L. C. Tsao, G. J. Shu, B. H. Lin - *The effects of alloying elements and microstructure on the impact toughness of powder metal steels*, Materials Science and Engineering: A 538, p. 135-144, DOI:10.1016/j.msea.2011.12.113.

[3]. N. Maheswari, S. Ghosh Chowdhury, K. C. Hari Kumar, S. Sankaran - *Influence of alloying elements on the microstructure evolution and mechanical properties in quenched and partitioned steels*, Materials Science and Engineering: A, 600, 2014, p. 12–20.

[4]. S. Trivedi, Y. Mehta, K Chandra, P. S. Mishra - *Effect of carbon on the mechanical properties of powder-processed Fe–0·45 wt.% P alloys*, Indian Academy of Sciences, vol. 35, part 4, 2010, p. 481-492.

[5]. S. Mansoorzadeh, F. Ashrafizadeh - *The effect of thermochemical treatments on case properties and impact behaviour of Astaloy CrM*, Surface and Coatings Technology, vol. 192, Issues 2-3, 2005, p. 231-238.

[6]. J. Kazior, C. Janczur, T. Pieczonka, J. Ploszczak - *Thermochemical treatment of Fe–Cr–Mo alloys,* Surface and Coatings Technology, vol. 151-152, 2002, p. 333-337.
[7]. I. D. Radomyselsk, A. F. Zhornyak, N. V. Andreeva, G. P. Negoda - *The pack carburizing of dense parts from iron powder,* Powder metallurgy and metal ceramics, vol. 3, p. 204-211.
[8]. G. Krauss - *Principles of Heat Treatment of Steels*, American Society for Metals, ASM International, 2003.
[9]. J. Georgiev, T. Pieczonka, M. Stoytchev, D. Teodosiev - *Wear resistance improvement of sintered structural parts by C_7H_7 surface carburizing*, Surface and Coatings Technology, vol. 180-181, 2004, p. 90-96.
[10]. M. Sulowski - *How processing variables influence mechanical properties of PM Mn steels?*, Powder Metallurgy Progress, vol. 7, no 2, 2007.
[11]. M. Askaria, H. Khorsand, S. M. Seyyed Aghamiric - *Influence of case hardening on wear resistance of a sintered,* http://www.sciencedirect.com/science/article/pii/S0925838811005962 - hit2 *low alloy steel,* Journal of Alloys and Compounds, vol. 509, issue 24, 2011, p. 6800-6805.
[12]. Dobrzański L. A., Otreba J., Grande M. A., Rosso M. - *Microstructural characteristic and mechanical properties of Ni-Mo-(W) steels*, vol. 18, issue 1-2, Jamme, 2006.
[13]. G. Krauss -, *Microstructure residual stress and fatigue of carburized steels*, in: Proceedings of the Quenching and Carburizing, The Institute of Materials, p. 205-225, 1991.
[14]. O. P. Modi, D. P. Mondal, B. K. Prasad, M. Singh, H. K. Khaira - *Abrasive wear behaviour of a high carbon steel: effects of microstructure and experimental parameters and correlation with mechanical properties*, Mater. Sci. Eng., 343, 235, 2003.
[15]. K. V. Sudhakar, P. Sampathkumaran, E. Dwarakadas -, *Dry sliding wear in high density Fe-2% Ni based P/M alloys*, Wear, 242, p. 207-12, 2000.
[16]. H. Khorsand, S. M. Habibi, K. Janghorban, H. Yoozbashizade, S. Reihani - *Fatigue of sintered steels (Fe-1.5 Mo-3 Mn-0.7 C)*, Materials and structures, vol. 37, number 5, p. 335-341, 2006.
[17]. A. Sundstrom, Rendon, M. J. Olsson - *Wear behaviour of some low alloyed steels under combined impact abrasion contact conditions*, Wear 250, p. 744, 2001.
[18]. M. Sulowski - *Structure and mechanical properties of sintered Ni free structural parts*, Powder Metallurgy, vol. 53, no. 2, p. 125-140, 2010.

THE ANNALS OF "DUNAREA DE JOS" UNIVERSITY OF GALATI
FASCICLE IX. METALLURGY AND MATERIALS SCIENCE
N^0. 2 – 2014, ISSN 1453 – 083X

STUDY RELATED TO IMPROVE PERFORMANCE OF A NEUTRALIZING GAS DYNAMICS SYSTEM

Vasile BĂLAN[1], Marian BORDEI[2*]
[1]Academia Tehnica Militara Bucuresti
[2]Dunarea de Jos University of Galati, Romania
[*]Corresponding author
email: mbordei@ugal.ro

ABSTRACT

Worldwide, the series of attacks "with bomb" are the most common, accounting for over 80% of terrorist attacks. The many constructive solutions of Improvised Explosive Devices (I.E.D), would require for defusing sequence at least as many variations of cancellation. To anticipate in a shorter time (intervention time) the manner in which an explosive device was made (possibly, up to several months) is another factor leading to the adoption of a uniform neutralization solution by mechanical disruption (mechanical separation of the constituent elements of a hand made explosive device, using different agents of disruption). In this paper, we analyzed the possibility to improve performance of a neutralizing gas dynamics system.

KEYWORDS: explosive device, disrupter, gas dynamics system

1. Introduction

Nowadays, it is unanimously accepted the fact that there are no precise methods and certain solutions, infallible, in the activity of neutralization the improvised explosive devices. It is worth mentioning the difference in content between the neutralization activity of improvised explosive devices and the neutralization activity of industrial ammunitions (projectiles, bombs, grenades, fuses etc).

While at the improvised explosive devices the dissimulation, structure, way of working, are elements difficult to intuit and determine, at the industrial ammunitions, the shapes, constructive scheme, way of working, and destination are in majority known or well known.

Also, classic ammunition, except certain categories of mines or aircraft bombs are not equipped with "traps".

The existing cases demonstrate that, because of these "traps" in the organization of improvised explosive devices there are few who survived an attempt to defuse them. Given the technical, financial possibilities, material and technical knowledge base and experience possessed by bombers, it is accepted that the devices may be designed and constructed and practically impossible to be neutralized by conventional methods and manual defusing. In these circumstances, the only realistic option in dealing pyrotechnist - improvised explosive devices is the safe neutralization performed from the distance, in secure conditions, always following the people protection, reducing property damage and removing the uncertainty created.

2. The gas-dynamics system (disrupter)

The most used method for neutralize an improvised explosive device is generation of shock waves by means of the impact method between a projectile or a jet formed from diverse disrupting backgrounds and the improvised explosive device.

The neutralization systems (gas-dynamics systems) that propels the kinetic projectiles using explosives, are used to transmit large shocks to various inert or reactive targets.

These shocks have a significant impact on the targets, transmit changes in state and kinematic parameters, leading to either dismantling targets or initiating explosive charges receivers.

The gas-dynamics system (disrupter) is intended to neutralize improvised explosive devices. The neutralization is performed by pulling with the disruptor using different media (water, antifreeze, sand, shot, bolt penetration etc...). The propulsion of disruption media above mentioned on the improvised explosive device is made with electric pyrotechnic

cartouches CPE-127 000, cal. 12.7mm or specialized cartouches cal. 12 mm.

The system of improvised explosive neutralizing devices with DR-2 disrupters provides, during the specific interventions, the display in technical parameters for which it is intended, in the following environmental conditions:

- temperature: 30^0C ÷ 50^0C
- atmospheric pressure: normal
- relative humidity: normal

The technical - tactical features of the disruptor are:

- calibre: 30 mm;
- length: approx. 487 mm;
- clamping area diameter of the disrupter on cap DR-2 ϕ 49 mm;
- mass: approx. 6.5 kg;
- capacity: approx.200 cm^3;
- load thrown type: water, antifreeze, sand, balls (shot) metal bolt;
- ammunition: - electric pyrotechnic cartouche CPE -127-000 cal. 12.7 mm; special cartouche calibre 12;

The ammunition used in shooting with the disruptor are: electric pyrotechnic cartouche CPE-127000, cal.12,7 mm; flinging load standard is ω = 9 g of powder VUFL; depending on the nature of the mission we can prepare cartouches with increased load (up to 18 g); specialized cartouche cal. 12.

The initiation of the cartridges is electrical and it can be done depending on the mission, from the exploser or car battery. From measurements made on a sample of 6 cartouches, calibre type 12.7 mm, the values of the masses of constituents resulted are presented in Table 1.

Table 1. *Mass characteristics of the existent cartouche calibre 12.7 mm*

Cartouche No.	Total mass	Powder mass	Bure mass (sponge)	Stopper plug mass
	[g]			
1	78.25	9.640	0.451	1.329
2	77.37	9.016	0.450	1.331
3	76.3	8.992	0.456	1.325
4	79.0	9.737	0.451	1.336
5	78.8	9.744	0.448	1.332
6	78.3	9.757	0.453	1.343

3. Experimental test results

To determine the performance characteristics of the disrupter there were made experimental studies and shootings, we determined:

- initial velocity of the projectile (agent of disruption being water);
- variation of the pressure in the pipe with respect to time;
- geometry of the water jet; the influence of various parameters on the operation of the disrupter (plugs, the amount of water etc.);
- the intensity of the sound wave emitted from the operation of the system.

Once all the experimental configuration elements are ready, after checking the triggering and signal acquisition (including continuity of speed circuit), it proceeds as follows:

- insert the agent of disruption, measuring its volume in advance; water is introduced the same time with retaining plugs mounting (if applicable);
- insert the cartouche into the chamber, taking care that the hole gas loan to be is in adequate position;
- electronic acquisition system of pressure and velocity restarts;
- electric supply of the cartouche is applied;
- acquiring results (the curve of pressure variation and time between speed frames);
- filming the geometric configuration of the water jet propelled by the disruptor;
- processing the results of pressure and speed acquisition;
- acquiring pictures with the geometric configuration of the water jet propelled by the disruptor.

In the case of the ballistic tests we followed: materials used, initial conditions, jet speed, pressure, noise level. Pictures of the geometrical configuration of the water jet propelled by the disruptor during shooting, for first shooting, are presented in Figure 1, a-d. The evolution of pressure depending on time, for first shooting, is shown in Figure 2.

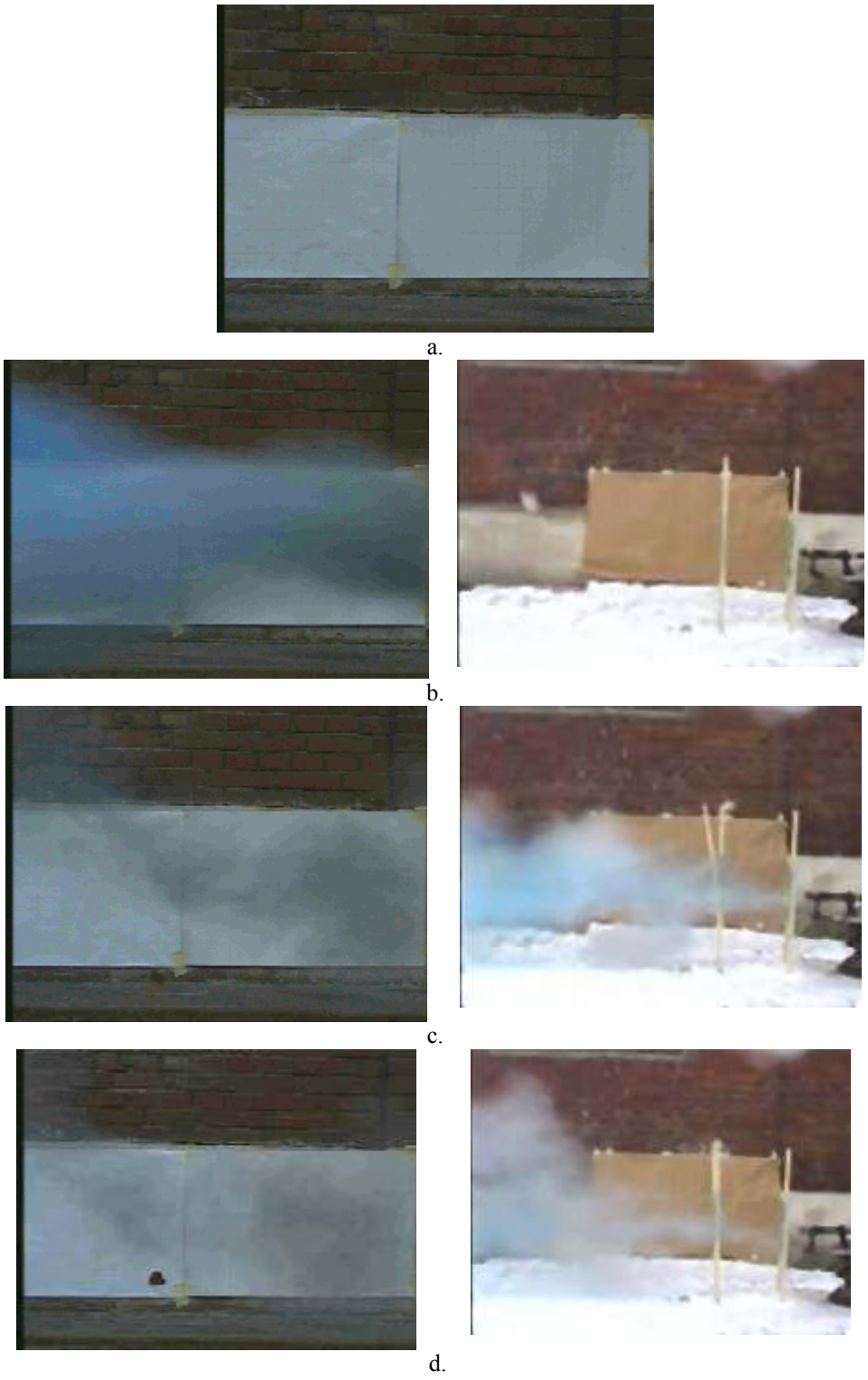

Fig. 1. *Analysis of the geometrical configuration of jets: images of the water jet, for first shooting: a. before shooting; b. after 40 ms; c. after 80 ms; d. after 120 ms*

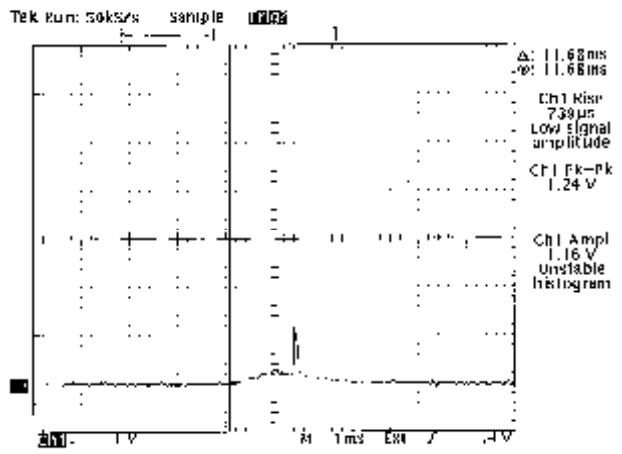

First shooting:

p_{max1}=1160 bar
t_{fl}=1.3 ms

Fig. 2. *Pressure versus time variation*

4. Conclusions

In the current use of the disrupter at the neutralization operations of some improvised explosive devices there have been found several shortcomings, such as:

- relatively heavy handling because of the entire mass system (hard-disruptor);
- initiating components pyrotechnic elements of some improvised explosive
- devices by the disrupting agent (electric detonating caps etc ...);
- the need for proximity to suspect parcel to obtain a good efficiency.

Given the assumptions presented, the results such as:

- explore the possibility of replacing the cartouche cal. 12.7 mm commonly used;
- study the ballistic characteristics of the existing cartouche:
- the initial speed of the jet and its geometric configuration;
- pressure value in loading chamber versus time;
- noise level produced at the load flinging initiation.

References

[1]. Goga, D. A. - *Probleme speciale de detonică*, Editura Academia Tehnică Militară, Bucureşti, 2008.
[2]. Kinney, G. F., Graham, K. I. - *Explosive Shocks in air*, Second Edition Poringer–Verlag Berlin Heidelberg, New York Tokyo, 1985.
[3]. Kistiakovsky, G. B., Wilson E. B. - *Teoria hidrodinamică a detonaţiei şi undele de şoc*, Report 114,1941.
[4]. Thevenin, M. - *Metode moderne în pirotehnie şi detonică*, Paris, 1972
[5]. Thevenin, M. - *Curs de detonică*, 1974.
[6]. Voicu V. - *Sisteme clasice pentru neutralizarea dispozitivelor explozive artizanale utilizate de specialişti din alte ţări*, a XIX – a Sesiune de Comunicări Ştiinţifice cu participare internaţională „NAV – MAR – EDU 2005", Constanţa, 2005.
[7]. Voicu V. - *Studiul dispozitivelor explozive artizanale şi al mijloacelor de neutralizare a acestora*, Referat 3, Academia Tehnică militară, Bucureşti, 2002.
[8]. Voicu V. - *Studiul teoretic şi experimental al propulsiei jeturilor de neutralizare prin deflagraţia pulberilor*, Bucureşti, Revista Tehnică Militară nr. 2, 2004.

THE ANNALS OF "DUNAREA DE JOS" UNIVERSITY OF GALATI
FASCICLE IX. METALLURGY AND MATERIALS SCIENCE
N^0. 2 – 2014, ISSN 1453 – 083X

THE INFLUENCE OF DIFFERENT COATINGS ON THE GRAPHITE DEGENERATION IN THE SUPERFICIAL LAYER OF IRON CASTINGS

Denisa Elena ANCA*, Elena PANCIU, Mihai CHIȘAMERA**
POLITEHNICA University of Bucharest, 313 Spl. Independentei, RO-060042, Bucharest, Romania
*corresponding author; **PhD – coordinator
e-mail: denisa_elena_anca@yahoo.com

ABSTRACT

The main objective of this experimenal reserch is to investigate new possibilities for reducing the graphite degeneration phenomenon in the superficial layer of iron castings.

For the experiment, a spheroidal graphite cast iron was poured in standard Quik-Cup moulds covered with various types of coatings. The sources of sulfur and oxygen used for coatings were based on FeS_2 and Fe_2O_3, respectively. After applying the coatings with sulfur or oxygen sources on the inner surface of the cups and after drying them, coatings based on iron powder and carbon containing powder respectively, were applied to block sulfur or oxygen access from the mould to the liquid iron. The coatings effect was evaluated by measuring the thickness of graphite degenerated surface layer and also by graphite nodularity and graphite shape factors deplating in the surface layer of the cast samples. The experimental results show a protective effect of the coating based on iron powder against the sulfur source while the coating based on carbon containing powder exerts a protective effect against the oxygen source.

KEYWORDS: coatings, graphite degeneration, superficial layer, sulphur, oxygen, iron powder, carbon containing powder

1. Introduction

The appearance of degenerated graphite layer phenomenon was observed with the first compacted graphite castings. A superficial layer in ductile iron castings can display a mixture of different graphite morphologies, from lamellar, compacted and spheroidal with various degrees of compactness up to a clear transition in the structure to fully spheroidal graphite [1, 2].

In ductile and compacted graphite irons, solidified with thin wall, the formation of an abnormal structure in the surface layer and its detrimental effect on mechanical properties has been documented over the years [3-9].

Various coating materials have been tested [10-12] to determine whether they can prevent deterioration in the surface structure. The severity of the abnormal surface layer has been significantly reduced, by employing CaO or MgO coatings due to a desulphurization reaction [11, 12].

To investigate new possibilities for reducing the graphite degeneration phenomenon in the superficial layer of the iron castings, the present work is especially focused on the evaluation of the influence of different coatings on the graphite degeneration in the superficial layer of the iron castings.

In this respect, a spheroidal graphite cast iron is developed. After the Mg treatment and CaBaFeSi inoculation, the iron melt was poured into standard Quik-Cup molds covered with various types of coatings. The metalographic samples were drawn for structure analysis.

2. Experimental procedure

The base iron was prepared by induction melting using a 150 kg acid coated induction furnace, at 1000 Hz frequency. As charge material 100% high purity pig iron was used while for iron melt chemical correction, high purity FeSi (90 wt.% Si) was added.

The thermal regim of iron melts processing was as follows: superheating temperature – T_s=1565 ^{o}C; Mg-treatment temperature - T_m=1530 ^{o}C; pouring temperature - T_p=1350 ^{o}C. The tehnical schedule of the experimental research program is presented in Fig. 1. FeSiCaMgRE (8 wt.% Mg) alloy as nodulizer was used (2 wt.% addition) while, for inoculation, CaBaFeSi75 (0.5 wt.% addition). The inoculated Mg-treated iron was poured in standard Quik-Cup resine molds [13] covered with various types of coatings. The materials used in this experimental program for creating the coatings are presented in Table 1. For metallographic analysis the cup samples were drawn [13]. The thickness of the surface layer was evaluated according to the schematic Fig. 2.a. with 100 µm between measurements on the unetched samples end 2% Nital etched samples.

The measured thickness of the surface layer is the average of all measurements. The structure in the healthy sample section was analized according to the schematic in Fig. 2.b. along 3 analysis directions, the distance between points in the same direction is the 0.66 mm. The average level of the structure parameters was calculated. Graphite nodularity was made in accordance with ISO 945 norm [14] after a previous metallographic preparation [13]. The main graphite shape factors analyzed are: circularity, sphericity, convexity and elongation [1].

Graphite morphology analysis was made by using a professional automat image analyzer using both the standard cast iron modulus and particle analysis software.

3. Results and discussions

The chemical composition of inoculated iron shows a level of Mg_{res} which suggests obtaining a ductile cast iron. The iron has a hypereutectic position - Table 2.

3.1. Effects on the surface layer thickness

On the etched samples were clearly obtained higher values of the average thickness of the degenerated graphite layer compared to the unetched samples. These differences are due to the difficulty in assessing the transition layer on the unetched samples and high sensitivity of metal matrix on this transition layer.

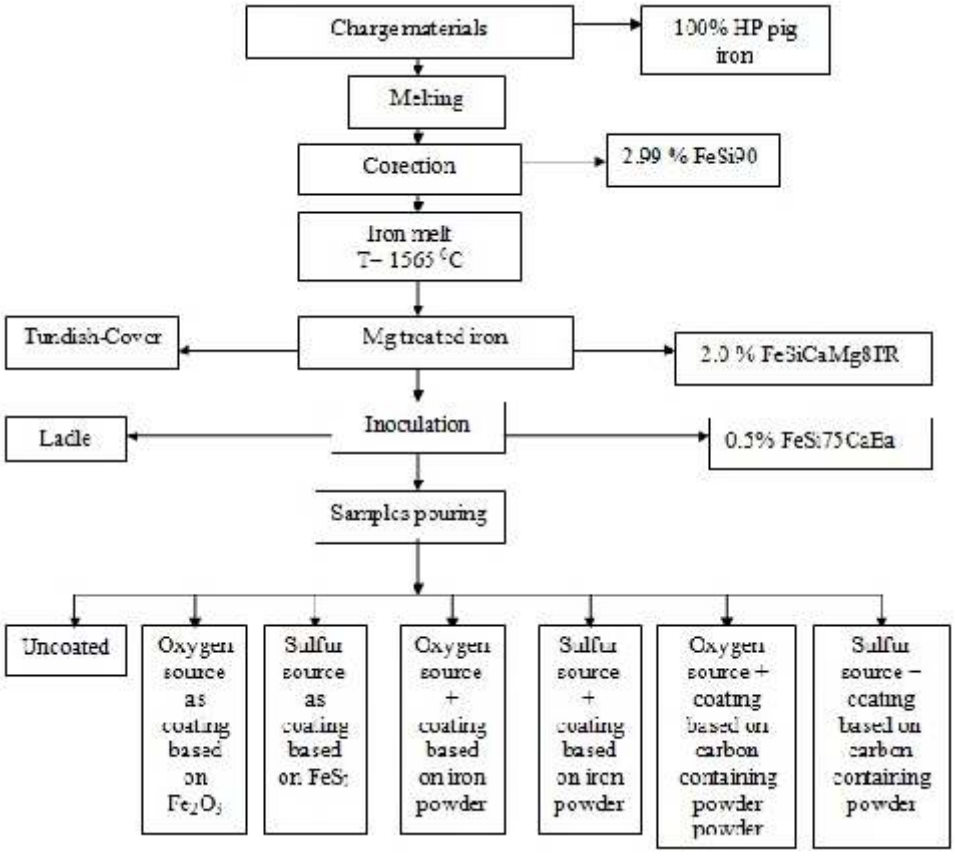

Fig. 1. *Technical schedule of the experimental program*

Table 1. *Dye coating materials*

Materials used for creating coatings	Binder
0.6 g FeS_2	- 4 g polystyrene - 10 ml toluene
0.6 g Fe_2O_3	
1.12 g iron powder	
1g carbon containing powder	

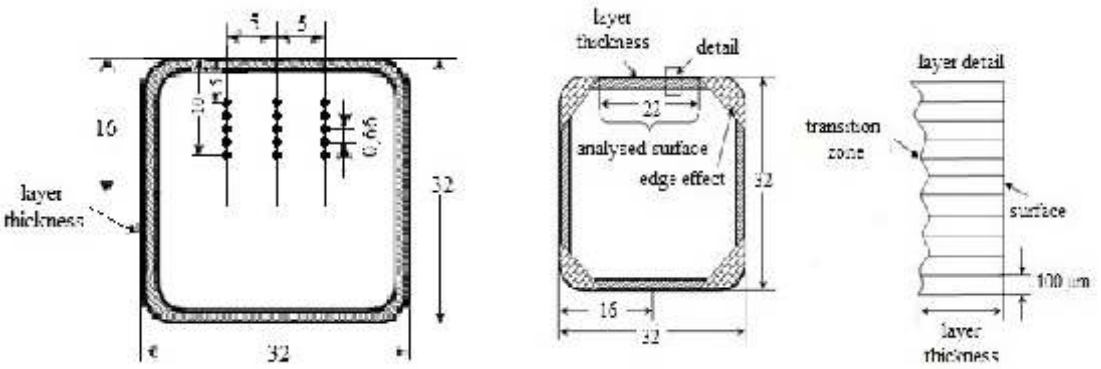

a) b)

Fig. 2. *The analysis procedure to evaluate the surface layer thickness (a) and the structure parameters in the healthy sample section (b)*

Table 2. *Chemical composition of obtained iron*

Chemical composition, [wt.%]*						CE**
C	Si	Mn	P	S	Mg	
3.65	3.15	0	0.013	0.004	0.049	4.6

*Others : Cr: 0.08, Mo: 0.05, Ni: 0.072, Al: 0.002, Cu: 0.02, V: 0.016, W: 0.004
**CE = C + 0.3·(Si + P) - 0.03·Mn + 0.4·S

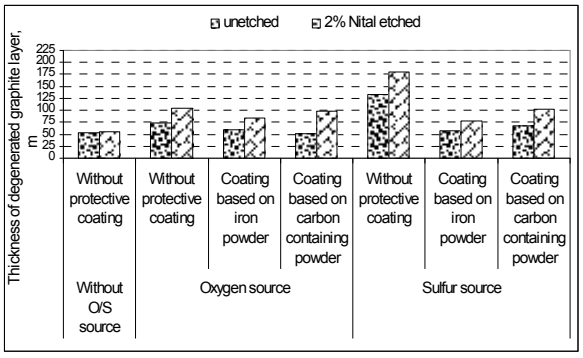

Fig. 3. *Influence of coatings on the surface layer thickness*

Samples protected with coating based on the iron powder or carbon containing powder showed lower values of the graphite degenerated superficial layer thickness compared to the unprotected (reference) samples (Fe_2O_3 or FeS_2 coated).

The largest thickness of the degenerated graphite layer was recorded for the unprotected (FeS_2 coated) sample which again highlights the strong influence of sulfur on graphite degeneration.

Coating based on iron powder shows a protective effect against the sulfur source while the coating based on the carbon containing powder shows a protective effect against the oxygen source (Fig. 3, Table 4).

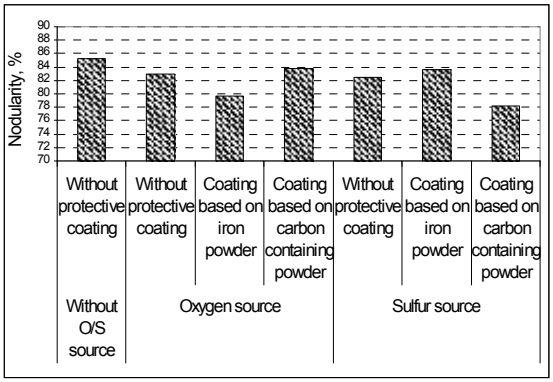

Fig. 4. *Graphite nodularity in healthy sample section under the influence of coatings*

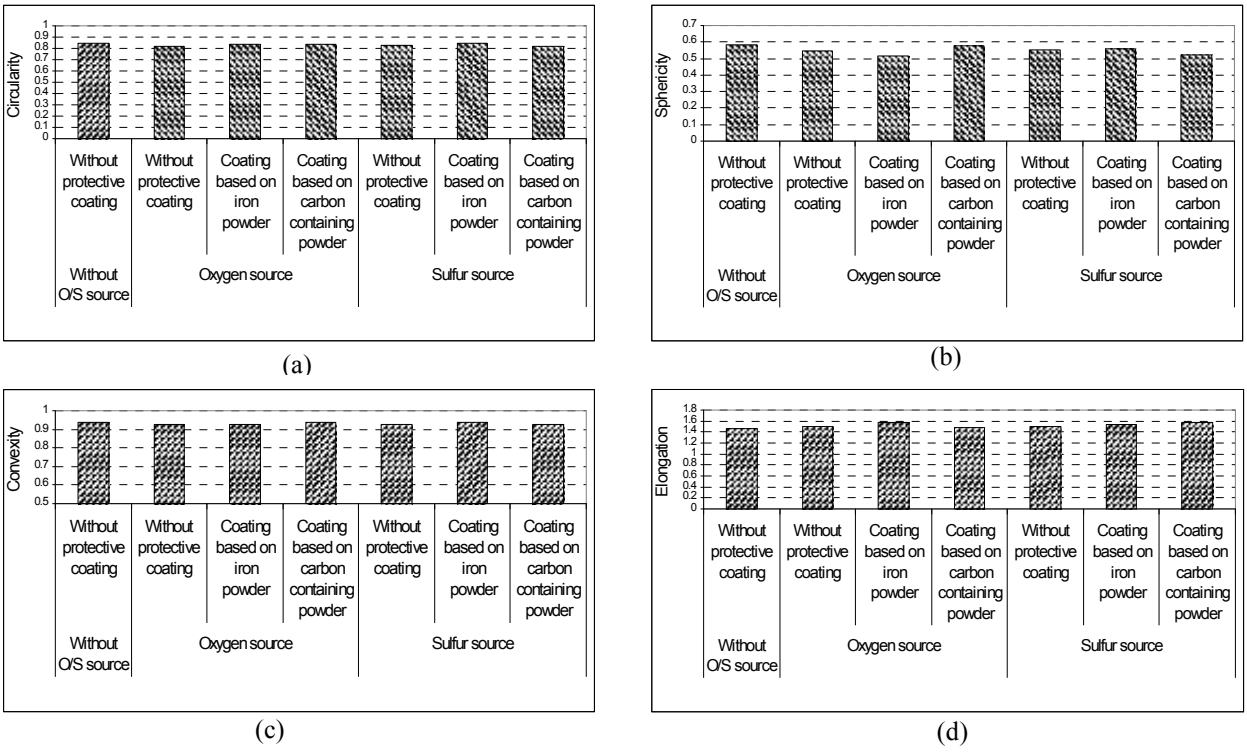

Fig. 5. *Graphite shape factors in healthy sample section under the influence of coatings: a - circularity, b - sphericity, c - convexity, d - elongation*

3.2. Effects on graphite morphology

Table 3. *Thickness layer evolution underthe influence of coatings*

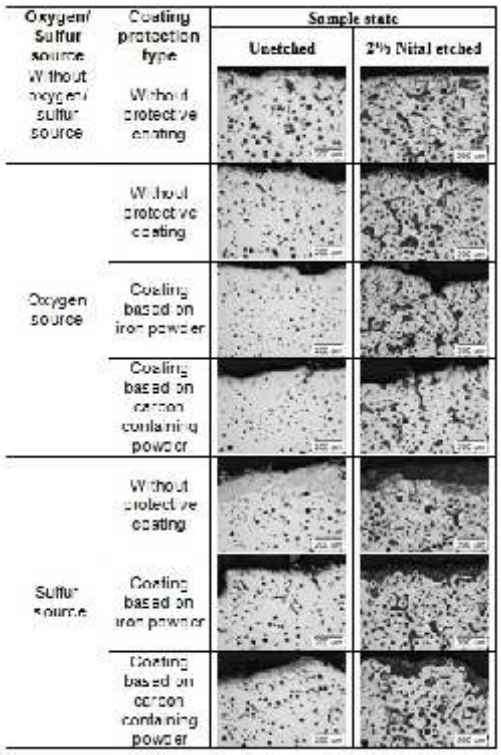

Graphite morphology was also affected by the experimented coatings in the healthy section of the samples. The influence of the O/S containing coatings without or with protective coatings on the graphite morphology (nodularity/graphite shape factors) is presented in Fig. 4 and Fig. 5.

As it can be seen in Fig. 4 and Fig. 5 result, coating based on iron powder has a protective action against the sulfur source (FeS_2), but does not exhibit the same effect against the oxygen source (Fe_2O_3) while the coating based on carbon containing powder has a reverse effect.

The effects on graphite morphology are in good connection with that on the graphite degenerated surface layer thickness. A higher thickness of degenerated surface layer means a lower graphite compactness (nodularity/shape factors) in the healthy section of the sample.

The explanation of these effects could be found if the different reactivities of the carbon towards oxygen and sulphur and the higher activity of oxigen towords the base iron components (C, Si Mn etc.) by comparing them to sulphur are taken into account.

The protective effect of the iron powder based coating could be explained by the decreasing of sulphur diffusion capacity on the sample – mould interface because of a lower sulphur gradient determined by the iron powder presence (sulphur diffusion effect).

4. Conclusion

(1) The experiment pointed out the much stronger degenarative effect of sulphur by comparing it to oxygen, objectified both through the size (thickness) of graphite degenerated superficial layer and graphite compactness decreasing in the sample volume.

(2) The coating of the sulphur source with iron powder coat has been shown to have a protective effect by lowering or eliminating the superficialy degenaration layer but it has been ineffective towards the oxygen source.

(3) The use of a carbon containing coat had an opposite effect compared to iron powder based coating that is, it had a protective effect towards de oxygen source but it was ineffective towards the sulphur source. The explanation of these effects consists in the different reactivity of S/O towards the main components of base iron and the different action of the two coats (iron powder and carbon containing powder) on the iron sample – mold interface.

Acknowledgement

The work has been funded by the Sectoral Operational Programme Human Resources Development 2007-2013 of the Romanian Ministry of Labour, Family and Social Protection through the Financial Agreement POSDRU/107/1.5/S/76903.

References

[1]. I. Riposan, M. Chisamera, S. Stan - *Performance of Heavy Ductile Iron Castings for Windmills*, China Foundry, 2010, vol. 7, Issue 2, p. 163-170.

[2]. I. Riposan, M. Chisamera, S. Stan, T. Skaland - *Surface Graphite Degeneration in Ductile Iron Castings for Resin Molds*, Tsinghua Science and Technology Journal, 2008, vol. 13, Issue 2, p. 157-163.

[3]. G. M. Goodrich, R. W. Lobenhofer - *Effect of Cooling Rate on Ductile Iron Mechanical Properties*, AFS Transaction, 2002, 110, p. 1003-1032.

[4]. S. Boonmee, D. M. Stefanescu - *Casting Skin of Compacted Graphite Iron Part II: Influence on Tensile Mechanical Properties*, AFS Transaction, 2010, 118, p. 217-222.

[5]. D. M. Stefanescu, S. Wills, J. Masson, F. Duncan - *Quantification of Casting Skin in Ductile and Compacted Graphite Iron and Its Effect on Tensile Properties*, International Journal of Metalcasting, 2008, p. 7-26.

[6]. S. Boonmee, M. K. Moran, D. M. Stefanescu - *On the Effect of the Casting Skin on the Fatigue Properties on CG Iron*, *AFS Transaction,* 2011, 119, p. 421-430.

[7]. S. Boonmee, D. M. Stefanescu - *The Effect of Nodularity and Surface Condition on the Fatigue Properties of CG Iron*, AFS Transaction, 2011, 119, p. 205-2016.

[8]. M. Kuwamoto, T. Iwamoto, T. Saeki - *The Effect of Skin on Fatigue Resistence of Cast Iron*, The Japan Society of Mechanical Engineers, 1951, vol. 17, no. 61, p. 139-142.

[9]. C. Labrecque, M. Gagne, P. Cabanne, P. Francois, C. Beret, F. Hoffman - *Comparative Study of Fatigue Endurance Limit for 4 and 6 mm Thin Wall Ductile Iron Castings*, International Journal of Metalcasting, 2008, p. 7-17.

[10]. J. Baier, M. Koppen - *Manual of Castings Defects. Incidence and Avoidance of Defects Attributable to Moldinf Sands*, Marl, Germany, IKO-Erbsloh, 1994, p. 32-35.

[11]. F. Marti, S. I. Karsay - *Localized Flake Graphite Structure as a Result of a Reaction between Molten Ductile Iron and Some Components of the Mold,* AFS Transactions, 1979, vol. 87, p. 221-226.

[12]. S. Morita, N. Inoyama - *Behavior of Nitrogen in Cast Iron*, AFS Cast Metals Research Journal, 1969, vol. 5, Issue 3, p. 109.

[13]. D. E. Anca, M. Chisamera - *Graphite morphology in Mg-treated iron - Sulphur and oxygen effect*, Metalurgia International, 2013, vol. XVIII, no. 5, p. 37-42.

[14]. N. Ivan, M. Chisamera, I. Riposan - *Influence of Magnesium Content and Coating Type on Graphite Degeneration in Surface Layer of Iron Castings in Resin Sand –P-Toluol Sulphonic Acid (PTSA) Moulds*, ISIJ International, 2012, vol. 52, no. 10, p 1848-1855.

THE ANNALS OF "DUNAREA DE JOS" UNIVERSITY OF GALATI
FASCICLE IX. METALLURGY AND MATERIALS SCIENCE
N^0. 2 – 2014, ISSN 1453 – 083X

RESIDUAL STRESS AND TRIBOLOGY BEHAVIOUR OF TiCx COATING DEPOSITED BY NPCVD METHOD

Stela CONSTANTINESCU
"Dunarea de Jos" University of Galati, Romania
e-mail: sconst@ugal.ro

ABSTRACT

In this paper, thin TiCx films were coated by chemical vapour deposition method, and various duty cycles were carried out in order to observe the influence of this parameter on residual stress and tribology behaviours. The duty cycles were 35, 43 and 50% at 500 ^oC operating temperature. Therefore, wear behaviour, hardness and chemical analyses of TiCx coating were characterised, and it was found that the residual stresses in the coating were compressive, which were- 1.14189 - 0.12985 and -0.1749 MPa at three different duty cycles, i.e. 35, 43 and 50% respectively. According to the results, the coating that was applied at 43% exhibited superior wear resistance and possessed the lowest friction coefficient of ~ 0.059 in a pin-on-disc test.

KEYWORDS: wear, residual stress, TiCx coating, NPCVD, duty cycle

1. Introduction

Titanium carbide (TiCx) coatings are well known for combining a number of special properties, which have made them of particular interest for a broad range of applications. They are used as wear resistant coating for cutting tools and inserts and diffusion barriers in semiconductor technology [1–3]. It has been established that the properties of TiCx microstructure coating strongly depend on the deposition conditions and elaboration methods [3]. There are a lot of methods to apply hard alloys coating, including chemical vapour deposition at low pressure (LPCVD), plasma assisted CVD (PACVD) and chemical vapour deposition at normal pressure (NPCVD); however, it is an appropriate method for the deposition of wear resistant coatings on temperature sensitive materials [4]. Normal presure CVD has the major advantage that coatings of uniform thickness and composition can be produced even on substrates with a complex shape at high temperature [3–8]. Further study has indicated that the properties of titanium carbide are related to its chemical composition and texture and are a result of low adhesion or residual stresses in the thin film [3–11]. The residual stress in thin film deposited by NPCVD may be either compressive or tensile, depending on the deposition conditions. However, applying TiCx microstructure coating on metals is so difficult, since this compound is metastable, and the reaction between atoms in the NPCVD method is complicated. Among several parameters with important effect on the properties of the TiCx microstructure coating, duty cycle plays an essential role as a thermodynamic and kinetic parameter.

More study showed that the duty ratio and pulse frequency affect the chemical deposition and that the processing rate can be improved [12–14].

Therefore, in the present paper, we studied the influence of duty cycle on the structure, morphology, chemical composition and tribological behaviour of TiCx.

2. Materials and methods

The alloy WC – Co was used as substrate material. Table 1 illustrates the results of chemical analysis accomplished by spark emission spectroscopy test. The samples of substrate with the dimension 18 x 18 x 5 mm were quenched and tempered to a hardness of 17 000 MPa. After being polished to a Ra of 2 μm using Al_2O_3 slurry, the samples were first cleaned with acetone and then cleaned in ethanol and a chemical process in Ar and H_2 before deposition.

3. TiCx coating deposition

The TiCx microstructure coating was deposited by NPCVD in a reactor using a HCl–CH_4–H_2–Ar gas mixture. The pressure in the reaction chamber amounted to 1 at. For more details concerning the

deposition conditions, see Table 2. The substrate temperature was achieved by auxiliary heating system. Three kinds of duty cycles including 35, 43 and 50% were selected for investigating the influence of duty cycle on residual stress and tribology behaviour of TiCx microstructure coating.

4. Characterisation of TiC microstructure coating

The surface morphology, uniformity and homogeneity of the coated samples were examined by (Philips) scanning electron microscopy (SEM) and atomic force microscopy (AFM), and also the coating thickness was measured by cross-section SEM analyses.

Micromechanical properties such as Young's modulus E and hardness HV of the TiCx microstructure coatings were evaluated by microindentation technique (TriboScope). The AFM was a MicroScope III, and the indentation time was set to 10 s. The sensor of the transducer recorded the values of normal force and depth. From the analysed load–displacement curves, the Young's modulus of the measured films can be calculated as follows.

$$1/E_r=2\beta/S(A_c/\pi)^{1/2} = (1-\upsilon^2_m)/E_m+(1-\upsilon^2_i)/E_i \quad (1)$$

where: Ac, Er, S and β denote the actual contact area, the reduced elastic modulus for each indenter/specimen combination, the measured stiffness and a shape constant of 1 for the Berkovich tip respectively.

The subscripts m and i denote the film and the indenter tip respectively, E is the Young's modulus, and υ is Poisson's ratio. The indenter properties used in this study's calculations are E_i = 1140 GPa and υ_i = 0.07, and the assumed Poisson's ratio of TiCx is υ_m = 0.17[8].

The crystalline structure of the coating was determined by X-ray diffraction (XRD) (using a Dron diffractometer in continuous scanning mode and using Mo, K_α radiation λ = 154056 μm).

Table 1. *Chemical analysis of widia achieved by spectroscopy test*

Composition	WC	Co
Weight per cent	0.94	0.06

The first part of this study is concentrated on using XRD for the purpose of characterising the TiCx microstructure coating with special emphasis on residual stress measurements, in which the stresses are measured using the conventional $\sin^2 \psi$ method [12, 13]; the second part of this study is devoted to investigate the effect of duty cycle on the tribology behaviour of the TiCx microstructure coating. The film composition was determined by X-ray photoelectron spectroscopy (XPS) using monochromatic Al K_α radiation. The adhesion of the TiCx microstructure coatings on hot working widia was analysed with a microscratch tester with a diamond tip (radius of 10 μm). The sliding speed was fixed at 15 μm s^{-1}. The critical load Lc was defined as the lowest load at which the TiCx microstructure coatings started to delaminate. The delamination of the coatings was confirmed through observation with an optical microscope. A pin on disc apparatus was carried out on the TiC microstructure coating under loading conditions of maximum 1 GPa pressure with Ø6 mm ball; this is the Hertzian pressure so close to the working condition, such as cutting and forming tools, [15–17]. The load was 5 N, and the sliding speed was 0.1 m s^{-1}. All the tests were performed for 1500 cycles. The temperature and relative humidity were 30 ^{o}C and 36% respectively. Before the tests, the samples were cleaned with ethanol and dried in hot air.

5. Results and discussion

The geometry of the test samples for each of the factor series summarised in Table 2 was kept the same, and also the positions in the process chamber were kept alike.

Table 2. *Process parameters for deposition of TiCx*

Parameter	**Value**
Temperature [^{o}C]	≤ 1050
Process time [h]	4
Ar +H_2 [L/h]	2.8
H_2 + CH_4 + HCl [L/h]	0.8
Duty cycle [%]	35, 43 and 50

In this work, titanium tetrachloride is obtained directly in the working chamber of the ferrotitanium and concentrated hydrochloric acid at elevated temperature (over 1000 ^{o}C) according to the reaction:

$$Ti_{(s)} + 4HCl \rightarrow TiCl_4 + 2H_2$$
$$TiCl_4 + CH_4 + H_2 \rightarrow TiC + 4HCl + H_2$$

It is noteworthy that the originality of the paper consists in direct titanium tetrachloride working inside, avoiding the import of this tetrachloride which shows a high toxicity.

Figure 1 demonstrates the XRD diffraction patterns for the deposited samples with three different duty cycles, i.e. 35, 43 and 50%. X ray diffraction is a well established technique for the measurement of residual stress in coatings [12].

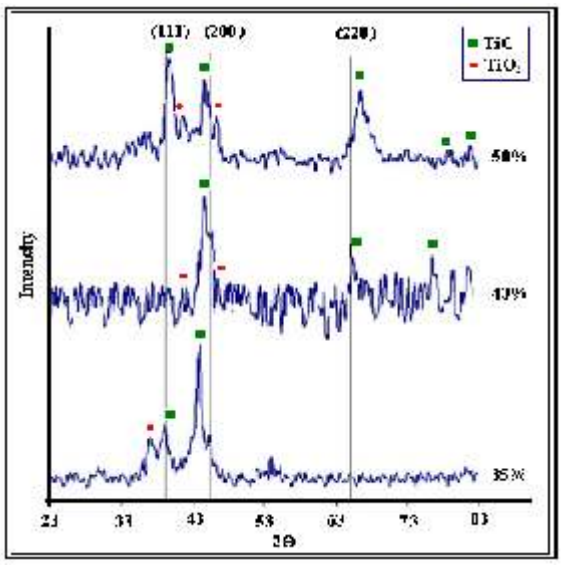

Fig. 1. *X-ray diffraction patterns for TiCx microstructure coating at three different duty cycles of 35, 43 and 50%*

As Fig. 1 shows, the (200) plane is the preferred structure; therefore, this result implies that the TiCx coating was deposited under a thermodynamically stable condition since the (111) structure (or texture) is the common structure of TiC that is observed.

The lowest energy surface for the TiCx crystal is the (200) plane and this is the structure that is expected for coatings deposited under thermodynamic equilibrium [14, 18]. In order to clarify the effects of duty cycle on the chemical composition of TiCx microstructure coatings.

Figure 2 displays the C 1s and Ti 2p XPS spectra of the TiCx microstructure coatings deposited at three different duty cycles. The Ti 2p XPS signal is composed of Ti $2p_{3/2}$ and Ti $2p_{1/2}$ doublets with binding energies of 455 • 2 and 460 • 8 eV respectively. These two doublets are separated by 6.0 eV. The C 1s spectrum shows a peak at 281.6 eV, and TiO_2 is represented by the Ti $2p_{3/2}$ peak at 458.4 eV. The existence of the Ti 2p and C 1s peaks indicates that the coating obtained under the deposition conditions (Table 2) is TiC.

Moreover, no significant variation of the surface chemical composition (C/Ti ratio) was observed with the increase in duty cycles.

As it was mentioned previously, the stresses in the TiC microstructure coatings were measured in the present paper using the conventional $\sin^2 \Psi$ technique [12].

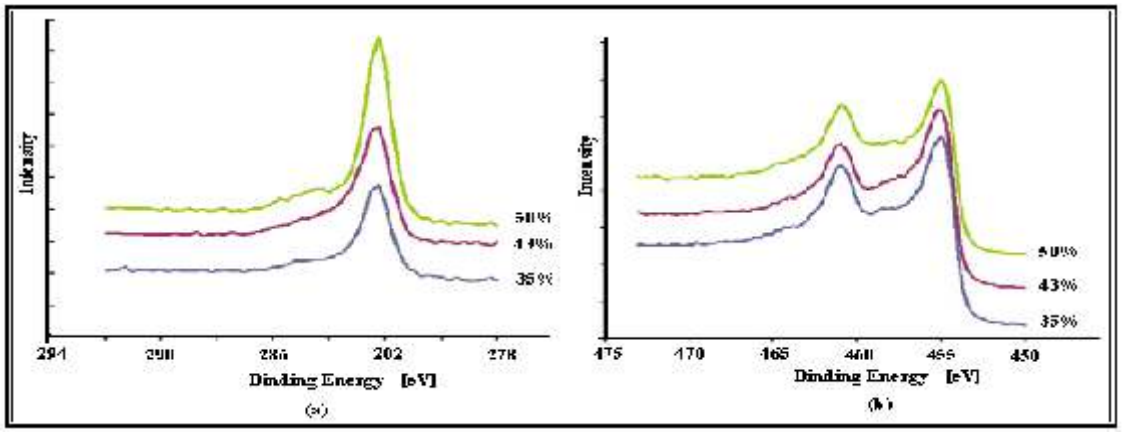

Fig. 2. *X-ray photoelectron spectroscopy spectra for surface of TiCx microstructure coatings deposited at three different duty cycles of 35, 43 and 50%: a) C 1s spectra peaks; b) Ti 2p spectra peaks*

It is supposed that the TiC microstructure coating under investigation can be considered homogeneous (in principle, preferential orientation free) and in a biaxial stress state. The residual stress can be deduced from the following relation (equation (2)):

$$\varepsilon = \sigma [(1+\upsilon)/E \bullet \sin^2 \Psi] - 2\upsilon/E] \qquad (2)$$

The critical load L_c was measured with a microscratch tester, and it is related to the adhesion strength of the TiC microstructure coating on hot working widia sample. The L_c values explained here were averaged for five times.

The results of residual stress in the TiC microstructure coating versus three different duty cycles are shown in Fig. 3.

The TiC microstructure coating deposited at 35% duty cycle has a relatively low adhesion strength compared to other duty cycle and increases the duty cycles from 35 to 43%, enhancing the adhesion strength from 18 to 36 mN, but following the

increasing duty cycle led to a decrease in adhesion strength from 36 to 27 mN. However, the adhesion strength was enhanced by increasing duty cycle. The low adhesion strength of the TiC microstructure coating at low duty cycle can be explained as a result of the internal stress with a high atomic density or the structural difference between films and substrates, its inherent brittle properties and chemical composition.

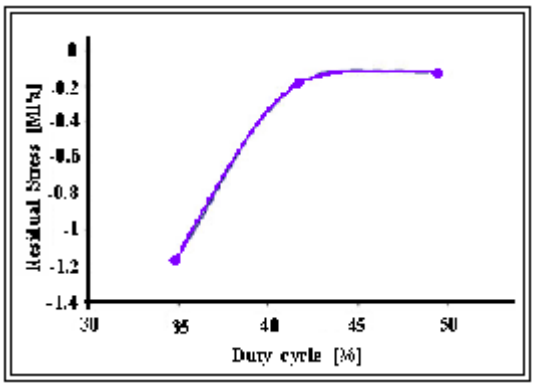

Fig. 3. *Residual stress of TiC microstructure coating as function of duty cycle*

5.1. Effect of duty cycle on residual stress

In Fig. 1, it can be observed that the increasing duty cycle from 35 to 43% has caused the (200) plane to be the preferred structure, and the TiO_2 phase was detected. It is clear that the detected peak was increased by rising duty cycles from 43 to 50%; moreover, the (200) and (111) planes are then the preferred structures. Actually, the various compounds between Ti–C and residual stress in the TiC microstructure coating cause a shift of peaks towards higher angles with increasing duty cycles from 35 to 50% [14, 18–20].

It should be mentioned that the residual stress in the TiC microstructure coating has an important role in forming the preferred orientation, and the latter is governed by the lowest overall energy conditions.

However, the best duty cycle to grow the (200) plane as a preferred orientation is 43%, the crystallite size of the TiC microstructure coating (which was calculated using the Scherrer formula) is 7 µm.

An evident change in grain size is observed for changing duty cycle.

Actually, the grain size of the TiC was decreased by rising the duty cycle from 35 to 50%, as raising the duty cycle leads to an increase in number of nucleation and cluster on the substrate. Finally, the grain size of the TiC microparticles is decreased accordingly.

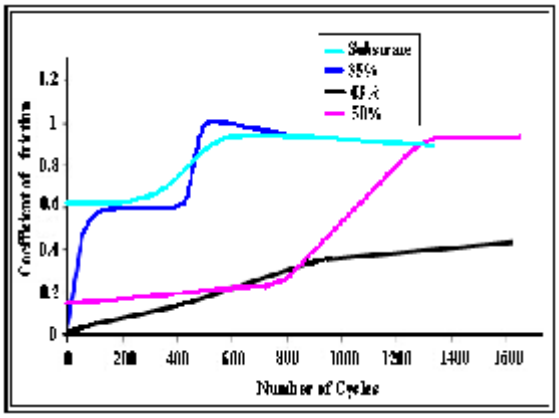

Fig. 4. *Friction coefficient of TiCx nanostructure coating versus number of cycles at three different duty cycles*

A sign of the preferred orientation has been achieved from measurements of the (111) and (200) reflections. As shown in Fig. 1, for all the coatings except for 50% duty cycle, the (200) direction is the preferred one with variations in the (111):(200) ratio ranging from 0 to 0.2.

Figure 2 illustrates that the residual stress in the TiCx microstructure coating is compressive, and the increasing duty cycle from 35 to 50% causes the compressive stress to drop from -1.14189 to -0.12985 MPa. It is usually believed that the residual stresses in a TiC microstructure coating are composed of the thermal stress component due to the difference in thermal expansion coefficients between the thin film and the substrate, which is created in the cooling stage from high temperature down to room temperature, as well as an intrinsic stress component depending on non-thermal origins.

Table 3. *Properties of TiC microstructure coating at three different duty cycles*

Duty cycle [%]	**Grain size** [µm]	**Thickness** [µm]	**Critical load** [mN]	**Hardness** [GPa]	**Residual stress** [MPa]
35	8.7	1.8	18	29.09	-1.14189
43	5.6	2.5	36	12.63	-0.12985
50	4.97	2.5	27	21.07	-0.1749

Fundamentally, the residual stress of the former origin in the TiC microstructure coating is an intrinsic stress component and is considered to depend strongly on the process parameters, such as duty

cycle, reactor pressure and operating temperature. This is speculated to be due to the more gradual crystal growth of the TiCx microstructure coating at 43 and 50% in comparison with the 35%, which may generate some intrinsic origins of the stress. In addition, it is believed that oxygen impurities lead to an increase in compressive stress in the TiC microstructure coating.

Figures 1 and 3 show the TiO_2 phase with TiC phase at 35%, and this impurity causes a rise in compressive stress rather than 43 and 50% duty cycle.

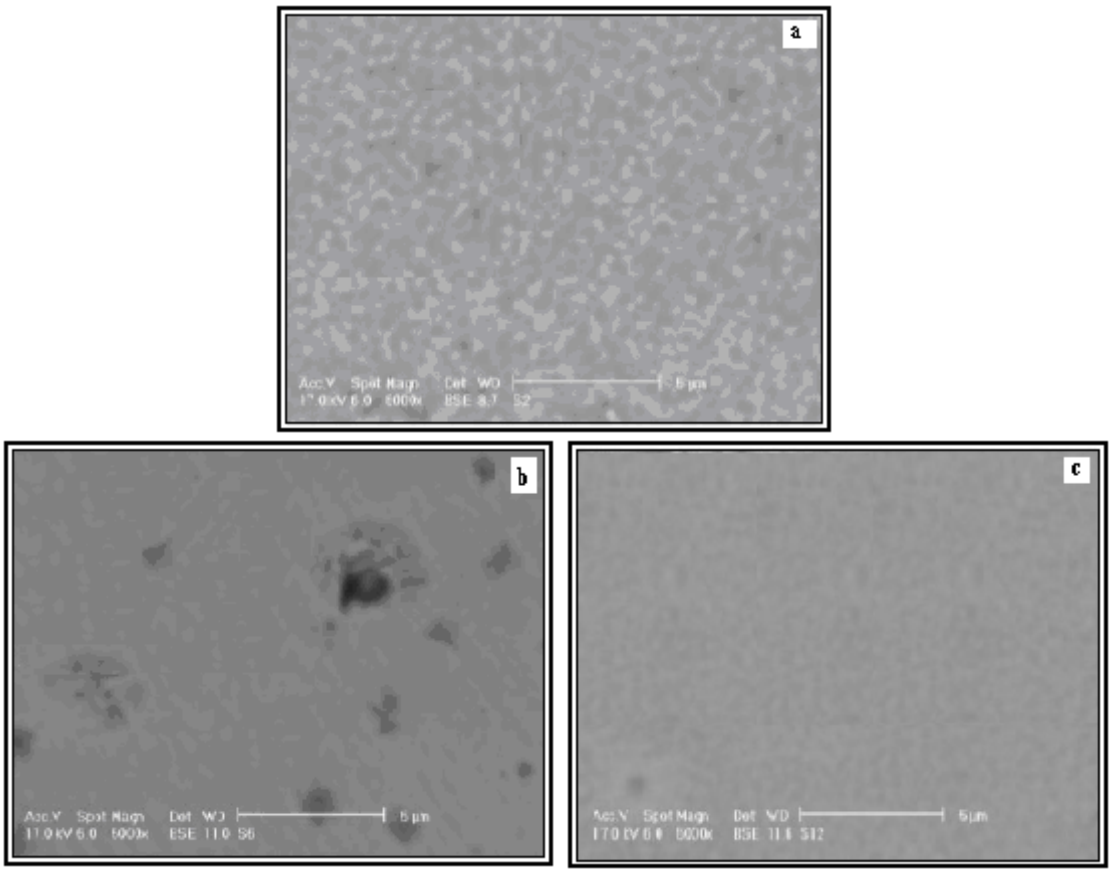

Fig. 5. *Images (SEM) of TiCx microstructure coating deposited at three different duty cycles: a) 35%; b) 43%; c) 50%*

Therefore, impurities play an important role in generating the residual stress in the coating. Indeed, deposition of the TiC microstructure coating at middle duty cycle (43%) may relieve the residual stress of the thin film, and the dependence between residual stress and preferred orientation in the TiC microstructure coating reveals that the preferred orientation is (200) [21]. Small areas of (111) textured TiC were also observed in this paper, while the general texture was predominantly (200).

5. 2. Effect of duty cycle on tribological behaviour

Figure 4 shows the variation of friction coefficient in the TiC microstructure coating as a function of the number of cycles for three different duty cycles, namely 35, 43 and 50%. For the coating, the friction coefficient in the initial stage is 0.13, 0.06 and 0.15 for 35, 43 and 50% duty cycle respectively. The friction coefficient of the TiC microstructure coating deposited at 35% duty cycle presents a drastic change from 0.13 to 0.6 and, after 200 and 400 cycles, presents a drastic change from 0.6 to 1.1 for both TiC microstructure coatings deposited at 35% duty cycle and substrate [22].

For the TiC microstructure coatings deposited at 43 and 50% duty cycles, the friction coefficients were constant with an average value of, 0.08 and 0.19 respectively and fluctuate slightly with changes in the number of cycles. Especially at the initial wear stage, the friction coefficient of the TiC microstructure coatings deposited at 35% duty cycle drastically fluctuated with changes in the number of cycle, indicating that wear mainly takes place at some protruding portions of the pin and discs. This

behaviour was seen for the final wear stage of the TiC microstructure coatings.

***Table 4**. TiCx microstructure coating at three different duty cycles*

Duty cycles	35%	43%	50%
Ra [µm]	8.992	10.509	14.057
Rrms [µm]	11.668	13.429	18.034

Table 3 shows the properties of TiC microstructure coating at three different duty cycles. It can be seen that the wear mass loss for both the widia substrate and the TiC microstructure coatings increases with the increase in number of cycles. Compared with the substrate, the TiC microstructure coatings have smaller mass loss, especially for coatings deposited at 43 and 50% duty cycles.

In addition, the mass loss of the W–Co pins drastically increases with the increase in number of cycles. It is mentioned that the W–Co pin as the counter body of the TiC microstructure coatings presents less wear mass loss compared to widia substrate. However, it was found that the friction coefficient decreased with the increase in duty cycle from 35 to 43% and then increased with the rise in duty cycle from 43 to 50%. However, the TiC microstructure coating, which was applied at 43%, exhibited the lowest friction coefficient of ~0.06, as shown in Figure 4.

Duty cycles	Images AFM 3D Dimension 1x1 µm	Images AFM 2D Dimension 1x1 µm
35%	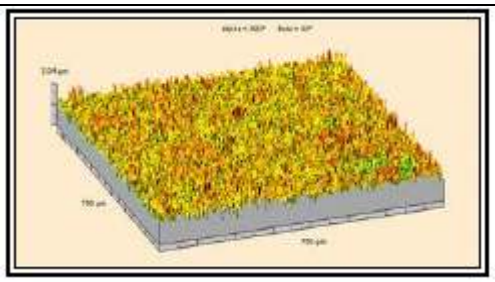	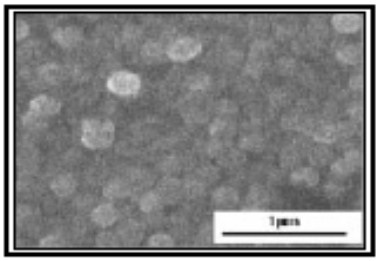
43%	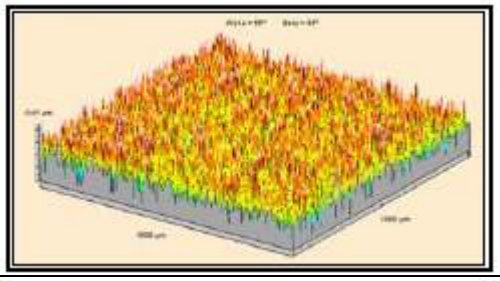	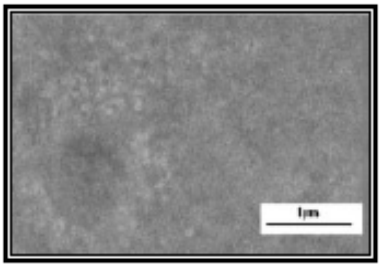
50%	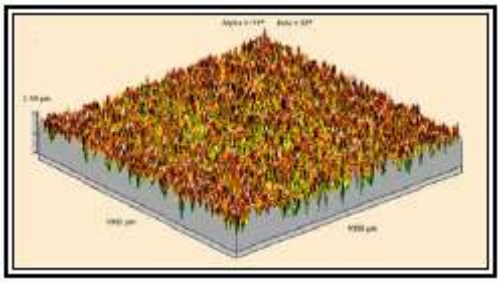	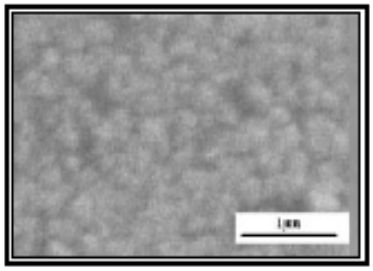

***Fig. 6.** Images (AFM) and roughness plot of TiCx microstructure at three different duty cycles: a 35%; b 43%; c 50%*

According to Fig. 4, the coating deposited at lower duty cycle showed a much higher friction coefficient than that of the higher duty cycle. It should be considered that the high friction coefficient is probably due to the coarsening of particles in the depositing process. Actually, the increase in particle size may decrease the convergence of particles. Figure 5 demonstrates the SEM images of the TiC microstructure coating in three kinds of duty cycles, i.e. 35, 43 and 50%. Surface morphology plays an important role in the tribology behaviour of the TiC microstructure coating. It can be seen that the surfaces of the two coatings, which were deposited at 35 and 50%, show similar microstructures (rough

surfaces) containing 0.1–0.2 μm aggregates of 4–10 μm TiC grains, and increasing the duty cycle from 35 to 43% produces relatively smooth and dense surfaces. The surface topographies and roughness plot of the TiC microstructure coating at three different duty cycles, including 35, 43 and 50%, are shown in Fig. 6. This Figure depicts that asperities are distributed over a broader range of heights for 50% compared to 35 and 43%.

The results of surface roughness are presented in Table 4. It can be seen from Table 4 that Ra is defined as the mean value of the surface height relative to the centre plane, and Rrms is the root mean square roughness profile of the surface height within the scanned area, and both have been used to explain the surface morphology [23].

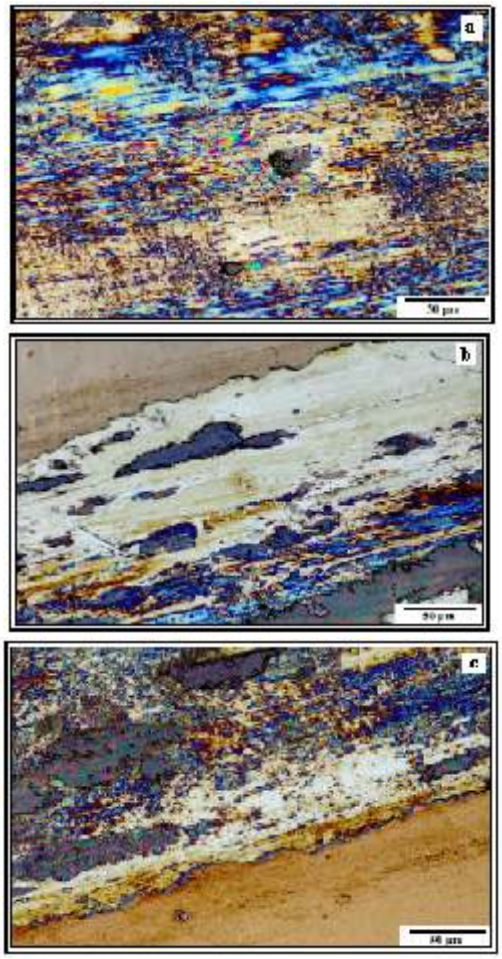

Fig. 7. *Optical microscopy images of TiCx microstructure coating wear track at three different duty cycles: a) 33%; b) 40%; c) 50%*

This is confirmed by roughness values Rrms of 11.668, 13.429 and 18.034 μm at three different duty cycles, including 35, 43 and 50% respectively.

Both the AFM images and the Rrms values prove that increasing duty cycles from 35 to 43 and 50% causes a reduction in overall roughness of the coating. Therefore, the SEM and AFM images of the TiC microstructure coating (Figs. 5 and 6) indicated that the growth mechanism of coatings at 35 and 50% are island-like growths, while at 43%, there is a layer growth. Therefore, the relatively smooth and dense surfaces (at 43%) lead to the lowest friction coefficient of ~0.06, as shown in Fig. 3. Nevertheless, the deposition parameters are responsible for the layer growth, and it can be concluded for the NPCVD process that the chemical deposition conditions, during deposition, such as duty cycles, determine the nucleation and growth of the layer.

It is noteworthy that increasing the hardness of the TiC microstructure coating is determined by decreases the friction coefficient. In addition, the gradual increase in friction coefficient at 43 and 50% is probably due to the decrease in hardness steadily. The failure of the TiC microstructure coating was determined by the increase in friction coefficient to 1.

The related optical microscope results are presented in Fig. 7.

Figure 7a–c reveals that a peeling of the TiC microstructure coating from the substrate has occurred on the surface. This Figure indicates that the TiC microstructure coatings were worn off to different degrees and islands of broken coatings, where coating was delaminated and substrate was exposed, were formed on the wear tracks. Increasing duty cycles from 35 to 43 or 50% causes to find a few TiC particles in the wear track of the TiC microstructure coating, and according to Fig. 7a, it can be found that the tribology behaviour of TiC microstructure coating for lower duty cycle (35%) may be due to oxide formations during the wear test.

The main wear mechanism of the TiC microstructure coating is the pull-out of particles for fatigue. This is because the extrusive particles bear the load during the process of wear.

After the long term action of the load, the bond will be slacked, and finally, the particles will be pulled out. Therefore, the TiC microstructure coating, which was deposited at 43%, has good wear resistance for its good plasticity (elasticity and microhardness) and compact fine grain microstructure. In addition, the lowest friction may be attributed to the formation of carbon compounds, such as CO_2 and amorphous carbon, and graphitization in the coating wear track, as shown in Fig. 7b. It should be noted that the main wear mechanisms of 50% duty cycle are the pull-out of particles for fatigue (such as oxide formations) and the formation of carbon compounds in the coating wear track, as can be observed in Fig. 7c.

6. Conclusion

Among several parameters, duty cycle plays an essential role as a thermodynamic and kinetic parameter.

The main conclusions are the following.

1. The (200) plane is the preferred structure at lower duty cycle (35%), and an increasing duty cycle from 35 to 50% causes the formation of other planes of TiC, such as (111) and (220) planes.

2. These peaks move to higher angles with increasing duty cycles from 35 to 50%.

3. The grain size of the TiC microstructure coating (~7 μm) was decreased by raising the duty cycle, since the number of nucleation was increased by rising the duty cycle.

4. The residual stress in the TiC microstructure coating is compressive, and the increasing duty cycle from 35 to 50% causes to drop the compressive stress.

5. The highest compressive residual stress was obtained at the lowest duty cycle (35%), and the lowest compressive residual stress was attained at middle duty cycle (43%).

6. The friction coefficient decreases with the increase in duty cycle from 35 to 43% and then increases with the rise in the duty cycle from 43 to 50%.

7. The lowest friction coefficient is ~0.06, and the TiC microstructure coating (which was applied at 43%) with the lowest residual stress (-0.12985 MPa) gives the best wear resistance under loading experiment.

References

[1]. L. R. Katipelli, A. Agarwal and N. B. Dahotre - Appl. Surf. Sci., 2000, 153, p. 65–78.
[2]. A. Kumar, H. L. Chan, J. S. Kapat - Appl. Surf. Sci., 1998, 127, p. 549.
[3]. A. Man, P. Aubert, F. Mercier, H. Khodja, C. Berthier, P. Houdy - Surf. Coat. Technol., 2005, 194, p. 190–195.
[4]. A. Leonhardt, K. Bartsch, I. Endler - Surf. Coat. Technol., 1995, 76, p. 225–230.
[5]. I. Dahan, A. Admon, N. Frage, J. Sariel, M. P. Dariel, J. J. Moore - Surf. Coat.Technol., 2001, 137, 111, p. 154-164.
[6]. D.-J. Kim, J.-Y. Kang, A. Nasonova, K.-S. Kim, S.-J. Choi, Korean J. Chem. Eng., 2007, 24 (1).
[7]. M. Meyyappan - J. Vac. Sci. Technol. A, 1996, 14A, (4), p. 2122.
[8]. S. Constantinescu - *Nitride coatings on widia substrate for mechanical applications*, Journal Surface Engineering, vol. 25, no. 1, 2009, p. 77-81, www.ingentaconnect.com.
[9]. C. Jarms, H.-R. Stock, H. Berndt, K. Bartsch, A. Leonhardt, B. Arnold - Surf. Coat. Technol., 1998, 98, p. 1547-1552.
[10]. N. Lisi, R. Giorgi, T. Dikonimos, E. Salernitano, S. Gagliardi, L. Giorgi, V. Contini, P. Morales, Diamond Relat. Mater., 2010, 19, p. 1382–1386.
[11]. I. Pollini, A. Mosser, J. C. Parlebas - Phys. Rep., 2001, 355, p. 1.
[12]. N. B. Thomsen, A. Horsewell, K. S. Mogensen, S. S. Eskildsend, C. Mathiasend, J. Buttiger - Thin Solid Films, 1998, 333, p. 50–59.
[13]. L. Hultman, J. E. Sundgren, J. E. Greene, D. B. Bergstrom, I. J Petrov - Appl. Phys., 1995, 78, (9), p. 5395.
[14]. E. Vogelzang, J. Sjollema, H. J. Boer, J. T. M. de Hosson - J. Appl. Phys, 2010, 61, p. 4606.
[15]. V. Spassov - *Alloying a hard phase with a solid lubricant an approach concept for hard, self-lubricating PVD coatings for tribological applications*, PhD thesis, Faculty of Natural Sciences, University of Basel, Basel, Switzerland, 2009.
[16]. M. Lindquist, O. Wilhelmsson, U. Jansson, U. Wiklund - Wear, 2009, 266, p. 379-387.
[17]. X. L. Bui, Y. T. Pei, J. Th. M. de Hosson - Surf. Coat. Technol., 2008, 202, p. 4939-4944.
[18]. D. Galvan, Y. T. Pei, J. Th. M. de Hosson - Acta Mater., 2005, 53, p. 3925-3934.
[19]. A. J. Perry, J. A. Sue, P. J. Martin - Surf. Coat. Technol., 1996, 81, p. 17.
[20]. M. A. R. M. Miranda, J. M. Sasaki, A. S. B. Sombra, C. M. R. Remedios - Mater. Res., 2006, 9, p. 243–246.
[21]. S. Yulong, U. P. Hongrui, X. Yan, X. Guangwen, Z. Cheng, L. Shizhi - Surf. Coat. Technol., 1998, 132, p. 26-30.
[22]. U. Bryggmar, S. Hogmark, O.Vingsbo - *Abrasive wear studied in a modified impactzz testing machine*. Proc. 2nd Int. Conf. on Wear of Materials, Dearborn, 1979, ASME, New York, NY, p. 292-303.
[23]. T. Fang, S. Jian, D. Chuu - *Shanaghi et al. Effect of duty cycle on TiCx nanostructure coating 370 Surface,* Appl. Surf. Sci., 2004, 228, p. 365-372.

MANUSCRISELE, CĂRŢILE ŞI REVISTELE PENTRU SCHIMB, PRECUM ŞI ORICE CORESPONDENŢE SE VOR TRIMITE PE ADRESA:

MANUSCRIPTS, REVIEWS AND BOOKS FOR EXCHANGE COOPERATION, AS WELL AS ANY CORRESPONDANCE WILL BE MAILED TO:

LES MANUSCRIPTS, LES REVUES ET LES LIVRES POUR L'ECHANGE, TOUT AUSSI QUE LA CORRESPONDANCE SERONT ENVOYES A L'ADRESSE:

MANUSCKRIPTEN, ZIETSCHRITFTEN UND BUCHER FUR AUSTAUCH SOWIE DIE KORRESPONDENZ SID AN FOLGENDE ANSCHRIFT ZU SEDEN:

After the latest evaluation of the journals achieved by National Center for the Science and Scientometry Politics (**CENAPOSS**), as recognition of its quality and impact at national level, the journal is included in B^+ category, 215 code (http://cncsis.gov.ro/userfiles/file/CENAPOSS/Bplus_2011.pdf).

The journal is indexed in:

CSA: http://www.csa.com/ids70/serials_source_list.php?db=mechtrans-set-c

EBSCO: http://www.ebscohost.com/titleLists/a9h-journals.pdf

Copernicus: http://journals.indexcopernicus.com/karta.php

The papers published in this journal can be visualized on the "Dunarea de Jos" University of Galati site, the Faculty of Materials Science and Environment, pages: http://www.sim.ugal.ro/Annals.htm, http://www.imsi.ugal.ro/Annals.html.

Publisher's Name and Address:
Contact person: Antoaneta Căpraru
Galati University Press - GUP
47 Domneasca St., 800008 - Galati, Romania
Phone:+40 336 130139, Fax: +40 236 461353
Email: gup@ugal.ro

Editor's Name and Address:
Prof. Dr. Eng. Marian BORDEI
Dunarea de Jos University of Galati, Faculty of Materials and Environmental Engineering

111 Domneasca St., 800201 - Galati, Romania
Phone: +40 336 130208
Phone/Fax: +40 336 130283
Email: mbordei@ugal.ro

AFFILIATED WITH:

- ROMANIAN SOCIETY FOR METALLURGY
- ROMANIAN SOCIETY FOR CHEMISTRY
- ROMANIAN SOCIETY FOR BIOMATERIALS
- ROMANIAN TECHNICAL FOUNDRY SOCIETY
- THE MATERIALS INFORMATION SOCIETY (ASM INTERNATIONAL)

Edited under the care of Faculty of MATERIALS AND ENVIRONMENTAL ENGINEERING

Annual subscription (4 issues per year)

Edited date: 15.09.2014
Issues number: 200
Printed by Galati University Press
accredited CNCSIS
47 Domneasca Street, 800036, Galati
Romania